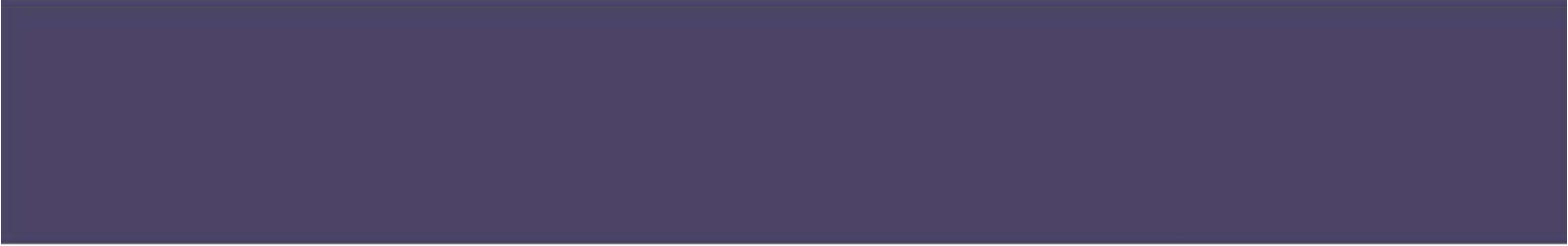Catharina Knieke

Fracture at the Nanoscale and the Limit of Grinding

Cuvillier Verlag Göttingen
Internationaler wissenschaftlicher Fachverlag

Fracture at the Nanoscale
and the Limit of Grinding

Fracture at the Nanoscale and the Limit of Grinding

Partikelbruch im Nanometerbereich und die Grenze der Echtzerkleinerung

Der Technischen Fakultät der Universität Erlangen-Nürnberg zur

Erlangung des Grades

DOKTOR-INGENIEURIN

vorgelegt von

Catharina Knieke

Erlangen - 2012

Als Dissertation genehmigt von der Technischen Fakultät der Universität Erlangen-Nürnberg

    978-3-95404-085-8

*"Die Neugier steht immer an erster Stelle
eines Problems, das gelöst werden will."*
(Galileo Galilei)

*"Wohin die Reise auch geht, hängt nicht davon ab, woher
der Wind weht, sondern wie man die Segel setzt"*
(Chinesisches Sprichwort)

Acknowledgements

The present work was performed from 2006 to 2010 at the Institute of Particle Technology at the Friedrich-Alexander University Erlangen-Nürnberg.

This thesis would not have been possible without the support of many people, who need to be recognized here.

First and foremost, I wish to express my deepest gratitude to my supervisor Prof. Dr.-Ing. Wolfgang Peukert for giving me the opportunity to conduct this thesis at his Institute. He always gave me the freedom to realize my own ideas and pushed me beyond my limits.

Additionally, I would like to thank my second referee Prof. Dr.-Ing. Arno Kwade for helpful advice and active coorperations.

Special thanks go to my Semester and Diploma students namely Constanze Deimling, Stefan Romeis, Angela Berger, Christian Rosskopf, Christian Schmidt, Michael Forstmeier, Matthias Radke and Christian Barthold as well as several student assistants for their enthusiastic commitment during their work.

I give my heartfelt gratitude to Beate Bierlein, Manuela Hollmach and Sandra Wittpahl for their reliable support in the laboratory during the years.

Moreover, I would like to acknowledge all my colleagues from the LFG and collaborating Institutes for the comfortable and motivating atmosphere and helpful discussions.

Maxx W. Capece is greatfully acknowledged for the grammar corrections of this thesis.

Finally, I want to thank my parents for their mental and financial support as well as their continuous encouragement throughout my whole education.

Abstract

Besides chemical synthesis routes, nanoparticles can be produced in top-down processes nowadays. Stirred media mills are commonly used to break particles down to the nanometer range. Thereby, their stabilization against agglomeration plays a major role to obtain nanoparticle suspensions with the desired properties. Whereas different stabilization methods have been a subject of much research in the last few years, the breakage behavior of nanoparticles is not well understood for the time being. A discrepancy exists between the common state of the art that particles cannot be comminuted below the brittle-to-ductile transition size, which is in the range of a few μm for ceramic particles, and the experimental findings of particles sizes in the nanometer range. In this work, long term grinding experiments of different oxide and non-oxide inorganic materials were carried out to investigate the breakage behavior in the nanometer range. By means of X-ray diffraction analysis and TEM investigations, the evolution of the internal microstructure of the particles was followed during the grinding treatment. A strong correlation between the microstructure and the fracture ability was found. In addition, the existence of a true grinding limit, where no further fracture takes place, and the influence of process and environmental conditions was demonstrated. A physical explanation of the grinding limit originates from changes in the defect structure below a critical crystallite size.

Besides the breakage behavior of brittle ceramics, the grindability of graphite particles as a typical layered material was also investigated. The strong anisotropy of the bond forces in the crystal results in a selective size reduction during the grinding process. By adjusting the process conditions in a way that the acting forces overcome the attractive van der Waals forces between the graphene sheets without breaking them, the production of thinnest flakes with high aspect ratios is allowed. The size reduction was realized as a kind of peeling process. Various analysis techniques such as AFM, Raman spectroscopy, TEM or XPS were employed to characterize the delaminated sheets, especially to determine the exact number of layers. Furthermore, information about the yield of delaminated sheets was given and first examples of application are presented.

Zusammenfassung

Neben chemischen Synthesemethoden können Nanopartikeln heutzutage auch über Top-down Prozesse in Rührwerkskugelmühlen hergestellt werden. Dabei stellt ihre Stabilisierung gegen Agglomeration ein wichtiges Kriterium dar, um Nanopartikelsuspensionen mit den gewünschten Eigenschaften zu erhalten. Während in den letzten Jahren Stabilisierungsmöglichkeiten Gegenstand der Forschung waren, ist das Bruchverhalten von Nanopartikeln bis heute nicht verstanden. Es existiert eine Diskrepanz zwischen dem vorherrschenden Stand der Technik, dass keine Zerkleinerung unterhalb des Spröd-Duktil-Übergangs möglich ist, der für keramische Partikeln im Bereich von weinigen μm liegt, und experimentell erreichten Partikelgrößen im Nanometerbereich. Im Rahmen dieser Arbeit wurden daher Langzeitzerkleinerungsversuche mit verschiedenen Materialien durchgeführt, um das Bruchverhalten im Nanometerbereich zu untersuchen. Mit Hilfe von XRD und TEM Analytik konnte die Entwicklung der inneren Mikrostruktur der Partikeln während der Zerkleinerung verfolgt werden. Ein Zusammenhang zwischen Mikrostruktur und Bruchfähigkeit wird nachgewiesen. Zusätzlich wird gezeigt, dass eine untere Zerkleinerungsgrenze existiert und wie diese Grenze von Prozess- und Umgebungsbedingungen abhängt. Eine physikalische Erklärung der Zerkleinerungsgrenze liegt in der Veränderung der Defektstruktur unterhalb einer kritischen Korngröße begründet.

Neben dem Bruchverhalten von spröden Keramiken, wird auch die Zerkleinerungsfähigkeit von Graphit als ein typisches Schichtmaterial untersucht. Die starke Anisotropie in den Bindungskräften resultiert in einer selektiven Zerkleinerung während des Mahlvorgangs. Eine Anpassung der Prozessbedingungen in einer Weise, dass die anziehenden van der Waals Kräfte zwischen den Graphen-Lagen überwunden werden, ohne die Schichten selbst zu brechen, erlaubt die Herstellung von dünnsten Flakes mit hohem Aspektverhältnis in einem Delaminierungs-Prozess. Verschiedene Analysetechniken wie AFM, Raman Spektroskopie, TEM oder XPS werden zur Charakterisierung der Schichten eingesetzt. Zudem werden in dieser Arbeit Informationen über die Ausbeute an delaminierten Schichten gegeben und erste Anwendungsbeispiele vorgestellt.

Nomenclature

Latin Symbols

A	J	Hamaker constant
A_{400}	-	absorption (at λ= 400 nm)
A_{GC}	m^2	surface area of the grinding chamber
b	Å	Burgers vector
c	g/l	concentration
c	nm	crack length
c_m	-	solid content (mass fraction)
c_v	-	solid content (volume fraction)
cmc	mol/l	critical micelle concentration
d	Å	lattice parameter
d	nm	interlayer distance
d_{film}	m	film thickness
d_{GM}	m	diameter of the grinding media
d_{crit}	m	critical diameter
E_m	kJ/kg	mass specific energy input
$E_{m,p}$	kJ/kg	product related mass specific energy input
F	N	force
$FWHM$	°	full width at half maximum
G	GPa	shear modulus
h	nm	sheet thickness
H	MPa	hardness
I	A	current
k	MPa$\sqrt{m}$	strengthening coefficient
k_{app}	1/s	apparent rate constant
K	-	shape factor
$K_{I,c}$	MPa$\sqrt{m}$	fracture toughness
l	nm	distance dislocation - particle surface
L	m	length
m_p	kg	mass of product particles
n	1/min	rotational stirrer speed

p	-	filler content (mass fraction)
p_c	-	percolation threshold (mass fraction)
P_t	W	power input
P_0	W	no-load power
r	m	radius
R	J/m^2	crack resistance
R_s	Ω	surface restistance
S_m	m^2/g	mass specific surface area
SE	J	stress energy
SE_{GM}	J	stress energy of the grinding media
SE_p	J	product related stress energy
SN	-	stress number
t	s	time
T	°C	temperature
U	V	voltage
x	m	particle diameter
x_{BDT}	m	brittle-to-ductile transition size
$x_{1,2}$	nm	Sauter diameter, primary particle size
x_{crys}	nm	crystallite size
v_t	m/s	stirrer tip speed
V_{GC}	m^3	grinding chamber volume
Y	GPa	Young's modulus
Y_{GM}	GPa	Young's modulus of grinding media
Y_P	GPa	Young's modulus of product particles

Greek Symbols

Λ	nm	distance
ϵ_o	-	maximum strain
η_{fl}	Pa·s	dynamic fluid viscosity
φ_{GM}	-	filling ratio of milling beads
γ	J/m^2	surface energy

10

$\Gamma_{G,L}$	°	full width at half maximum of Gauss or Lorentz function
λ	nm	wavelength
μ	-	friction coefficient
ν	-	Poisson's ratio
ρ_P	kg/m^3	particle density
ρ_{GM}	kg/m^3	grinding media density
σ	S/cm	specific conductivity
σ_B	MPa	breakage stress
σ_i	GPa	image stress
σ_P	MPa	Peierls stress (friction stress)
σ_y	GPa	yield stress
σ_{th}	GPa	theoretical shear strength
τ	GPa	shear stress
Θ	°	diffraction angle
ζ	mV	zeta potential

Abbreviations

AFM	atomic force microscopy
BET	Brunauer-Emmett-Teller
DLS	dynamic light scattering
GO	graphite oxide
HOPG	Highly oriented pyrolitic graphite
HRTEM	high resolution transmission electron microscopy
Pt-NP	platinum nanoparticles
RT	room temperature
SEM	scanning electron microscopy
TEM	transmission electron microscopy
XPS	X-ray photoelectron spectroscopy
XRD	X-ray diffraction
YSZ	yttria stabilized zirconia

Contents

1. Introduction

Nanoparticles are widely used in many industrial fields such as the ceramic, pharmaceutical, chemical or microelectronic industry. Caused by the extraordinary high ratio of surface area to volume, nanoparticles can yield totally new properties compared to the bulk material. Additionally, nanoparticles can be used as building blocks to create larger structures with tailored properties. For nanoparticle production, two distinctly different fabrication routes exist. Bottom-up processes are based on a direct arrangement of molecules to particulate clusters, whereas the top-down approach describes the production of nanoparticles by fragmentation of coarser feed materials. Top-down processes can be realized for example in wet operated stirred media mills, which can supply the high specific energies necessary for nanoparticle production. Stirred media milling allows the production of highly concentrated suspensions with high throughputs in an industrially well established process. In general the production of nanoparticles requires two preconditions. The first one is the fracture of the particles as a result of a sufficiently high stress field inside the particles, which has to build-up during the impact between the grinding media. The second condition demands the stabilization of the created fragments against agglomeration. Below sizes of about 1 μm, particles tend to agglomerate because of an increased Brownian motion and smaller interparticle distances, both enhancing the collision rate of the particles. As a consequence a steady state between breakage and agglomeration appears in the milling process, which strongly affects the grinding result. In the last few years many research activities have been carried out in the field of stabilization to control the agglomeration behavior in wet grinding processes by an adjustment of the interparticle interactions [Sten 05a], [Mend 04b].
To this day the breakage mechanisms of nanoparticles are still poorly understood. In contradiction to earlier theories that predict a grinding limit for

brittle oxide materials in the lower micrometer range [Scho 71], [Kend 78], [Haga 79], particle sizes down to 10 nm can nowadays be observed by real breakage. Approaches to explain the observed discrepancy between the postulated grinding limits and the experimentally achieved particle sizes are still missing. Therefore, the main objective of this work is to gain deeper understanding about the breakage mechanisms at the nanoscale. In general three questions can be defined, which display the focus of this thesis:

1. How does particle breakage become possible in the nanometer range?
2. Does there exist a true limit of grinding?
3. If yes, which parameters affect the limit of grinding?

To answer these questions a closer look into the particles' microstructure is necessary. Microstructural changes in terms of crystallite size and microstrain evolutions under mechanical stressing are investigated under different process conditions in stirred media milling. Beside the breakage behavior of brittle ceramic particles, the size reduction characteristic of graphite particles as a typical example of a layered material with a strong anisotropy in the bond forces is presented in this work.

18

2. State of the Art

2.1. Ultrafine grinding in stirred media mills

The top-down approach for the production of ultra fine particles can be reasonably realized in stirred media mills since they can provide the necessary high specific energies for fracturing fine particles. Stirred media mills are the most frequently used milling machines in many fields of industry. A consideral amount of research investigations on the operation performance of stirred media mills has been carried out at the Institute of Mechanical Process Engineering (today: Institute for Particle Technology) in Braunschweig, Germany. Fundamental results of their research activities are summarized in section 3.1.

Recently, it was shown by Stenger and Mende that even nanoparticles can be produced by stirred media milling [Sten 05c], [Mend 03]. The authors figured out that an appropriate stabilization is necessary to avoid agglomeration of the created fragments to improve the grinding results. Below particle sizes of about 1 μm the collision rate of the particles increases because the particles show an enhanced Brownian motion and the interparticle distances decrease at a constant solid content. Hence, the overall grinding result in the submicrometer range depends on both, breakage and stabilization. Since many important suspension properties such as the rheological behavior [Sten 05b] or optical properties are affected by the degree of agglomeration, Stenger and Mende focused on the stabilization of inorganic oxide particles in aqueous media by a pH adjustment.

Later on, Sommer and Breitung-Faes extended the work of Stenger and Mende to non-aqueous media and the use of polymers as dispersing agents [Somm 07], [Brei 09]. Sommer showed for polyethylene oxide that large polymers can break under high shear forces during the milling process. Furthermore, he discovered a dampening effect of the polymer leading to

reduced breakage kinetics. Based on the work of Stenger and Mende several other groups extended their research investigations to the submicrometer size range [Wang 06], [Vita 08], [Henn 10]. Nano-sized organic pigment particles have been produced via wet milling and stabilizing in the group of Scarlett [Bilg 06]. Particle sizes down to 10 nm could be produced with polymeric grinding media of about 20 μm in size.

Microstructural changes of hematite during wet and dry grinding in different kinds of media mills were investigated in the group of Forssberg [Pour 08], [Pour 07]. By means of X-ray diffraction the evolution of crystallite size and lattice strain was detected with milling time. A decrease of crystallite size and an increase of dislocation density were observed. Simultaneously the amorphous content of the product powders rises caused by highly energetic impacts of the grinding media. A limit of grinding was not observed in their investigations.

2.2. The limit of grinding

Throughout the history there are many discussions about a size limit in comminution processes. In general, the grinding limit can be the result of a

- machine limitation: problem of transferring energy from the milling machine to the product particles. In media milling this, for instance, can be the case if no trapping of particles between the grinding media or a strong dampening of the bead motion in a highly viscous media occurs.

- material limitation:
  a) agglomeration or welding (relevant in dry grinding applications, where high temperatures or high local stresses are present)
  b) no further breakage of the particles below a certain size.

Whereas the machine limitation can be overcome by an optimization of the milling device or an adjustment of process parameters, the material limitation determines the minimal particle size which could theoretically be achieved in grinding processes. The existence of this minimal particle size was predicted by several authors. First of all, Schönert presented in 1971 an

20

experimental study about single particle compression experiments of quartz and limestone. He claims that a limiting particle size in grinding operations is reached if plastic flow of the particles takes place exclusively instead of breakage. An almost breakage-free deformation of the investigated particles was achieved for sizes below 2 μm and 4 μm for quartz and limestone, respectively [Scho 71]. Later on, Schönert published a theoretical approach to estimate the smallest specimen size in milling experiments based on considerations from Dugdale [Dugd 60]. This size depends on the size of the plastic zone δ which is formed around the crack tip, if the local stress at the notch root exceeded the yield stress of the material [Scho 88]. Schönert's equation (Eq. 2.1) is valid, if the length of the fracture zone is much smaller than the length of the crack.

$$\delta \approx 0.4 \left(\frac{RY}{\sigma_y^2} \right) \tag{2.1}$$

Schönert specified values for δ between 1 nm and 10 nm for brittle minerals. This length determines the minimum separation between fractures and, therewith the size of the smallest fragments (ca. 5 - 10 δ). The material data used for this estimation are not mentioned in the publication of Schönert. From today's perspective, an exact calculation of the plastic zone size is difficult because of the lacking of reliable material data especially for ceramic particles and in particular for nano-sized ceramic particles as they are known to yield different properties as their bulk materials [Gerb 06]. Additionally, the crack resistance R depends on the notch depth as well as the fracture history, which is usually visualized in so-called R-curves [Evan 84], [Kneh 82].

Replacing the crack resistance R and the Young's modulus Y by the fracture toughness (mode 1: crack opening under a normal tensile stress perpendicular to the crack) K_{1c} with the relation $K_{1c} = \sqrt{RY}$, gives the following expression for the minimal particle size:

$$d_{crit,S} = 2...4 \left(\frac{K_{1c}}{\sigma_y} \right)^2 \tag{2.2}$$

In 1978 Kendall [Kend 78] published a paper about the *"The impossibility of comminuting small particles by compression"*. For a special geometry based on the Griffith energy criterion for fracture, he derived an expression for a critical particle size, below which crack propagation is impossible under compressive force (Eq. 2.3). Kendall postulated that bodies smaller than d_{crit} appear ductile and are pressed flat under loading. d_{crit} is therewith equal to the size of brittle-to-ductile transition.

$$d_{crit,K} = 10.7 \left(\frac{K_{1c}}{\sigma_y} \right)^2 \tag{2.3}$$

Kendall confirmed his theory by single compression experiments of polystyrene specimens. He observed that the brittle-to-ductile transition size was in good agreement with the theoretical predictions from Eq. 2.3.

One year later, Hagen described that crack nucleation is the limiting factor for fracture rather than crack propagation as assumed by Kendall. Beside a critical load, the presence of initial flaws with a minimal length inside the material is another condition for crack nucleation. The size of the critical flaw length and therewith the minimal grain size can be estimated with Eq. 2.4 [Haga 79].

$$d_{crit,H} = 29.5 \left(\frac{K_{1c}}{H} \right)^2 \tag{2.4}$$

For Al_2O_3 particles, a critical size of 3.3 μm and 1.1 μm for SiO_2 was determined from Hagan's equation. If the hardness H is replaced by the expression $H = 3\sigma_y$ [Tabo 70], the critical size can be written in the following form:

$$d_{crit,H} = 3.3 \left(\frac{K_{1c}}{\sigma_y} \right)^2 \tag{2.5}$$

The independent approaches from Schönert, Kendall and Hagan show the same dependence of the critical particle size. Only the constants differ resulting from different adopted body geometries.

Several authors have compared their grinding results with the predicted limits. Ghadiri, for instance, investigated the milling behavior of α-lactose

monohydrate and microcrystalline cellulose in an oscillatory single ball mill. Particle sizes well below the predicted limits of Kendall and Hagan were achieved [Kwan 04]. Also, the grinding results of Stenger and Mende cannot be explained by the dominating theories of Schönert, Kendall and Hagan. The main reason for this discrepancy might be the different loading cases in the investigations. In the experiments of Schönert and Kendall the bodies were compressed under static loading with high load forces, while the media milling experiments of Ghadiri and Stenger were carried out under cyclic loading, where the applied forces are much smaller. However, breakage must be possible below the size of brittle-to-ductile transition by other breakage mechanisms, which cannot be described with the above equations.

The grinding limit in wet media milling

In 1992 Jimbo [Jimb 92] presented results of milled alumina suspensions in a stirred media mill. He distinguished between a minimal particle size that was measured with scattering methods and a much smaller particle size that was calculated from the mass specific surface area of the ground powders (S_m). Jimbo also claimed that sizes determined from S_m reach a certain value for long grinding times which is independent of the mechanical grinding conditions and the feed particle size. Cho et al. also carried out investigations of the grinding limit in stirred media milling for quartz particles dispersed in water [Cho 96]. A grinding limit at a size of about 30 nm was found by means of dynamic light scattering, TEM, and gas adsorption measurements. A physical explanation for the observed limit is not given in the publication of Cho.

The grinding limit in dry media milling

Dry grinding applications, typically realized in planetary ball mills, are widely used in the field of mechanical alloying or for grain refinement of metals to improve selected properties. In contrast to wet media milling, the grinding limit in dry operated high-energy mills is determined by an equilibrium between size reduction and growth processes. Caused by strong welding phenomena, the particles typically remain polycrystalline during the milling procedure so that it has to be distinguished between a minimal particle and a minimal crystallite (i.e. grain) size. The minimal particle size is determined by an equilibrium between fracture, agglomeration and possible welding processes. Since agglomeration effects cannot be avoided as in the case of wet milling by the addition of grinding aids, much larger particle sizes are obtained in dry grinding experiments. Due to the missing surrounding medium, heat can hardly be dissipated and the grinding media impacts are much more intensive, which often results in welding of the particles. The minimal crystallite size is determined by an equilibrium between grain refinement through a severe plastic deformation and the recovery by thermal processes (splitting and coalescence/recrystallization of grains) [Kara 03].

Eckert and later on Koch investigated such equilibrium conditions for various metal particles [Ecke 92], [Koch 97]. Eckert showed that a steady state grain size is reached when the refinement rate equals the recovery rate. Both rates depend on intrinsic material properties as well as on process conditions like impact intensities [Ecke 95]. Since the recovery rate scales inversely with the melting temperature of the materials, high-melting-point materials yield the smallest grain sizes. If no recovery takes place, the smallest achievable size by milling would be determined by the minimum grain size that can sustain a dislocation pile-up. This minimum grain size is only determined by intrinsic material properties so that the material itself provides a limit for further grain refinement. Nieh et al. estimated this limit as the equilibrium separation distance between two edge dislocations by [Nieh 91]

24

$$L = \frac{3Gb}{\pi(1-\nu)H} \tag{2.6}$$

with the shear modulus G, Burgers vector b, Poisson's ratio ν, and hardness H of the material. Applying this relation to ball-milled metal powders shows that the achieved minimum grain sizes are larger than the sizes obtained from Eq. 2.6. The reason is the simultaneous recovery that dominates at small grain sizes and prevents further size reduction.

The theory of an equilibrium between grain refinement and recovery in dry milling applications was confirmed by the group of Boldyrev [Bokh 95] who used smaller initial crystallites than the steady state size as feed material in the grinding experiments. A growth of the hematite crystals from 10 nm to about 50 nm in size was observed after 2 minutes of high energy milling in a planetary ball mill. Additionally, the crystals were almost spherical in shape. Milling of 5 nm γ-alumina also leads to an increase in the crystallite size to 20 nm accompanied by a phase transition to α-alumina, which is for larger grain sizes the thermodynamically most stable modification [Chen 02].

Planetary ball mills can also be used as mechano-reactors for chemical reactions or mechanical alloying, since they provide the necessary high energy densities. In the group of McCormick, mechano-chemical synthesis reaction are carried out in planetary mills. Therefore, the solid precursor mixture is embedded within a salt matix (e.g. LiCl or NaCl). After reaction, which is caused by impact between the grinding media, the generated nanocrystalline product particles can be recovered by removing the salt through a simple washing procedure. The salt matrix as an inert dilute phase surrounding the reactants allows the formation of finest particles by a reduction of the reaction rate. Particle sizes down to 5 nm for various material systems ranging from pure metals to oxide, carbonate, and sulphite matrials are obtained by this method [Dodd 02], [Tsuz 04].

Moreover, media mills are not only suitable for size reduction and synthesis reactions, but also for delamination processes. If a material holds

a strong anisotropy in its bond forces, a selective size reduction can occur during mechanical stressing. This knowlegde is used to investigate the delamination behavior of graphite particles stressed in a stirred media mill. Especially the question of the smallest possible sheet thickness is in the focus of this work.

2.3. Graphene - properties and production methods

Since the discovery of the 1-dimensional carbon nanotubes (CNTs) by Iijima in 1991 [Iiji 91] and the 2-dimensional graphene sheets by Novoselov and Geim in 2004 [Novo 04], there arised an enormous interest in new carbon nanomaterials having unique electrical, thermal, and mechanical properties. In 2010 Geim and Novoselov were awarded the Noble Prize in Physics "for groundbreaking experiments regarding the two-dimensional material graphene". An overview about the existing carbon allotropes is given in Fig. 2.1.

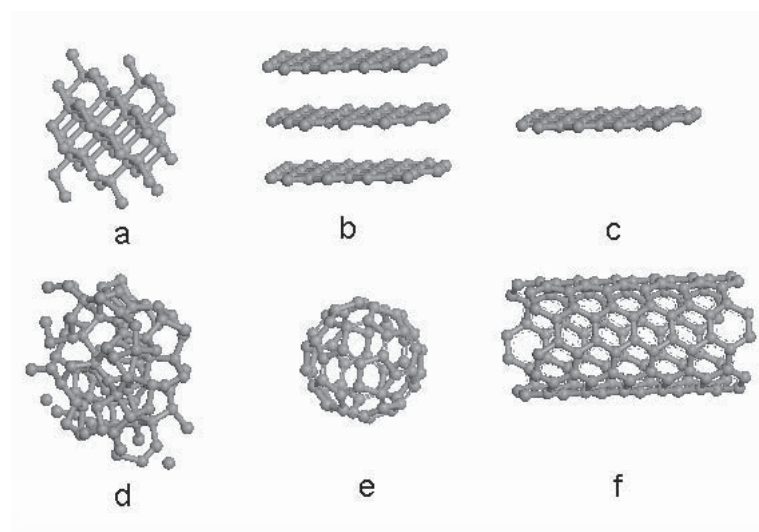Figure 2.1.: Allotropes of carbon: a) diamond, b) graphite, c) graphene, d) amorphous carbon, e) C_{60} (Buckminsterfullerene or buckyball), f) carbon nanotube [Sun 10]

Beside the 3D modifications diamond, graphite, and amorphous carbon, there exist the 2D allotrope graphene, the 1D carbon nanotubes, and the 0D fullerenes. Graphene is a one-atom-thick planar sheet of sp^2-bonded carbon

26

atoms that are arranged in a hexagonal lattice. In contradiction to the former state of the art manifested by Landau and Peierls, that 2D crystals are thermodynamically unstable, free-standing graphene monolayers can be produced nowadays [Stan 06a]. Meyer et al. showed by TEM studies that the suspended graphene sheets are not perfectly flat, but exhibit an intrinsic roughness, which is assumed to stabilize the 2D structure at finite temperatures [Meye 07]. The first graphene monolayer was proven by the group of Novoselov and Geim at the University of Manchester with a simple Scotch tape method [Novo 04]. Single graphene sheets were cleaved from a highly oriented pyrolytic graphite (HOPG) plate with an adhesive tape and pressed onto a silicon wafer with a defined thickness of SiO_2. Due to interference effects with the Si-SiO_2-substrate, even graphene monolayers become visible in an optical microscope [Blak 07]. Common techniques to detect single graphene layers are Raman spectroscopy, scanning probe, and transmission electron microscopy.

The remarkable properties of graphene are summarized in a publication of Ruoff [Park 09]. So far, high values of the Young's modulus (~ 1 TPa, [Lee 08]), fracture strength (130 GPa, [Lee 08]), thermal conductivity ($\sim 5000\ Wm^{-1}K^{-1}$, [Bala 08]), and electron mobility ($> 200000\ cm^2V^{-1}s^{-1}$, [Bolo 08]) have been reported, accompanied by an enormous specific surface area of 2630 m^2g^{-1}. Additionally, a single graphene layer shows an optical adsorption of only 2.3 % in the visible [Nair 08] and NIR [Mak 08] range and yield fascinating transport phenomena such as the quantum Hall effect [Zhan 05]. This makes graphene a promising candidate for applications in many technological fields such as sensors, composites, supercapacitors, transparent conductive films, or solar cells [Geim 07], [Stan 06a], [Stol 08], [Wang 07]. Graphene is known to be a zero-gap semiconductor. Recently, it was demonstrated that the band-gap is tuneable by an adsorption of specific molecules or tailoring its geometry to nanoribbons [Balo 10], [Han 07].

In the graphite crystal, graphene layers are stacked parallel with an interatomic distance of 0.335 nm. Whereas the carbon atoms within a graphene sheet are covalently bound, only weak van der Waals forces are acting between the sheets. As a consequence of this structure, a strong anisotropy of the material properties such as thermal and electrical conductivity or

mechanical strength results. The latter enables the production of graphene layers by cleavage from thicker graphite specimens and is utilized in many fabrication routes. Although there has been intensive research on the preparation of graphene monolayers in the last few years, a large-scale and low-cost production of the new 2D carbon material still remains challenging. The existing production routes can be separated into chemical intercalation methods, growth methods, and mechanical exfoliation methods.

Chemical intercalation and subsequent exfoliation

Most of the described methods to fabricate graphene sheets are based on the intercalation of oxygen or other intervening atoms or molecules between the graphite layers and subsequent thermal or mechanical treatment. Usually, graphite is oxidized to graphite oxide (GO) in the presence of strong acids such as sulfuric or nitric acid. The intercalation compounds enlarge the distances between the graphene layers so that the attractive van der Waals forces are drastically reduced and an exfoliation is facilitated. In a subsequent thermal treatment, the dried GO is heated rapidly ($>$ 2000 °C/min) to 1050 °C. Exfoliation takes place when the decomposition rate of the oxygen groups exceeds the diffusion rate of the evolved gases and the resulting pressure overcomes the van der Waals forces [McAl 07]. Solution-based methods mainly describe the subsequent exfoliation of the intercalated graphite by mechanical forces applied by ultrasound or even simple stirring [Stan 06b]. However, the removal of the intercalation compounds is necessary to regain the excellent properties of the pure carbon material. In particular, the electrical conductivity of GO is strongly reduced compared to the pristine graphite. The reduction of the GO can be realized either thermally or chemically, but it was shown that a complete removal of oxygen is difficult [Schn 06], [Stan 07].

Growth methods

Another approach, which is favored if large graphene areas are requested, is their growth either by chemical vapor deposition (CVD) or epitaxial on SiC surfaces. The latter is based on the higher vapor pressures of Si compared to C, so that silicon sublimates at heating temperatures of about 1300 °C

28

in ultrahigh vacuum causing a thin carbon layer to remain on the surface [Berg 04]. In CVD processes, an active catalytic polycrystalline metal (Ni, Pt, Co, Ir, Ru) substrate is heated (to 900 - 1000 °C in the case of Ni) and exposed to a diluted hydrocarbon flow under ambient pressure resulting in a growth of a single- or multilayer graphene film on the metal surface [Rein 09], [Kim 09].

Mechanical exfoliation

The strong anisotropy of the bond forces in the graphite crystal enables the mechanical exfoliation of graphene sheets as shown with the scotch tape method by Novoselov and Geim. As the interlayer distances in pristine graphite are very small, higher net forces are required to overcome the attractive forces compared to the intercalated material. The group of Coleman focuses on the exfoliation of graphite particles by means of ultrasound in an aqueous surfactant solution or certain organic solvents such as n-methyl-pyrrolidone [Hern 08], [Loty 09]. A yield of monolayer graphene of about 1 %, which corresponds to a concentration of 0.01 g/l, could be achieved with their method so far. Englert et al. presented the exfoliation of mono- and multilayer graphene sheets by means of sonication in aqueous solution and their stabilization with a perylene-based detergent [Engl 09].

Thin graphite nano-sheets were obtained by mechanical shearing of graphite suspensions in a mortar grinder [Anti 06] and a planetary ball mill [Jano 02] [Mile 08]. In both described methods, a selective size reduction was observed leading to a flaky shape of the graphite sheets down to a thickness of about 6 nm. Besides a pure delamination, also a significant in-plane-fracture of the sheets was observed.

3. Theoretical Background

3.1. Wet grinding with stirred media mills

3.1.1. Fundamentals in stirred media milling

Ball mills are used in different fields of industry for comminution, dispersing, and disruption purposes of different inorganic or organic feed materials. They belong to the class of comminution machines with loose grinding media. In stirred media mills, the grinding beads are agitated by a stirrer in a stationary cylinder, which can be arranged either horizontally or vertically. The first proposals to perform a wet grinding task using an agitator in a fixed milling chamber filled with grinding media were made by Klein and Szegvari in 1928. The industrial breakthrough of this technology occurred when DuPont put its "sand mill" into operation in 1948. During the operation the grinding chamber is filled up to 90% with grinding beads, which can consist depending on the desired application of steel, glass, ceramics, or plastics. The size of the beads is typically in the range between 0.1 mm and 3 mm. The energy input is generated by an agitator, which can be a pin or disc rotor, for instance. Compressive and shear (i.e. friction) forces between the moving grinding beads allow a size reduction of the product particles with milling time. Stirred media mills can be operated in batch mode or continuously. The continuous mode can be realized either as pendulum mode, where the suspension is pumped from one vessel through the mill into another one and backwards or as circuit mode, where the suspension is pumped continously through the milling chamber and a vessel. Different operation modes lead to different residence time distributions of the suspension in the mill and affect thereby the width of the particle size distributions. To prevent a discharge of the grinding media out of the milling chamber, the outlet is equipped with cutting slits or sieving cartridges. In centrifugal

separation systems, the sieving cartridge is fixed in the axial center of the rotor so that plugging of the sieve by grinding beads or thick feed particles can be avoided due to centrifugal forces. As a consequence, smaller beads down to 50 μm can be used to fulfill the comminution tasks nowadays. Especially for nano-milling applications, small grinding media are known to be more effective than larger ones. Theoretical investigations of Blecher showed that about 90 % of the inserted energy is dissipated in 10 % of the milling chamber volume, which is located close to the outer endings of the stirrer discs and the wall [Blec 96]. During the grinding treatment, about 99 % of the inserted energy is dissipated into heat. Hence, the grinding chambers are typically equipped with double walls for cooling. According to Kwade, the main stressing mechanism in a stirred media mill is the collision of milling beads moving with different velocities. Since the tangential velocities are usually much higher than the radial and axial velocities, the movement in the tangential direction is the most relevant for breaking the product particles [Kwad 99].

Fundamental investigations on operating parameters, flow fields, scale-up laws, and attrition behavior in stirred media mills were carried out extensively at the Institute of Mechanical Process Engineering / Institute for Particle Technology in Braunschweig and are described in the work of Stehr, Weit, Stadler, Bunge, Thiel, Blecher, Joost, Kwade, Becker, Theuerkauf, Stender, Mende, and Breitung-Faes.

3.1.2. The concept of stress energy and stress number

Effectively, only a small portion of the energy consumed by the stirrer reaches the product particles. Whereas one part is transferred to the grinding media in terms of kinetic energy, the other part is transferred to the product suspension and is dissipated into heat by friction processes. Additional losses of the remaining kinetic energy emerge due to the displacement of fluid during the approach of two grinding beads and deformation processes at their impact. Nevertheless, investigations of Stehr [Steh 82] and Weit [Weit 86] showed that the grinding result is mainly influenced by the specific energy input (energy supplied to the milling chamber related to the product mass). Later on, the grinding media size was also found to

32

have an influence on the achieved particle sizes. In 1996, Kwade introduced the characteristic parameters stress energy SE and stress number SN of the milling beads to describe media milling processes [Kwad 96]. The stress energy is proportional to the kinetic energy of the grinding beads. Since the exact velocity distribution of the grinding media is unknown, the circumferential speed of the stirrer v_t is used to calculate the stress energy of the grinding media:

$$SE_{GM} = \rho_{GM} \cdot v_t^2 \cdot d_{GM}^3 \tag{3.1}$$

A few years later, Becker extended the equation from Kwade and introduced the stress energy of the product particles SE_P [Beck 01]. This number describes the part of the stress energy which is transferred to the product particles. Becker considered energy losses caused by the elastic deformation of product particles and grinding media. Based on the equations of Hertz, Becker extended Eq. 3.1 by including the ratio of the Young's moduli of grinding beads and product particles:

$$SE_P = \rho_{GM} \cdot v_t^2 \cdot d_{GM}^3 \cdot \left(1 + \frac{Y_P}{Y_{GM}}\right)^{-1} \tag{3.2}$$

The stress number describes the average number of stress events of each particle in a batch grinding process and shows the following dependency for comminution, i.e. actual breakage:

$$SN \approx \frac{\varphi_{GM} \cdot (1 - \epsilon)}{(1 - \varphi_{GM} \cdot (1 - \epsilon)) \cdot c_V} \frac{n \cdot t}{d_{GM}^2} \tag{3.3}$$

where n is the number of revolutions of the stirrer, t the comminution time, φ_{GM} the filling ratio of the grinding media, ϵ the porosity of the grinding media bulk, and c_V the volume concentration of the feed. If all particles in the mill are taken into account, the product of stress energy and stress number is proportional to the mass specific energy input E_m.

$$E_m \approx SE \cdot SN \tag{3.4}$$

In order to achieve the same product fineness, two of these three parameters have to be constant [Kwad 02]. Based on experimental findings, rela-

tionships between median particle size and stress energy at constant specific energy inputs are obtained. As shown in Fig. 3.1, an optimal stress energy SE_{opt} exists at which the comminution process is energetically favorable.
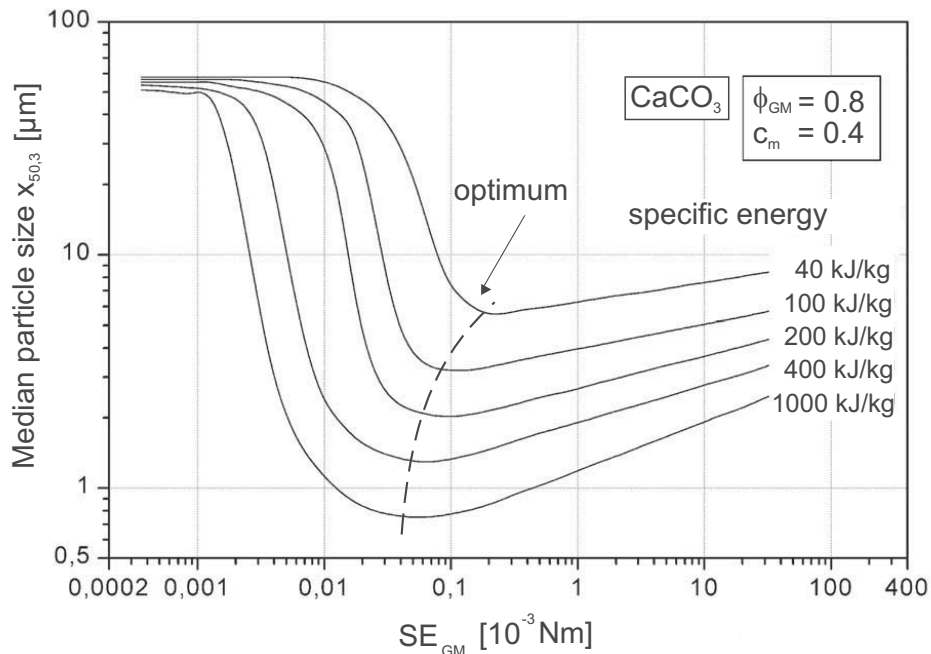

Figure 3.1.: Comminution results as a function of stress energy for different E_m [Kwad 96]

If the stress energy is too low for breaking the feed particles, no grinding progress will take place at all. At higher stress energies than necessary for breakage, the stress number is reduced at a constant energy input. In other words, to reach the same particle size as with SE_{opt}, higher specific energy inputs are required. With smaller particle sizes, the optimal stress energy is shifted to smaller values because smaller particles need less net energies for fracturing. Mende confirmed in his experimental investigations that the concept of stress energy and stress number is still valid in the nanometer range [Mend 04b].

3.1.3. Stabilization methods

As already mentioned above, the stabilization of the particles during the grinding treatment is an improtant factor to obtain well dispersed nanopar-

34

ticles in a liquid medium. Although the breakage of the particle is in first approximation not influenced by agglomeration effects, the suspension stability has a great influence on the final properties. For example, optical properties like transparency or the rheological behavior of the suspension strongly depend on the quality of stabilization as shown by Stenger [Sten 03]. In Fig. 3.2 an overview of different stabilization methods is given. Generally, particles can be stabilized electrostatically due to unipolar charging of the particles, sterically, if (macro)molecules adsorb on the surface, or electrosterically, if these molecules contain additionally charged groups.

a) electrostatic stabilization   b) electrosteric stabilization   c) steric stabilization
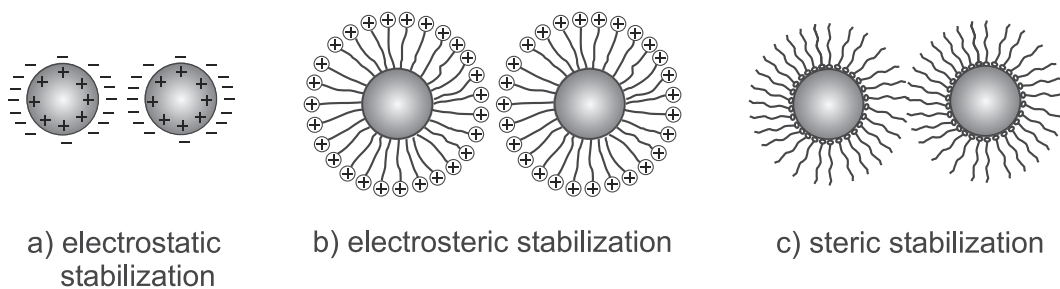
Figure 3.2.: Overview of different stabilization methods

In aqueous systems, the most suitable method is electrostatic stabilization. Surface charge is generated for mineral oxides, which are in the focus of this thesis, by protonation and deprotonation of hydroxyle groups as a function of the pH in the solution. An electrostatic double layer consisting of a rigidly attached Stern layer and a diffuse layer is formed around the particles and contain a huge amount of counter-ions for charge neutralization reasons. Depending on the charge density of the particle surface and the ionic strength of the surrounding media, repulsion forces emerge that have to overcome the attractive van der Waals forces interacting between the particles. In order to predict the stability of an electrostatically stabilized suspension, the DLVO (after Derjaguin, Landau, Verwey and Overbeek) theory can be used [Derj 41], [Verw 48]. The DLVO theory is based on the superposition of particle-particle interactions such as the attractive van der Waals forces, the repulsive electrostatic forces, and the Born repulsion originating from an overlap of electron clouds at very small distances. The total energy as a function of the interparticle distance show a maximal value, the energy barrier, which has to be overcome by approaching particles to

35

coagulate in the primary minimum. If the energy barrier is lager than 15 kT and exhibits a sufficiently steep decline, i.e. large repulsive forces, the suspension is considered to be stable [Laga 97]. In nonpolar media with low dielectric constants, an electrostatic stabilization becomes more and more difficult. On the one hand, only few hydrophilic surface groups are formed in the nonpolar medium, which can be protonated or deprotonated in order to generate surface charge. On the other hand, the overall ion concentration in the medium is extremely small, so that an electrostatic double layer can hardly be formed. Therefore steric stabilization is preferred for such systems. The main idea of this stabilization method is the adsorption of macromolecules or even mono- or oligomers onto the particle surface, which act as spacer between the particles. If the adsorbed molecules contain charged groups, additional electrostatic forces emerge increasing the overall stability of the suspension.

Stabilization simultaneously to grinding operations in media mills is often a challenging task and much more complicated than in unsheared systems. Beside the stabilization against perikinetic agglomeration (Brownian motion) also the stabilization against orthokinetic agglomeration (hydrodynamic forces) has to be ensured. Hence, the repulsion forces have to be larger than the acting shear forces. These considerations are discussed in more detail in related literature (e.g. Husband and Adams [Husb 92]). The grinding operation can also cause problems when using steric stabilizers, since adsorbed molecules may be rubbed from the surface by the grinding media or they even get destroyed during the milling treatment [Somm 07].

Stabilization with surfactants

If the particles surface is inert as in the case of carbon materials, the surface has to be chemically modified to allow an electrostatic or steric stabilization. Another possibility is the stabilization with surfactant molecules. Surfactants consist of a hydrophilic and a hydrophobic part, which make them attach to interfaces. Usually, the surfactant molecules physisorb onto the interface in an adsorption-desorption equilibrium and lower the interface tension between the two phases. Depending on the presence of ionic groups in the hydrophilic part, surfactants can be classified as ionic or non-ionic. If the concentration of free surfactant molecules (monomers) in the bulk

solution exceeds a critical value (critical micelle concentration, cmc), the surfactant molecules start to form clusters (micelles) due to thermodynamic reasons. Depending on the type and concentration of surfactant as well as the solution conditions (temperature, pH, ionic strength), the micelles can bear different sizes and shapes. If the concentration of free monomers fall below the cmc (this is for instance the case when new interfaces are generated), micelles dissolve until the cmc in the bulk is reached again (see Fig. 3.3). Further interactions can result between micelles and stabilized particles especially if ionic surfactants are used [Rose 04].
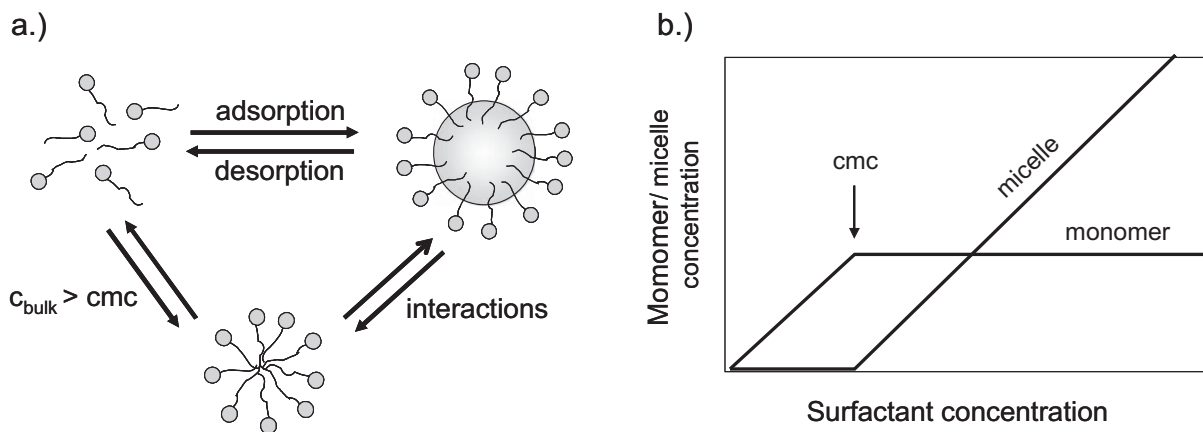

Figure 3.3.: Stabilizing with surfactants: a.) interactions between free monomers, micelles and adsorbed molecules b.) monomer and micelle concentration as a function of surfactant content

Below the cmc, the monomer concentration increases with increasing surfactant concentration until the critical micelle concentration is reached. Further added surfactants are only consumed for micelle formation. Hence, the concentration of micelles increases, whereas the monomer concentration in the bulk solution remains constant. During a grinding experiment, the total surface area is increasing with milling time, so that the equilibria are changing continuously. The coverage of surfactant molecules on the particle surface can be determined by means of adsorption isotherms. From the adsorption isotherms, the necessary amount of stabilizer can be calculated for every available surface area.

3.2. The particles' microstructure

3.2.1. Defect structures in crystalline matter

The elastic limit of a defect-free solid is usually referred to as the "ideal" or "theoretical" strength. The theoretical strength can be estimated by the energy necessary to break the atomic bonds in the fracture plane. A rough estimation for the theroretical shear strength is given by $\tau_{th} \approx G/(2\pi)$. However, this ideal value is not found in "real" materials. Here, the strength is typically much lower, which can be ascribed by the presence of lattice imperfections within the solid. These imperfections weaken the material and reduce its strength. Lattice defects can be separated by their dimensional extension as shown in Tab. 3.1.

Table 3.1.: Classification of microstructural defects

DIMENSION	TYPE OF DEFECT	ENERGY (rule of thumb values)
0 dimensional	Vacancy	1 eV
	Interstitial	3.5 eV
	Substitutional	3.5 eV
1 dimensional	Dislocation	4 eV/atom
2 dimensional	Surface	1 J/m^2
	Grain boundary	0.5 J/m^2
	Stacking fault	10^{-3} - 1 J/m^2
3 dimensional	Pore, flaw	-

Since defects distort the crystalline lattice, an elastic stress field is formed close to the defect. The energy increase accompanied by defects is strongly dependent on the considered material. Nevertheless, "rule of thumb" values are also given in the table above [Blum 03]. Different defects predominantly influence specific materials' parameters, e.g. vacancies are important for diffusion and creep, whereas dislocations are mainly responsible for plastic deformation. Other mechanisms of plastic deformation are phase changes, twinning, super plasticity, or creep based on diffusion processes. Nevertheless, dislocation movement and multiplication are regarded as the most important deformation mechanism.
Hence, their characteristics are discussed in more detail in the following.

Dislocations are characterized by two vectors. The line vector describes the pathway of the extra half plane through the lattice and the Burgers vector describes the magnitude and direction of the lattice distortion. Based on the orientation of line to Burgers vector, it can be distinguished between two different types of dislocations: edge and screw. In real materials often mixed dislocation types are found. That means they exhibit both edge and screw characteristics. In Fig. 3.4, an edge and a screw dislocation are presented.
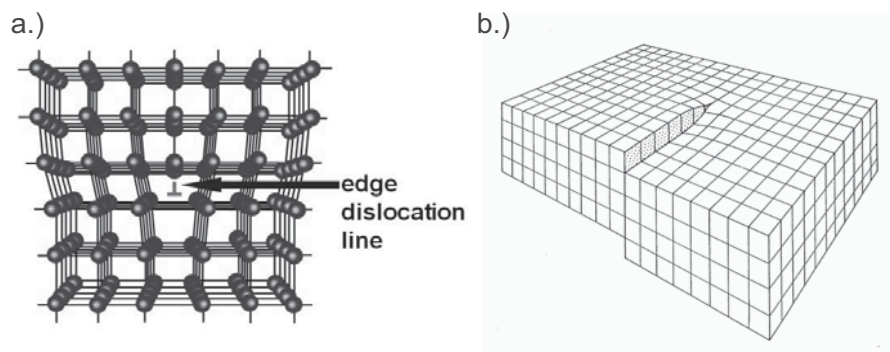

Figure 3.4.: 1 dimensional crystal defects: a.) edge dislocation; b.) screw dislocation

Plastic deformation, e.g. caused by the movement of dislocations, is accompanied by a step by step tearing of atomics bonds in the crystal. The resulting force acting against the dislocation movement is the so-called friction force or Peierls force. The dislocation line disappears if it reaches a free surface. During plastic deformation, the amount of dislocations in a crystal increases. This is caused either by the formation of new dislocations (dislocation nucleation) or a multiplication of present ones. Since very high stresses are required for dislocation nucleation close to the theoretical yield strength, the multiplication mechanism is the more frequent one. Dislocation multiplication takes place at Frank-Read sources according to the Orowan mechanism, which is schematically shown in Fig. 3.5.

A dislocation line is pinned with its outer endings between two obstacles, at which point the inner part starts to bend as a consequence of the applied stress. The dislocation bows further and further until it interacts with itself and forms a new dislocation loop. In addition, the initial dislocation is rebuilt. The necessary stress to multiply a dislocation by the Orowan mechanism can be estimated using Eq. 3.5.
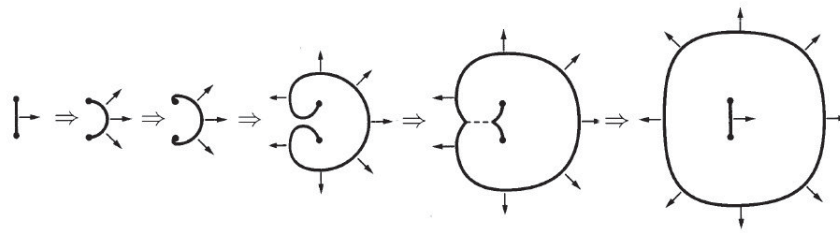
Figure 3.5.: Orowan mechanism [Roes 06]

$$\tau_{Orowan} \approx 0.84 \cdot \frac{G \cdot b}{\Lambda} \tag{3.5}$$

where G is the shear modulus, b the Burgers vector, and Λ the distance between the two obstacles. With decreasing grain size, the maximum available obstacle distance decreases and higher Orowan stresses are necessary to generate new dislocations.

The concept for plastic deformation is not restricted to any specific material class. Dislocations are found even in very brittle ceramics. However, plastic deformation is rarely observed in such materials since low toughness values and high Peierls forces facilitates cracking prior to plastic yielding.

3.2.2. Size effects in nanocrystalline materials

The materials' behavior is governed by its microstructure. In particular, lattice defects and grain size are known to affect the material properties. One important effect of grain size in nanocrystalline solids is the Hall-Petch relationship or grain boundary strengthening/hardening. It describes the correlation between the yield strength of a material σ_y and their grain size d in the following form: [Hall 51], [Petc 53]

$$\sigma_y = \sigma_P + k \cdot \frac{1}{\sqrt{d}} \tag{3.6}$$

where σ_P is the friction stress (Peierls stress) and k is the strengthening coefficient unique to each material. The Hall-Petch relation is based on the observation that grain boundaries impede dislocation movement and that

40

the number of dislocations within a grain have an effect on how easily dislocations can traverse grain boundaries. With decreasing particle size, the amount of surface atoms increase rapidly so that the materials' behavior may differ from the bulk properties. In several experimental and theoretical studies, it was proven that values such as Young's modulus, fracture toughness, or hardness are changing with grain size in the nanometer range [Lata 03], [Mook 07], [Gerb 06].

As already mentioned in chapter 2.2, the whole material behavior can change with particle size. Below a critical size, which is termed the brittle-to-ductile transition x_{BDT}, originally brittle materials start to behave plastically. The reason is the increasing necessary breakage stress with decreasing particle size (smaller initial cracks), so that below the brittle-to-ductile transition size the yield stress of the material exceeds its breakage stress and yielding occurs prior to fracture. Sizes for the brittle-to-ductile transition were found in the lower micrometer and submicrometer range ($SiO_2 \sim 1.1$ μm, $Al_2O_3 \sim 3.3$ μm [Haga 79]; Si $\sim$ 300 - 400 nm [Ostl 09]). As a consequence of the changing material properties with grain size, the fracture behavior is also influenced by size effects in the nanometer range.

Absence of dislocations in smallest grains

It is reported for metal nanoparticles, that below a certain size, the grains contain only very low dislocation densities or may even be free of any dislocations [Vepr 95]. Some explanations are given in literature for this phenomenon ranging from an inability to generate new dislocations in the smallest grains limited by dislocation nucleation [Vale 07] or multiplication [Chri 98] to an instability of dislocation lines. The latter is consolidated by most of the authors referring to the theoretical considerations of Nieh et al. [Nieh 91] (see chapter 2.2) or of Gryaznov et al. [Grya 89], [Grya 91]. Gryaznov et al. ascribe the dislocation instability by an increasing image force acting on the dislocation loop with decreasing grain size. The image force F_i drives the dislocation to the grain surface, whereas a friction force (i.e. the Peierls force F_P) works against the dislocation movement. This competition is illustrated in Fig. 3.6 [Roma 95].
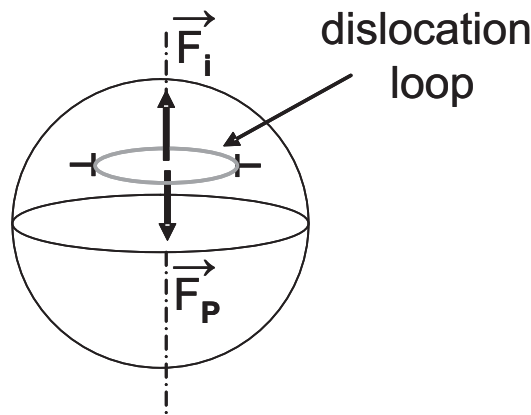
Figure 3.6.: Forces acting on a dislocation loop [Polo 91]

A dislocation loop becomes unstable and spontaneously leaves the grain at its surface when the image stress σ_i exceeds the Peierls stress σ_P. According to Hirth [Hirt 82] the image stress can be determined by the following expression:

$$\sigma_i = \frac{G \cdot b}{4\pi(1 - \nu) \cdot l_{ds}} \tag{3.7}$$

where l_{ds} is the distance of the dislocation line from the surface. In a spherical particle, the maximum distance equals the radius of the particle. Eq. 3.7 shows that the image stress scales inversely with particle size. The Peierls stress does not show any dependency on particle size, but is very sensitive to the nature of the interatomic bond force. From the force equilibrium, the critical grain size can be determined from:

$$d_{crit} = \frac{G \cdot b}{2\pi(1 - \nu) \cdot \sigma_P} \tag{3.8}$$

Characteristic lengths were calculated by Gryaznov et al. for spherical metal particles, Al: 14 nm, Cu: 38 nm, and Ni: 16 nm [Grya 91]. Recently, it was shown in the group of Banfield that the observation of dislocation-free nanocrystals seems to be valid for ceramic nanocrystals as well. In HR-TEM studies of 6 nm titania nanoparticles, no more dislocations could be detected inside the grains [Penn 98]. Also, the elastic properties are found to change below a critical grain size, which is ascribed by the absence of dislocations [Chen 09].

3.3. Particle breakage

3.3.1. General considerations

Understanding particle breakage is an important issue to obtain the desired product in milling processes. A combined knowledge of process design and fracture behavior of the product particles is a necessary precondition to realize optimal process conditions in terms of energy utilization and product quality.

To achieve particle breakage, a sufficiently high amount of energy has to be applied to the product particles either in single or multiple stressing events. The breakage behavior depends on its intrinsic material properties as well as the applied stress conditions. These stress conditions can be classified by type of stress (loading case), number of loading points, stress intensity, and stress rate. According to Rumpf, there exists four different types of stress, which can be separated by the manner in which the energy is supplied [Rump 90]. The four mechanisms are summarized in Fig. 3.7.

Type I	Type II	Type III	Type IV
Compression (+Friction)	Impact	Shear flow	Non-mechanical supply of energy

Figure 3.7.: Stress types according to Rumpf

Different stress types result in different stress fields inside the particles, which are depending on the material properties more or less favorable for fracture. In ball milling applications, only type I is relevant for particle breakage. The product particles are trapped between the grinding media and compressive and friction forces (often termed as shear forces) act on the particles.

Depending on the stress type as well as the material properties, there exist different failure modes. The failure mode of a material can be classified according to Ghadiri as brittle, semi-brittle, or ductile depending on the degree of deformation [Ning 97]. Brittle failure is caused by fracture without any plastic deformation. If plastic flow takes place prior to fracture, the process is termed semi-brittle. This failure mode is often valid for brittle materials, if the stress concentration at the notch root under loading exceeds the yield stress of the material. A plastic zone is formed around the crack tip changing the stress field and the resulting breakage pattern. Ductile fracture is dominated by strong plastic flow. Most of the inserted energy is used for plastic deformation rather than the cracking process.

Influence of material properties

It is well known that the milling behavior of particles depends not only on their intrinsic material properties (material function), but also on the mill performance (machine function). Whereas the machine function in stirred media mills can be well described by the concept of stress energy and stress number (Kwade and Schwedes), the determination of the material function directly from the grinding process is hardly possible, since both functions are interconnected.

Peukert distinguished between different scale levels to describe the material behavior on the breakage propensity [Peuk 04]. On the molecular scale, rupture depends on the break-up of chemical bonds and hence, depends on atomic interactions. One level above the breakage event is characterized by a continuums approach, which is commonly practiced in the field of Materials Science. By means of stress-strain curves, the failure behavior of a standardized sample is described. Characteristic material properties like Young's modulus, ultimate strength, or yield strength can be obtained from these curves. In general, materials can be classified according to their response to an applied stress into brittle, plastic, and visco-elastic materials. The latter show a strong dependence of the breakage behavior on strain

44

rate (e.g. impact velocity) and temperature. The next level closer to the real process comprises investigations of the single particle. The particles are stressed definedly under comparable conditions as in the milling device. The overall particle strength is a function of particle size, morphology, and defect structure. Depending on the stress type, the material, and morphology, a certain stress field arises inside the particles, which causes fracture if the particle strength is exceeded. The last level represents the process itself. Here, it is usually not possible to separate the influence of the material from the machine function. In general, the deeper the level of investigation, the more difficult it is to transfer the results to the real process.

Vogel generated a single master curve from particle stressing experiments, which reflects the breakage probability of different materials based on only two material parameters (f_{mat} and $xW_{m,min}$) [Voge 03]. Later on, Meier et al. correlated these breakage parameters to intrinsic materials properties by nanoindentation measurements [Meie 09].
Ghadiri et al. showed for single particle impact milling of pharamceutical powders that the main influencing material properties for breakage are the Young's modulus Y, the hardness H, and the critical stress intensity factor K_c. These values reflect the resistance of a material to elastic deformation, plastic deformation, and crack propagation, respectively [Ghad 02]. First experiments were carried out where the results from single particle impact tests could be successfully transferred to a dry bulk milling process [Kwan 04].

Energy-size reduction laws

A general relationship between energy and size reduction was given by Walker et al. in 1937 [Walk 37]:

$$dE = -C\frac{dx}{x^n} \tag{3.9}$$

where dE is an infinitesimal amount of energy required to reach an infinitesimal size reduction dx. C and n are constants for a given mill and

45

material system. From the "general grinding law" (Eq. 3.9), a power function can be derived resulting in the following form:

$$x = a \cdot E_\mathrm{m}{}^b \tag{3.10}$$

Validated by various experimental data, this equation describes the size reduction by straight lines in a double logarithmic scale diagram. Beside this general formulation by Walker, more specific theoretical and empirical energy-size reduction equations were proposed by von Rittinger (1867), Kick (1885), and Bond (1952), known as the three theories of comminution. Whereas the approaches from von Rittinger and Kick are derived for single particle models, the equation of Bond can be used for comminution of particle assemblies in media mills. The equation of Walker can directly be transformed into the Bond law for n = 1.5, where the constant is a material specific fit value defined as "work index".

3.3.2. Breakage theories

In 1921, the first considerations about crack propagation under an applied stress field were published by Griffith in *"The Phenomena of Rupture and Flow in Solids"* [Grif 21]. The Griffith concept is only valid for brittle materials already containing at least one microcrack, which is nearly always the case for adequately large particles. The concept is based on an energy equilibrium at the crack tip. To reach a propagation of the crack, the provided elastic energy in the direct surroundings of the crack tip has to be larger than the necessary energy for the creation of new surfaces (differential energy balance). According to Griffith, the crack can propagate throughout the material if the following condition for the breakage stress applies:

$$\sigma > \sigma_B = \sqrt{\frac{2Y\gamma}{\pi c}} \tag{3.11}$$

where γ is the surface tension of the material, Y the Young's modulus and c the maximum crack length existing in the sample. Hence, with smaller particle sizes, smaller maximum cracks pre-exist in the material and higher stresses are required for particle breakage.

46

In experimental investigations, much higher stresses than predicted by the Griffith law were observed to reach fracture of brittle materials. In 1949, Orowan [Orow 49] and later on in 1957, Irwin [Irwi 57] found that a huge part of the inserted energy is consumed for nonelastic deformation processes such as the formation of a plastic fracture zone around the crack tip and microstructural interactions. Only a small portion of energy is used for the creation of new surfaces. This fracture behavior is termed semi-brittle and is the most likely one for brittle materials as well. Hence, reducing the surface energy by changing the surrounding medium or the adsorption of grinding aids cannot have any influence on the breakage energies for such materials as once postulated by Rehbinder [Rehb 72]. The Griffith equation was modified by replacing 2γ by the crack resistance R, which includes all energy consuming processes during crack propagation. Irwin introduced the so-called energy release rate G for plane stress and showed that G = K^2/Y, where K is the stress intensity factor. At the point of instability (fracture), G reaches a critical value G_c which equals the crack resistance R. The corresponding stress intensity factor is the fracture toughness K_c or under plane stress K_{1c}. All processes acting against crack propagation can be summarized in K_{1c}, which describes the resistance of a material against crack propagation. Hence, the fracture stress can be calculated using the following equation:

$$\sigma_B = \frac{K_{1c}}{\sqrt{\pi c}} \tag{3.12}$$

According to Eq. 3.12 particle breakage is facilitated if large inner cracks exist and the material yield a low fracture toughness.

Intercrystalline or transcrystalline fracture

In polycrystalline materials, the crack can propagate either along the grain boundaries (= intercrystalline/intergranular fracture) or through the grains (= transcrystalline/transgranular fracture). The fracture path mainly depends on the energy of the grain boundaries and the cleavage planes. In general, the crack chooses the path of least resistance and hence propagates along the weakest internal interfaces. These interfaces are within a crystal in the case of the transcrystalline fracture cleavage planes. Cleavage planes

are characterized by close atom packings and low surface energies. If the cohesion forces on the grain boundaries become lower than the cohesion forces on the cleavage planes or if there is not a sufficiently high number of slip systems to propagate, intergranular fracture takes place. This fracture type often occurs for brittle ceramic particles. Beside the material properties (e.g. crystal system, grain boundary energy), the crack path is a sensitive function of temperature, strain rate, stress field, and microstructure (grain size, defect structure, grain boundary segregation). Frequently, fracture shows both transcrystalline and intercrystalline components.

3.3.3. Fracture along the length scales

As already discussed in 3.2.2, the properties of a material can change with particle size. Therewith, also the fracture behavior of a particle will change with the dimension of the sample. In Fig. 3.8, the fracture behavior of a brittle particle in different size ranges is illustrated.
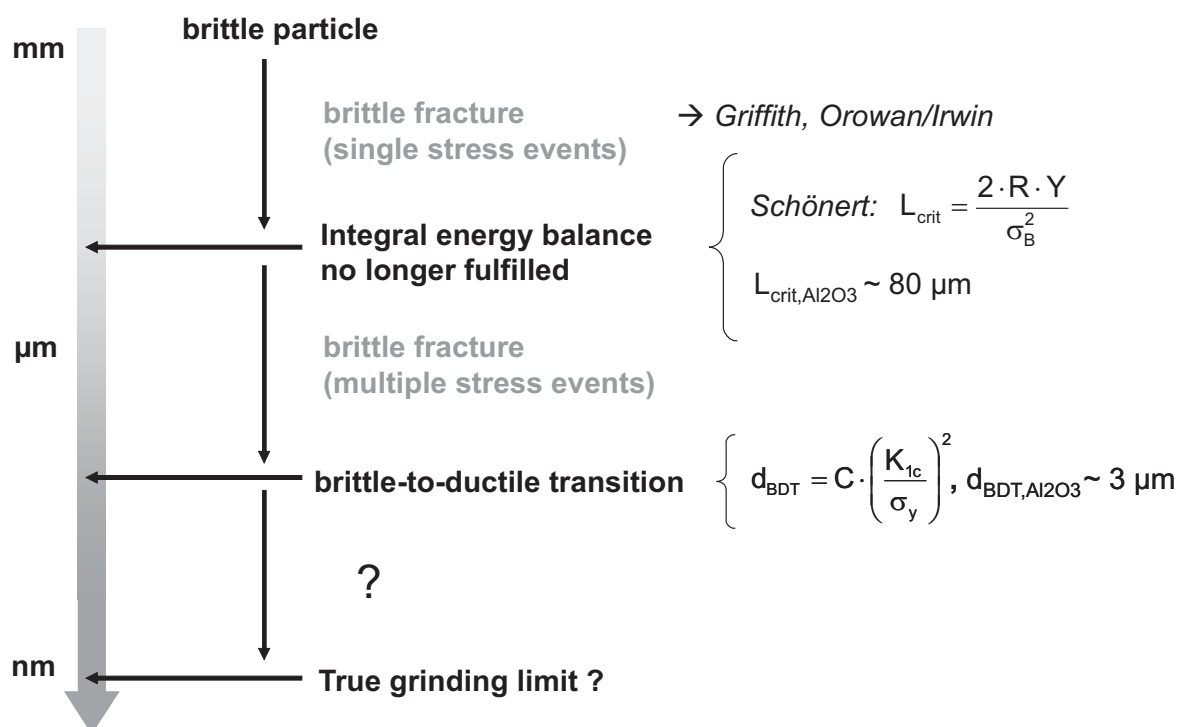

mm

brittle particle

brittle fracture
(single stress events) → *Griffith, Orowan/Irwin*

Schönert: $L_{crit} = \dfrac{2 \cdot R \cdot Y}{\sigma_B^2}$

**Integral energy balance
no longer fulfilled**

$L_{crit,Al2O3} \sim 80 \ \mu m$

µm

brittle fracture
(multiple stress events)

brittle-to-ductile transition $d_{BDT} = C \cdot \left(\dfrac{K_{1c}}{\sigma_y}\right)^2$, $d_{BDT,Al2O3} \sim 3 \ \mu m$

?

nm

True grinding limit ?

Figure 3.8.: Fracture along the length scales

48

For large particle and grain sizes, a brittle material, e.g. a ceramic particle such as alumina, shows a typical (semi-) brittle fracture behavior under loading, which can be described by the Griffith or Orowan/Irwin approach. With decreasing particle size, the particle can hardly store the necessary elastic energy within its volume required for crack motion across the entire particle in one stress event (integral energy balance). If sufficient energy cannot be supplied to the crack tip, the crack stops. Further stress events are necessary to reach breakage of the whole particle. Schönert estimated a critical size below which multiple stress events are required using the following equation [Scho 88].

$$L_{crit} = \frac{2 \cdot R \cdot Y}{\sigma_B^2} \tag{3.13}$$

This equation is based on the Griffith approach for fracturing a cylindrical body with the length L. For Al_2O_3 particles, this critical size is in the range of 80 μm. With decreasing particle size, the breakage stress increases since smaller crack lengths pre-exist in the sample and yielding takes place prior to fracture. A critical size can be defined below which a breakage-free deformation of the specimen occurs under loading. At this size the material behavior changes from brittle to ductile and is accompanied by severe plastic deformation. Hagen gives a brittle-to-ductile transition size x_{BDT} of about 3 μm for alumina particles. However, an exact calculation of x_{BDT} is hardly possible, since the yield strength describes a region rather than an exact value. Nevertheless, particle sizes of alumina much smaller than 100 nm can be achieved in milling processes nowadays [Sten 05b]. Hence, it is assumed that the size reduction below x_{BDT} is accompanied by a strong plastic deformation even for originally brittle materials. For metal particles, a size reduction by a ductile fracture is known. Ductile fracture is characterized by the formation and movement of dislocations resulting in a strong plastic flow of the material. An accumulation of dislocations lead to the formation of new grain boundaries and the nucleation of small voids. Their coalescence can cause crack nucleation followed by its propagation until complete failure of the material. Additionally, hardening effects such as strain hardening (At high dislocation densities, dislocations interact with each other, and serve as obstacles that significantly impede their motion.

As a consequence, the strength of the material increases and their ductility falls.) or grain boundary hardening (Hall-Petch relation) lead to an increase in the materials' brittleness and facilitates fracture. If fracture terminates at a critical size -the true grinding limit-, is still unclear for the time being.

Cyclic loading and fatigue fracture

In Material Science, failure under cyclic loading at stresses lower than the ultimate tensile stress is described as fatigue failure. If the loads are above a certain threshold, cracks will start to form (mainly at sharp edges at the surface or internal microflaws), reach a critical size, and the structure will suddenly fracture. The relation between loading stress and number of cycles to reach fracture is described in the curves of Wöhler (S-N-curve) [Schu 93]. The lower the applied stress, the higher the cycle number until the material fails. Also, the grain size is known to have an influence on the Wöhler lines. With decreasing grain size, higher cycle numbers are necessary to reach fracture. In 1870, Wöhler introduced an endurance or fatigue limit: Below a certain stress amplitude, no further failure of the material is assumed to be observed. However, recent studies of very high cycle fatigue tests reveal that endurance limits do not actually exist or are at least shifted to smaller loads at huge cycle numbers [Hopp 10], [Bath 99].

50

4. Experimental Section

4.1. Experimental setup

4.1.1. Comminution in LabStar LS1

The milling experiments were performed as circuit mode comminution in the laboratory stirred media mill LabStar LS 1 (NETZSCH Feinmahltechnik GmbH, Selb, Germany). The suspension is pumped with a hose pump from the grinding chamber into a stirred vessel, where samples can be taken and stabilizers can be added. From the vessel, the suspension returns into the mill. A schematic overview of the experimental setup is shown in Fig. 4.1.
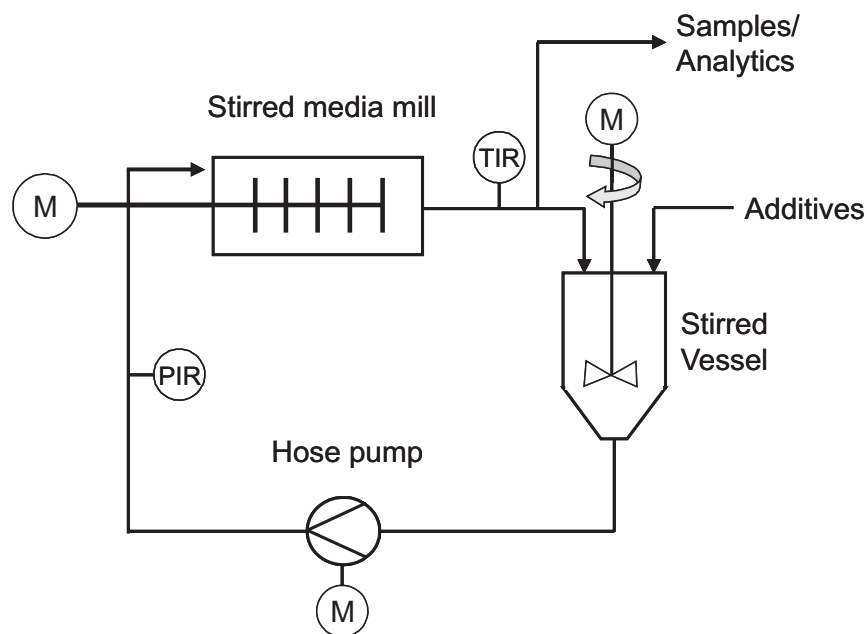
Figure 4.1.: Circuit mode comminution with LabStar LS1
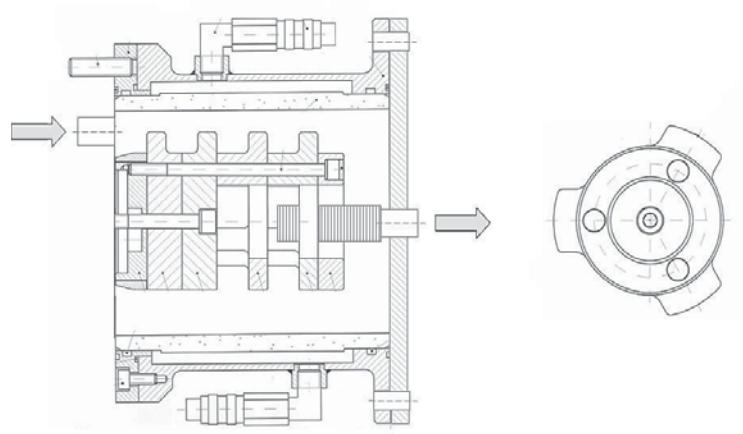
Figure 4.2.: Grinding chamber of LabStar LS 1 and plan view of the pin rotor

The LabStar LS 1 is a horizontally arranged media mill with a rotating pin stirrer. The mill has an explosion-proof design and is equipped with a centrifugal separating system for the grinding media which allows the use of small grinding beads down to a size of 50 μm. The grinding chamber is lined for wear protection reasons with ZrO_2 and offers a total volume of 0.67 l. The rotor is made out of ZrO_2 or Si_3N_4 and has a maximum radius to the outer ending of the pin of 3.8 cm. A schematic drawing of the grinding chamber of LabStar LS 1, and the pin stirrer is given in Fig. 4.2. All experiments were carried out with a filling ratio of grinding beads in the milling chamber of 80 vol.%. The grinding chamber and the vessel are equipped with a double wall for cooling, which is connected to an external cooling water system (FPW55-SL, Julabo, Germany). The rotational speed of the agitator is continuously adjustable with a frequency converter between 1000 and 4500 rpm. The maximal drive capacity of the LabStar LS 1 is 3 kW. The data acquisition was carried out with a LabView 6i program. During the grinding process, the power consumption of the mill P(t) is measured which allows the determination of a mass specific energy input $E_m(t)$ according to Eq. 4.1

$$E_m(t) = \frac{\int_0^t (P(\tau) - P_0)\, d\tau}{m_P} \qquad (4.1)$$

52

where P_0 is the no-load power of the empty mill at a certain revolution speed and m_P is the mass of the feed material.

4.1.2. Delamination in Batch Mill PE 075

The laboratory stirred media mill PE 075 (NETZSCH Feinmahltechnik GmbH, Selb, Germany) has been used for the delamination experiments of the graphite particles. The experimental setup provides a batch mode comminution of the product particles only. The vertically arranged grinding chamber is made of ceramic (Al_2O_3) and has a volume of 0.6 l. To dissipate the generated heat, the grinding chamber is also equipped with a double wall and is connected to an external cooling water system. The stirrer consists of three eccentrically arranged perforated discs made out of Si_3N_4. The rotational speed of the stirrer can be adjusted continuously from 233 to 2100 rpm. The mill provides a maximum drive capacity of 0.25 kW. The design of the batch mill as well as the stirrer geometry is shown in Fig. 4.3.
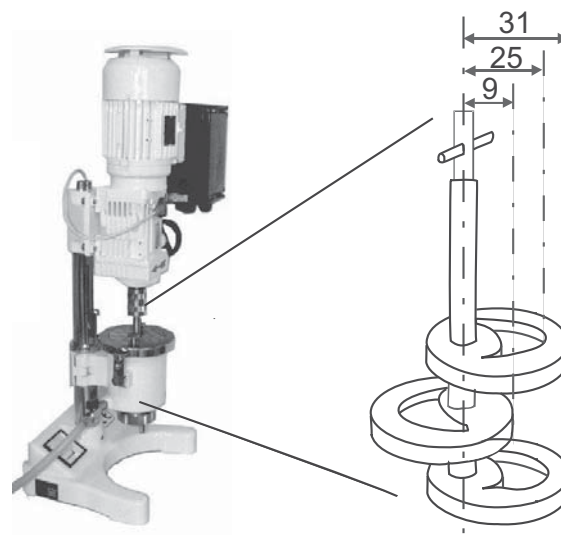

Figure 4.3.: Design and stirrer geometry of batch mill PE 075

4.1.3. Dry grinding in a planetary ball mill

For dry grinding experiments, the planetary ball mill PM 400 (Retsch GmbH, Haan, Germany) was used. In general, planetary ball mills are limited to a batch mode comminution by their design. The used mill is equipped with 4 grinding jars (planets) which are made of steel and offer a volume of 500 ml each. The sun wheel has a diameter of 300 mm and the wheel speed can be adjusted continuously between 30 rpm and 400 rpm. The grinding jars are arranged eccentrically on the sun wheel of the planetary mill. The direction of movement of the sun wheel is opposite to that of the grinding jars in the ratio 1:1.5. The movement of the grinding media in the milling jars result in high energy release rates. Since the jars could not be connected to a cooling system, high temperatures arise during milling and require pause times for cooling.

4.2. Materials and methods

4.2.1. Materials

Milling Material.
To investigate the influence of milling material on the breakage behavior of nanoparticles, different materials were used in the experiments. An overview about the materials with their manufacturers and their initial specific surface areas S_m are given in Tab. 4.1.

Solvents.
De-ionized water and technical ethanol (95 vol.% denatured with MEK, VWR International GmbH, Germany) were used as solvents in the grinding experiments.

Grinding Media.
Wear resistant commercially available yttria stabilized zirconia milling beads (YSZ) in different size ranges from 0.05 mm to 1.25 mm were used as grinding media. According to the manufacturer (Tosoh Corporation, Japan), the beads have a density of 6065 kg/m^3, a Young's modulus of 265 GPa, and a

54

Table 4.1.: Milling materials

MATERIAL	MODIFICATION	MANUFACTURER/ TRADE NAME	DENSITY [kg/m^3]	S$_M$ [m^2/g]
Al_2O_3	α-alumina	Almartis GmbH/ CT 1200 SG	3930	7.6
SnO_2	cassiterite	Merck KGaA	6950	8.2
SnO_2	cassiterite	Keeling & Walker	6950	4.0
SnO_2	cassiterite	Thermox Zinnoxide GmbH/ VS	6950	4.1
SiO_2	quartz	Carl Roth GmbH+Co.KG	2650	1.0
ZrO_2	baddeleyite	Sigma Aldrich Co.	5770	4.3
TiO_2	anatase	Kronos Titan GmbH/ Kronos 1171	3880	8.6
$CaCO_3$	calcite	Carl Roth GmbH+Co.KG	2730	2.0
ZnO	zincite	Sigma Aldrich Co.	5610	4.1
CaF_2	fluorite	Hüttenses-Albertus	3180	2.5
SiC	SiC/moissanite	Struers GmbH	2390	0.3
C	graphite	RMS Remacon GmbH/ GS 6	2300	17.7

chemical composition of 95 % ZrO_2 and 5 % Y_2O_3.

Beside the spherical zirconia beads, an irregular shaped α-alumina split (Cerpass XTL®, Saint-Gobain Ceramic Materials GmbH, Weilerswist, Germany) in a size range between 0.18 mm and 0.3 mm was also used in the milling experiments. This alumina split was produced in a seeded sol-gel process and is highly wear resistant. Compared to the spherical zirconia grinding beads, the costs for the alumina split are about one order of magnitude lower. The alumina grinding media has a density of 3910 kg/m^3 and a purity $\geq$ 99.6 %. A microscopic picture of the split is given in Fig. 4.4.

Dispersing Agents and other Chemicals.

To prevent agglomeration or restacking of the delaminated graphite sheets, the anionic surfactant Sodium Dodecyl Sulfate SDS ($C_{12}H_{25}NaO_4S$, assay $\geq$ 98 %, Fluka BioChemica, Switzerland) was used as received. The necessary amount of stabilizer was determined by an adsorption isotherm.

For the polymer composites, polyvinyl alcohol (PVA, 4-88, Sigma Aldrich Co.) was used as matrix material. The polymer has a molecular weight of about 31000 g/mole, a density of 1.269 g/cm^3, and is 86.7-88.7 % hydrolyzed. Since PVA is also a good stabilizer for aqueous graphite suspensions, the polymer is also used in some grinding experiments.
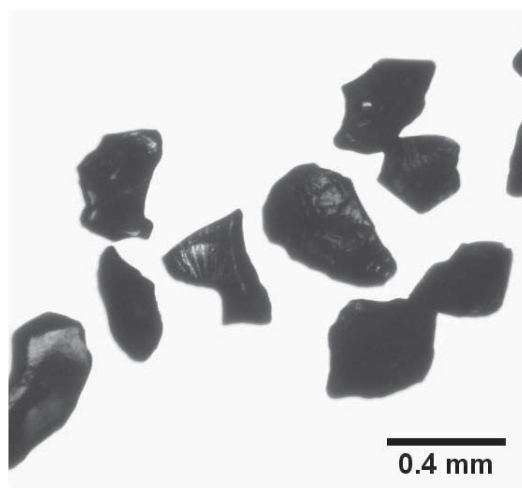
Figure 4.4.: Microscopic image of the alumina grinding media

For the coating experiments of delaminated graphite sheets with platinum nanoparticles and the determination of their catalytic activity, some other materials were needed. The non-ionic surfactant Dodecyldimethylaminoxide (DMAO, Sigma Aldrich Co.) was used as a stabilizer for the aqueous graphite suspensions.

The fabrication of the Pt-NP was carried out by the reduction of potassium hexachloroplatinate(IV) (K_2PtCl_6, VWR International GmbH) with either sodium borohydride ($NaBH_4$, Sigma Aldrich Co.) or analytical ethanol (purity ≥ 99.8 %, VWR International GmbH). The produced Pt-NP could be stabilized with Polyvinylpyrrolidone (PVP, K30, Sigma Aldrich Co.). The catalytic activity of the coated sheets was analyzed by the reaction of p-nitrophenol (Merck KGaA) with $NaBH_4$ under the presence of the Pt-NP to p-aminophenol.

4.2.2. Characterization methods and sample preparation

Atomic force microscopy (AFM). To determine the exact thickness of the graphite sheets, the commercial AFM NanoScope III (Digital Instruments/Veeco, Santa Barbara, CA, USA) was used in tapping mode with MikroMash Ultrasharp NSC15/AIBS cantilevers made out of silicon. The samples were prepared by spin-coating (Spin-Coater SCV, LOT Oriel Group, rotational speed 3000 rpm) diluted suspensions onto cleaned Si or

56

Si/SiO$_2$ wafers. In exceptional cases, the coated wafers were put into a bath of millipore water to remove adsorbed surfactant molecules and subsequently dried under moderate temperatures (T $\leq$ 80 °C).

Contact angle measurements. Surface tension measurements were carried out with the contact angle meter OCA 20 (DataPhysics Instruments GmbH, Filderstadt, Germany) using the Pendant Drop method in order to determine the adsorption isotherm of SDS molecules on graphite particles.

Dynamic light scattering (DLS). Particle size distributions of the milled samples were obtained using the Honeywell Ultrafine Particle Analyzer 150 (UPA, Microtrac Inc., USA), which allows according to the manufacturer a size detection in a range between 3.2 nm and 6.54 μm. The Brownian motion of the particles causes intensity fluctuations of the scattered light (3 mW semiconductor laser, $\lambda = 780$ nm), which can be correlated to a particle size distribution by means of the Stokes-Einstein equation. To avoid multiple scattering, the suspensions were diluted in an appropriate background solution prior to the measurements.

Inductively Coupled Plasma Mass Spectroscopy (ICP-MS). To determine the amount of grinding media attrition in the milled suspensions, ICP-MS measurements (ICP-OES, Spectro Analytical Instruments GmbH, Kleve, Germany) of the dried suspensions were carried out at the Institute of Glass and Ceramics (Department of Materials Science and Engineering, University Erlangen-Nürnberg).

Impedance spectroscopy. Impedance measurements to examine the dielectric properties of the polymer composites were carried out on a Concept 40 Impedance Spectrometer (Novocontrol Technologies GmbH & Co. KG) in a frequency range between 0.01 Hz and 20 MHz. Epoxy resin plates (15 mm x 15 mm) with interdigitated Cu electrodes (channel length = 23.28 cm; channel width = 200 μm; channel height = 18 μm) were used as the substrate for the impedance measurements.

Nitrogen adsorption (BET). To investigate the specific surface area S_m of the milled powders after different grinding times, a gas adsorption analyzer (NOVA 2200e, Quantachrome, Germany) was used. The dried samples were degassed for at least 2 h at 250 °C under vacuum to remove adsorbed solvent molecules. The S_m was determined using the BET (Brunauer-Emmett-Teller) method at 7 relative pressures p/p_0 between 0.1 and 0.4 (standard 7-point method) with nitrogen as the adsorption gas. Under the assumption of spherical and monodisperse particles containing no micropores, S_m can be used to calculate the mean Sauter diameter $x_{1,2}$ using the following equation:

$$x_{1,2} = \frac{6}{S_m \cdot \rho_p} \qquad (4.2)$$

Complete adsorption-desorption isotherms of the final products were additionally recorded to determine the presence of micropores in the material, which can falsify the calculated Sauter diameters. The evaluation of the isotherms was carried out by means of V-t-plots (see Appendix). Also, the roughness on the particle surface can influence the measured surface area. However, since no visible irregularities were found during SEM or TEM imaging on the particle surface, this effect is neclegted in the following.

Raman spectroscopy. Raman spectra of graphite sheets were recorded on a single spectrometer (LabRam Aramis, Horiba Jobin Yvon GmbH, Unterhaching, Germany) using 532 nm laser excitation. The sheets were spread via spin coating on Si-wafers with a 300 nm SiO_2 layer, which enhance the Raman signal of the carbon material.

Rheology measurements. Rheology measurements were carried out on a Physica Universal Dynamic Spectrometer (UDS 200, Paar Physica GmbH, Austria) with double gap geometry according to DIN 54453. The instrument is connected to an external thermostat to ensure a constant temperature during the measurements. To avoid errors due to the shear history of the samples, a constant shear rate of 1000 s^{-1} was applied for 60 s to the suspensions before the flow curves were recorded. The data acquisition was carried out stepwise via ramp function from 1000 s^{-1} to 0.1 s^{-1}. In

exceptional cases the shear rate was increased to a maximal value of 4000 s^{-1}.

Scanning electron microscopy (SEM). Scanning electron microscopy images were obtained using an Ultra 55 field emission SEM (Carl Zeiss NTS GmbH, Oberkochen, Germany) with EDX detector (Thermo Scientific, Dreieich, Germany). The concentrated suspensions were diluted and dispersed in appropriate background solutions before spreading them on cleaned Si-wafers via spin-coating. The prepared wafers were dried under dust free conditions.

Transmission electron microscopy (TEM). TEM was conducted to examine the size, morphology, and inner structure of the particles. The TEM CM 30 and the HRTEM CM 300 UT (both: Philips, Eindhoven, Netherlands) were used in this work. The measurements were carried out at the Center for Nanoanalysis and Electron Microscopy (CENEM; University Erlangen-Nürnberg). Both microscopes were operated at 300 kV using a LaB$_6$ filament. The samples were prepared by pipetting a few microliters of the diluted suspension onto a holey carbon mesh grid.

UV-Vis spectroscopy. The concentration of delaminated sheets in the suspension after removal of the feed particles was determined using optical absorption spectroscopy (CARY 100 Scan, Varian Inc., Palo Alto, USA) at a wavelength of 660 nm. By means of calibration curves, the measured extinction can be related to a defined concentration of carbon particles with the same size and shape.

X-ray diffraction analysis (XRD). The XRD data were collected using a D8 Advance powder diffractometer (Bruker AXS, Karlsruhe, Germany) equipped with a VÅNTEC-1 detector and Ni filter. Cu Kα radiation with a wavelength of $\lambda = 0.15406$ nm was used to determine the evolution of the crystallite sizes during the grinding treatment. The X-ray patterns were recorded in a range from $20° \leq 2\theta \leq 80°$ with a step width of 0.014 °/step and a counting time per step of 1 s. The crystallite sizes which are regarded

in this work as the size of the coherent scattering domains were determined by using the Scherrer equation [Sche 18]:

$$x_{crys} = \frac{K \cdot \lambda}{FWHM(2\theta) \cdot cos\theta} \qquad (4.3)$$

where K is a dimensionless shape factor, which is normally set to 0.9 for crystallites of unknown shape. The given crystallite sizes in this work were determined by an evaluation of at least three different, non-overlapping peaks from the diffraction patterns. The Scherrer equation provides domain sizes as a volume-weighted quantity. Beside the Scherrer equation, a Rietveld refinement was also used to simultaneously determine crystallite size and lattice microstrain. The Rietveld method uses a least squares approach to refine a theoretical line profile until it matches the measured profile. The evaluation was carried out with the commercial software TOPAS 3 (Bruker AXS GmbH, Karlsruhe, Germany; [Balz 99]). A more detailed description of the Rietveld method is given in the appendix. The samples were prepared by pipetting the undiluted suspension onto special low background silicon wafers. The wafers were cut in a way that no additional signal from silicon appears in the diffraction patterns.

X-ray photoelectron spectroscopy (XPS). XPS spectra were measured using a PHI 5600 spectrometer (Physical Electronics Inc., Chanhassen, USA) with a monochromatic Al-Kα X-ray source and a hemispherical capacitor analyzer at the Institute of Surface Science and Corrosion (Department of Materials Science and Engineering, University Erlangen-Nürnberg). For the XPS measurements the samples were dried and afterwards compressed to dense pellets (Zwick Z020, F_{max} = 5000 N).

ζ-potential measurements. ζ-potentials were recorded with the Zetasizer Nano ZS ZEN 3600 (Malvern Instruments GmbH, Herrenberg, Germany) employing the Laser Doppler electrophoresis method. An electric field is applied to the suspension and the resulting particle velocity is directly proportional to the magnitude of the ζ-potential. Since the measurements are limited to only low solid concentrations, the milling suspensions were diluted prior to the measurements.

60

5. Breakage Behavior of Nanoparticles

5.1. The apparent and true grinding limit

The grinding progress in milling experiments is commonly tracked by the evolution of particle size. Thereby, the particle size can be determined by different measuring techniques. The most common ones are scattering or diffraction methods. For nanosized particles, dynamic light scattering is a powerful tool to determine size distributions in terms of a hydrodynamic diameter down to a few nanometers. The BET method is based on the adsorption of gas molecules on the surface of a dry powder. The evaluation with the BET method gives a mass specific surface area from which a surface-weighted mean Sauter diameter can be calculated if the product particles contain no pores at all. Depending on the physical principle of the used method, different measuring techniques can yield different particle sizes. Hence, it is very important to give information about the used method in addition to the measuring result. Nevertheless, comparing sizes from different measuring techniques will give additional information about the analyzed product. In Fig. 5.1 the grinding progress of quartz particles dispersed in ethanol without any additive as stabilizer is presented.

At the beginning of the grinding experiment, both the mean Sauter diameter $x_{1,2}$ determined from BET measurements as well as the median particle size from DLS measurements $x_{50,3}$ decrease with specific energy input. In contrast to $x_{1,2}$, the measured hydrodynamic diameter already reaches a constant value at low energy inputs. No further grinding progress is observed in the remaining milling experiment and a final median particle size $x_{50,3}$ of about 250 nm is achieved. The evolution of the mean Sauter diameter from the BET analysis is quite different. Much smaller particle sizes can be detected with this measuring method, but a plateau in particle size is also reached for long grinding times. The reason for this discrepancy is
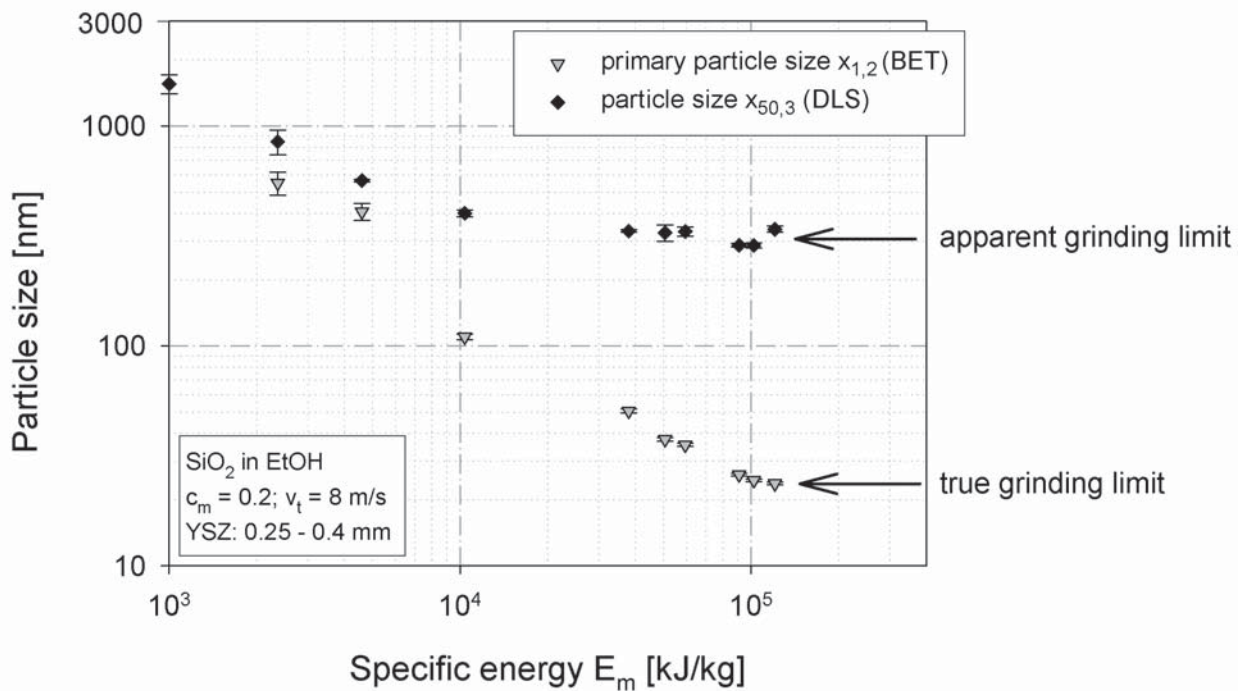
Figure 5.1.: Grinding progress of SiO_2 dispersed in ethanol

the formation of agglomerates, since no stabilizer was added to the milling suspension. Agglomerates are measured by DLS, whereas the BET method gives information about the primary particle sizes and is independent of agglomeration processes. Hence, this method can be used to describe the real breakage process as long as the samples are free of micropores, which enlarge due to the additional inner surface the totally measured surface area. Nevertheless, both methods exhibit a limit in particle size, which is defined in the case of the hydrodynamic diameter as an apparent grinding limit and for the primary particle size as a true grinding limit [Knie 09]. The apparent grinding limit reflects therewith an agglomerate size, which depends on the stability of the suspension and flow conditions inside the milling chamber. Sommer showed in separate agglomeration experiments of Ludox particles in a stirred media mill, that with increasing salt content (i.e. decreasing stability due to the compression of the electrostatic double layer) and decreasing stirrer tip speed, larger final agglomerate sizes are obtained. Larger tip speeds result in the formation of more compact agglomerates,

62

proven with SANS measurements [Somm 07]. Hence, the apparent grinding limit can be shifted to smaller values with increasing suspension stability and should reach the value of the true grinding limit in a perfectly stable system. The true grinding limit is in first approximation not affected by the stability of the suspension. It reflects therewith the size, where no further breakage of the particle occurs. For quartz particles this size is in range of 30 nm. In Fig. 5.2 a SEM image of the milled product in shown.
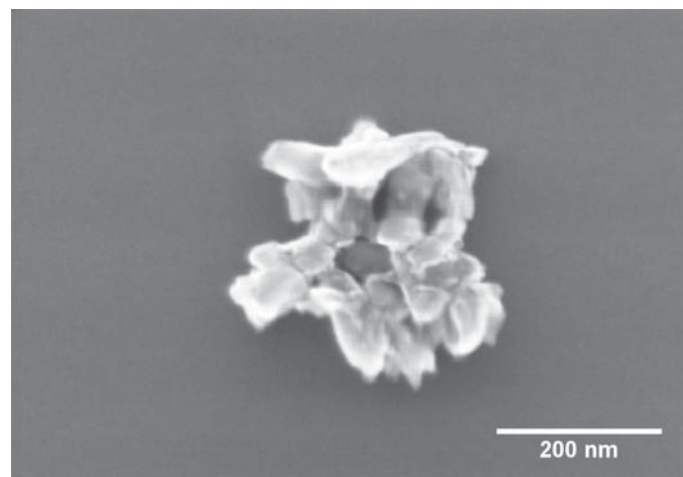
Figure 5.2.: SEM image of milled SiO_2

It can clearly be seen that the broken fragments are highly agglomerated to a cluster of about 300 nm in size, which is in good agreement with the DLS measurements. The primary particles are much smaller and exhibit sizes less than 100 nm. With this first example, it becomes clear that it has to be distinguished between an apparent particle size, which is more or less an agglomerate size and the "real" fragment size (primary particle size). Since particle sizes in comminution experiments are commonly measured by scattering methods, the apparent grinding limit is often misinterpreted in literature as the overall limit of grinding. Moreover, it also seems that fracture itself is a limited process and a true grinding limit exists in the lower nanometer range. These findings will be investigated in more detail in the following chapters.

5.2. The breakage behavior of tin dioxide

5.2.1. Evolution of external structure

In the following, the breakage behavior of nanoparticles is investigated exemplarily for tin dioxide particles, which were chosen as a model system in this study. Tin dioxide (undoped or Sb-doped) has a wide application field not at least for its electrical conductivity (wide energy gap n-type semiconductor (3.6 eV at 300 K)) coupled with a high optical transparency as well as a high chemical and mechanical stability. The n-type conduction in undoped tin dioxide can be related to the presence of oxygen vacancies and tin interstitials leading to a natural nonstoichiometry of the material [Kili 02]. Hence, tin dioxide is extensively used in many applications such as transparent electrodes, solar cells, or other optoelectronic devices [Sund 04]. To achieve sufficiently thin transparant films (0.1 - 1 μm, optical transparancy up to 97 % in the visible range [Kili 02]), small particle sizes are required for film formation in a printing or coating process in order to avoid expensive CVD or ALD methods. In addition, SnO_2 is sensitive towards reducing and oxidizing gases. A change in surface conductivity upon adsorption of gas molecules occurs, which makes tin dioxide an appropriate material for gas sensors.

First of all, the grinding progress of tin dioxide particles dispersed in water is tracked by means of DLS measurements. Since DLS only provides a hydrodynamic diameter, the instrument can be used to investigate the external structural evolution during comminution experiments. The external structure or in other words the size of possible agglomerates is important for further applications, since they determine many properties of the suspension. Stenger found for SnO_2 particles in water the highest zeta-potentials and therewith the highest suspension stability at a pH of 11 [Sten 05a]. This pH value was adjusted in the following experiment, where an aqueous 20 wt% SnO_2 suspension was milled with 0.5 mm to 0.63 mm YSZ grinding media and a stirrer tip speed of 8 m/s. The grinding results are presented in Fig. 5.3.

With increasing specific energy input, the particle sizes characterized by the $x_{10,3}$, $x_{50,3}$, and $x_{90,3}$ values of tin dioxide decrease until a plateau value
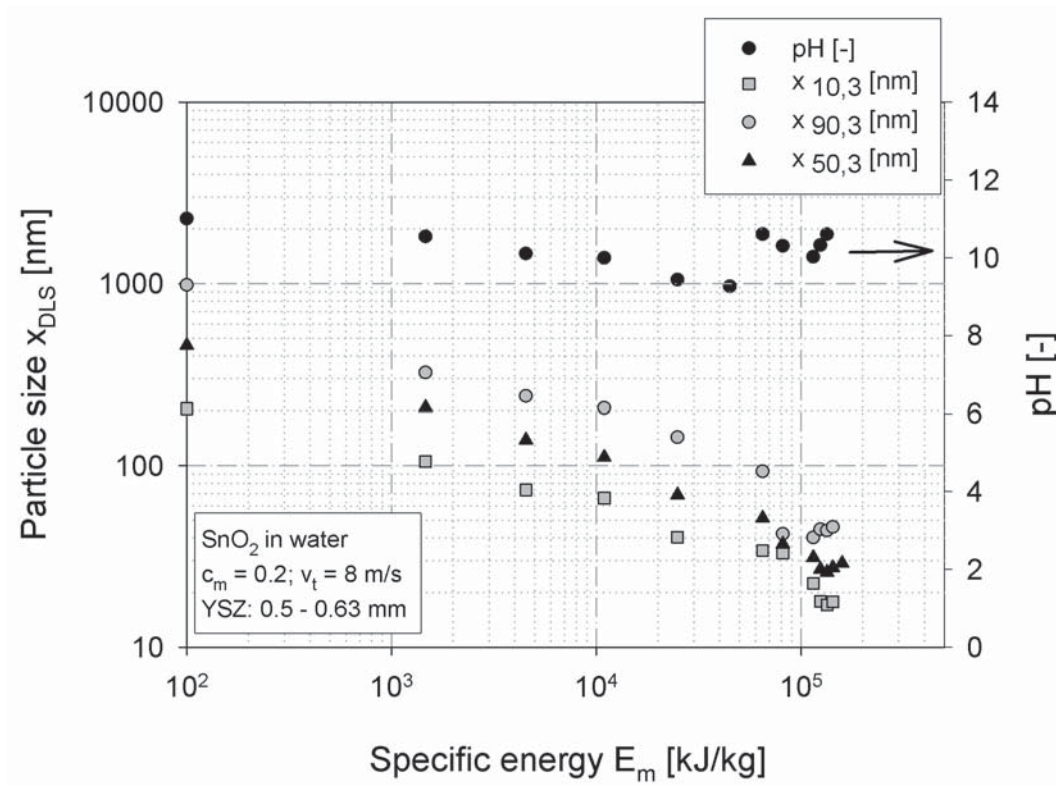
Figure 5.3.: Grinding progress of SnO_2 dispersed in water at pH 11

at a $x_{50,3}$ of about 26 nm and a $x_{50,0}$ of 19 nm was reached. The suspension already yields at these sizes a transparent character, which is enabled by the reduced scattering of fine particles. Even the $x_{90,3}$ value achieved sizes well below 50 nm at high specific energy inputs. It is likely that no agglomerates have been formed in the suspension, which has a zeta-potential of about -50 mV and that the measured sizes reflect the primary particles. DLS measurements provide a hydrodynamic diameter which is the diameter of a sphere that has the same translational diffusion coefficient as the measured particle and depends on the surface structure as well as the concentration and type of ions in the surrounding medium. However, is it difficult to track the true breakage process by means of DLS measurements, since the formation of agglomerates can never be completely excluded. Hence, to investigate the size reduction process exclusively, the primary particle sizes are determined in this study by BET measurements. In Fig. 5.4, a typical evolution of the specific surface area in a long-term milling experiment of tin dioxide

65

is given. Unless otherwise mentioned, the following "standard" grinding conditions apply in the experiments: solid content 10 wt%, YSZ grinding media in a size range of 0.4 - 0.5 mm, stirrer tip speed 8 m/s. At the beginning of the grinding experiment, a steep increase in the specific surface area is observed indicating a fast size reduction. For longer grinding times, i.e. larger specific energy inputs, the increase slows down and a constant value is reached. Under the assumption of monodisperse and spherical particles, a mean Sauter diameter $x_{1,2}$ as a primary particle size can be calculated using the following equation:

$$x_{1,2} = \frac{6}{S_m \cdot \rho_p} \tag{5.1}$$
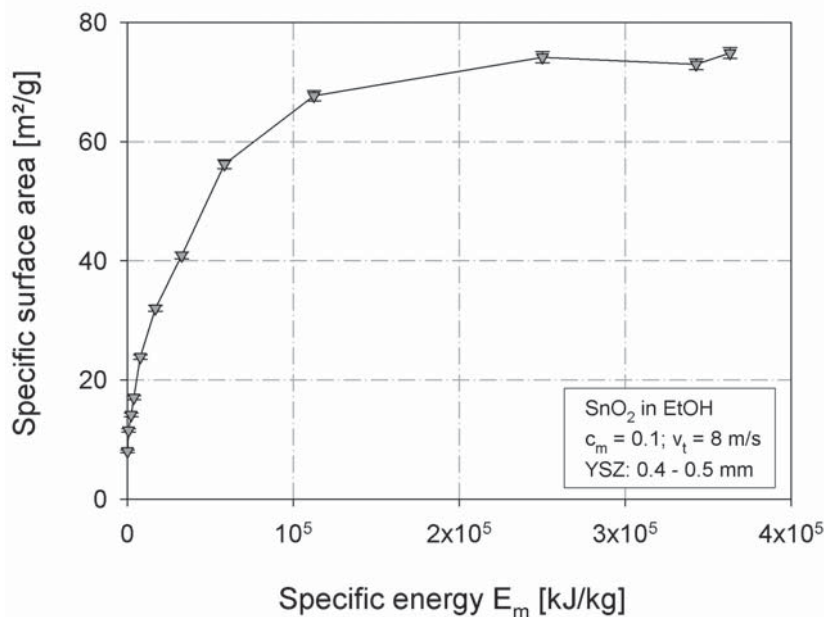
Figure 5.4.: Evolution of specific surface area during comminution of tin dioxide

The evolution of the primary particle size is presented in Fig. 5.5. Since all samples in the double logarithmic diagram lay on a straight line, the breakage behavior of the SnO_2 particles can be described by a power law. Hence, the general predictions of Walker for size reduction processes still seem to be valid for nanosized particles and the breakage follows a first order kinetics. Only the first sample steps out of line, which can be ascribed to

66
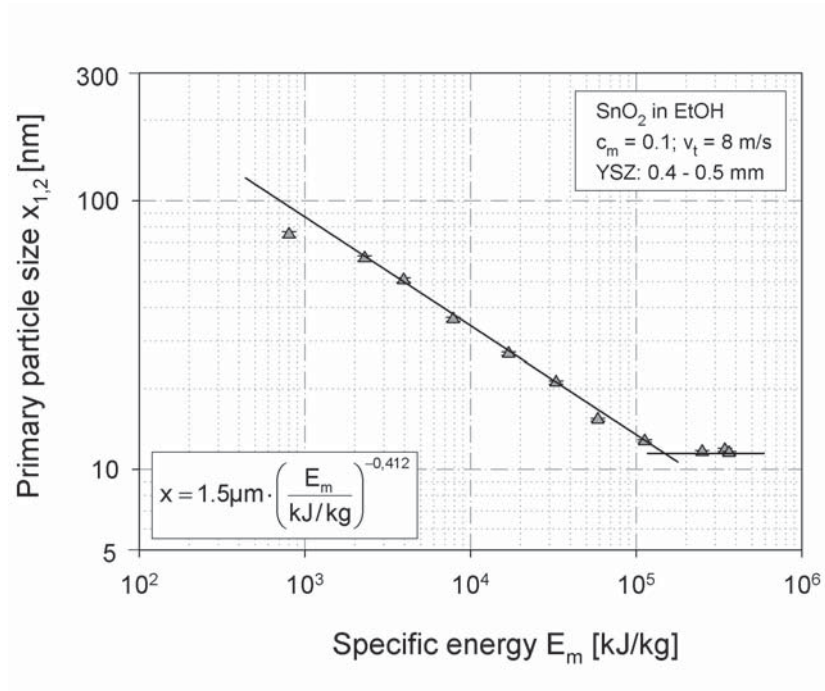
Figure 5.5.: Evolution of primary particle size during comminution of tin dioxide

fluctuations during the starting operation of the milling machine. The first order kinetics is represented by a power law. Fitting the experimental data gives the following dependency for the particle size:

$$x = a \cdot E_m^b = 1.5 \mu m \cdot \left(\frac{E_m}{kJ/kg} \right)^{-0.412} \tag{5.2}$$

For long grinding times, the law of Walker becomes invalid, since size reduction is no longer observed. Although the particles were stressed for another 15 hours, no increase in specific surface area, i.e. no further breakage of the particles is observed. A final primary particle size between 10 and 11 nm is reached for the SnO_2 particles. Hence, a grinding limit also exists for tin dioxide particles. During grinding of tin dioxide, a strong color change from white to dark brown is observed. It is possible that this color change is related to a change in the defect structure (probably the number of oxygen vacancies), which can change the band gap of tin dioxide and therewith change its optical absorption properties [Sun 03]. In the following, it will be investigated how the existence of a grinding limit can

be physically explained and how the limit of grinding depends on process or environmental conditions.

5.2.2. Evolution of internal structure

As internal structure the inner crystalline microstructure of the particles characterized by its crystallite size and defect structure is described. The microstructure evolution during the grinding process can help to understand the breakage mechanism since internal changes in the crystalline lattice take place under stressing prior to particle fracture. A grinding experiment typically starts with polycrystalline particles, i.e. the particles exist of several crystallites which are separated by grain boundaries. During mechanical stressing in the grinding experiment, the particles can break either trans- or intercrystalline and new defects are generated in the lattice. These defects can be point defects, dislocations, or new grain boundaries, which can be formed from accumulated dislocations. Hence, beside a reduction in primary particle size, a decrease in crystallite size as well as an increase in defect density is also expected with milling time. Information about the particles' microstructure can be gained from X-ray diffraction analysis. In Fig. 5.6, X-ray diffraction patterns of tin dioxide at different milling states are presented.

With increasing milling time, a loss in crystallinity due to a size reduction of the coherent scattering domains (in this work termed as "crystallites") and amorphization processes and a broadening of the diffraction peaks is observed. The line broadening can be ascribed by two effects: a decrease in crystallite size and/or an increase in microstrain. The microstrain describes a median change of the lattice parameter in the distorted lattice related to the lattice parameter of the ideal lattice. Defects in the crystalline material lead to a distortion of the lattice, since the interatomic distances are disturbed (compressed or elongated). As a consequence of the distortion, additional elastic energy is stored in the crystallites. A much larger lattice distortion is obtained by the presence of 1-dimensional dislocations compared to 0-dimensional point defects. Therefore, in the following discussions, the role of dislocations as the main distortion mechanism is mainly considered.
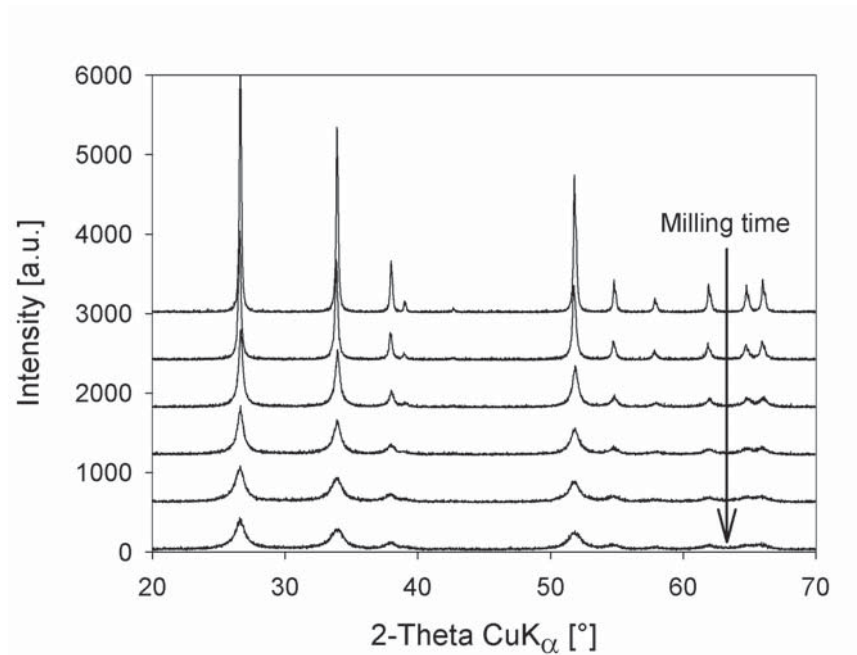
68

Figure 5.6.: X-ray diffraction patterns of SnO_2 at different milling states

X-ray diffraction patterns can be evaluated by different methods. The most common ones are the Scherrer equation, the Rietveld refinement, the Warren-Averbach evaluation, or the Williamson Hall plot. In this work the Scherrer equation and the Rietveld refinement are used to determine the crystalline microstructure. The Scherrer equation (see Eq. 4.3) assumes that the whole broadening of the peak can be referred to a change in crystallite size. The microstrain is not considered in this approach. Hence, the crystallites containing a significant amount of strain will be underestimated in size by using the Scherrer equation.

To investigate both the crystallite size and the microstrain evolution, a Rietveld refinement was used. The possibility to distinguish between size and strain broadening is based on the different dependency of the broadening on the Bragg angle. During Rietveld refinement, which was carried out with the commercial software TOPAS 3.0 (Bruker AXS, Karlsruhe, Germany), the whole pattern is fitted by a theoretical line profile using the least squares approach. The fitted profile can be deconvoluted into Gaussian and Lorentzian contributions representing the size-broadening and the strain-broadening, respectively [Balz 99]. The obtained microstrain from

the TOPAS evaluation can be regarded as an upper-limit strain and is defined as the change of the lattice parameter in the distorted lattice related to the lattice parameter of the ideal crystal ($\Delta d/d$; d: lattice parameter). More detailed information about the Rietveld method is given in the appendix. In Fig. 5.7, the typically evolution of primary particle size, crystallite size, and strain of tin dioxide during a grinding experiment is given.
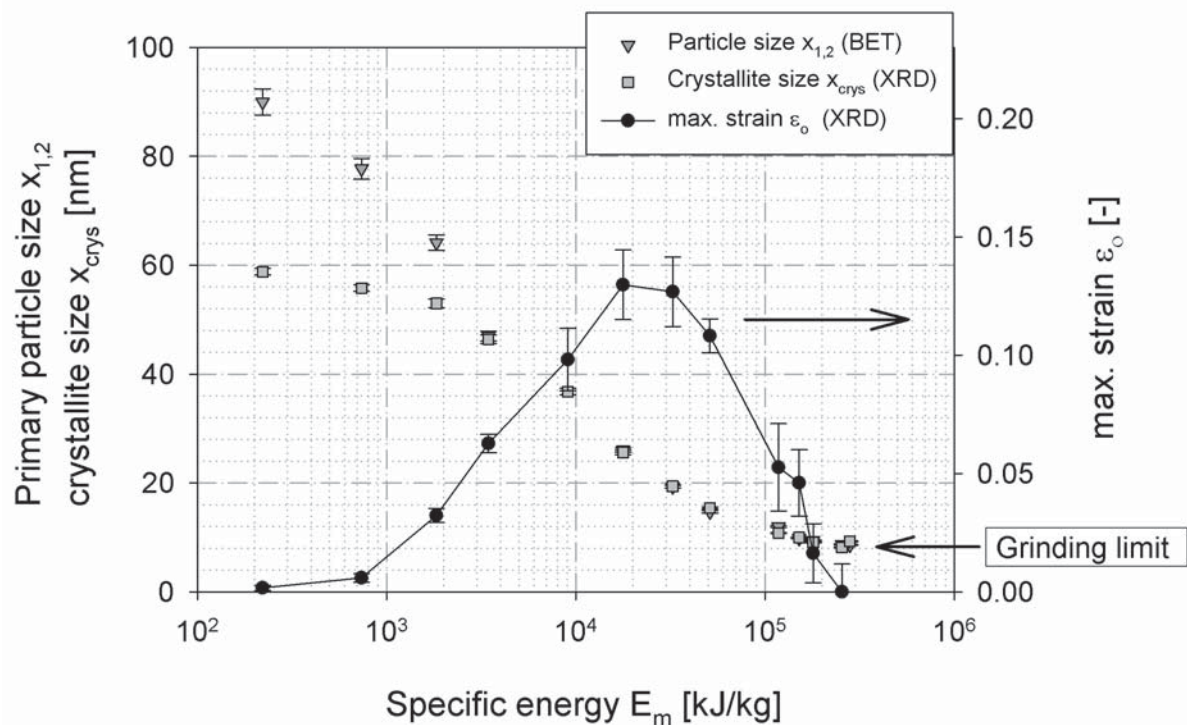

Figure 5.7.: Internal structure evolution of SnO_2 milled in ethanol

As expected, both primary particle size as well as crystallite size decrease with specific energy input until the grinding limit is reached. During the grinding treatment, the initial polycrystalline particles become monocrystalline, indicating a faster primary particle size reduction preferred along grain boundaries. After the monocrystalline stage is reached, further size reduction of the single crystallites takes place. The microstrain increases steeply at the beginning of the grinding treatment, reaches a maximum, and then declines to almost zero. It is worth noticing that the disappearance of the strain takes place almost simultaneously to the achievement of the

grinding limit. Thus, it follows that the presence of microstrain seems to be a necessary precondition for fracturing the nanosized particles. In Fig. 5.8, the evolution of the number of crystallites per particle is illustrated versus the specific energy input.
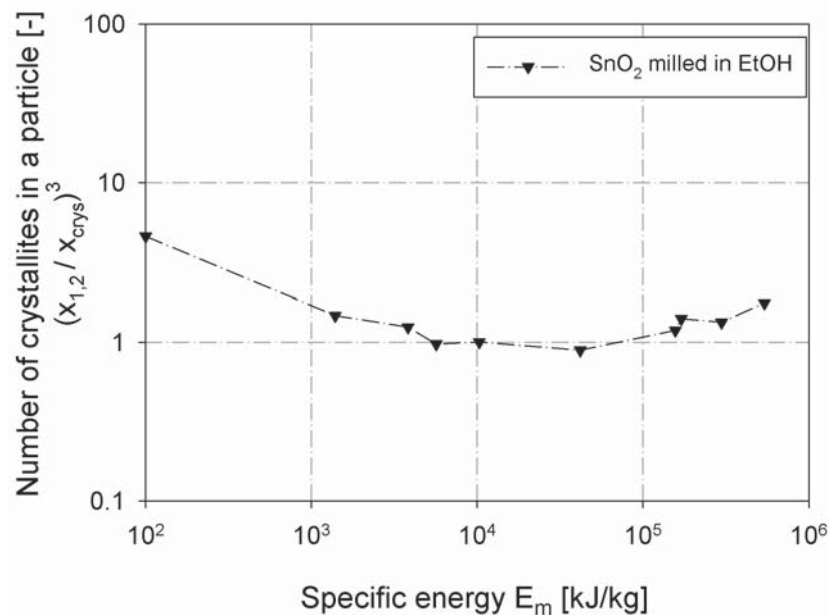

Figure 5.8.: Evolution of the number of crystallites per SnO_2 particle during a grinding experiment

At the outset, each primary particle consists in average of about four or five crystallites. During the grinding treatment, this amount decreases to about one, where the monocrystalline stage is reached. This evolution indicates a preferred intercrystalline fracture along the grain boundaries. For large specific energies, the evaluation predicts a renewed increase in the number of crystallites per particle. This is however, an artefact since an amorphization of the material at long grinding times slightly reduces the crystallite sizes, whereas the primary particle sizes remain constant.

5.2.3. TEM studies of SnO$_2$

Beside the X-ray diffraction analysis, TEM studies were also carried out to investigate the inner structure of the stressed particles. The TEM investigations were carried out by Dipl.-Ing. Mirza Mackovic from the Center for Nanoanalysis and Electron Microscopy (CENEM, University of Erlangen-Nürnberg). First, the initial tin dioxide particles were analyzed by means of HRTEM to investigate possible defects in the structure. A typical image of the feed material is given in Fig. 5.9.
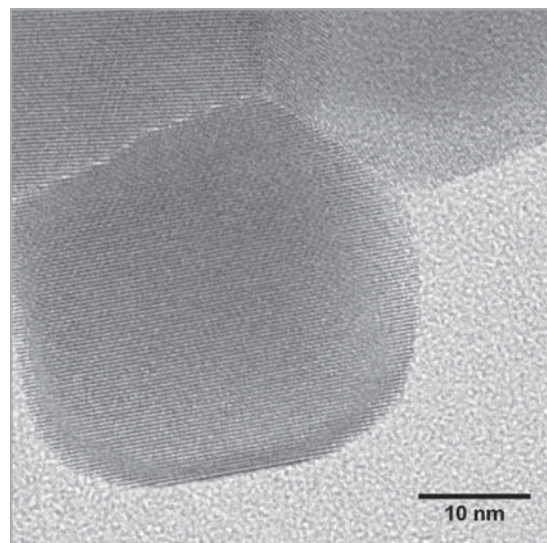
Figure 5.9.: HRTEM image of tin dioxide feed material

It can be recognized that the illustrated feed particle is polycrystalline and consists of several crystallites with a size of about 40 nm. According to XRD analysis, the feed material exhibits a median volumetric crystallite size of about 65 nm. The crystallites are separated by high-angle grain boundaries and seem to be free of defects. Nevertheless, it has to be taken into account, that only a few particles were investigated at each milling stage, so that the results should be interpreted carefully with respect to general statements. It is also possible that some particles in the feed material already contain defects from a pretreatment of the powder. To get more reliable information about the defect structure, statistics should be carried out in future works, which describe, for instance, the amount of defect type per 100 investigated particles at different milling times. In Fig. 5.10, TEM images of SnO$_2$ milled for 1.5 hours are presented.
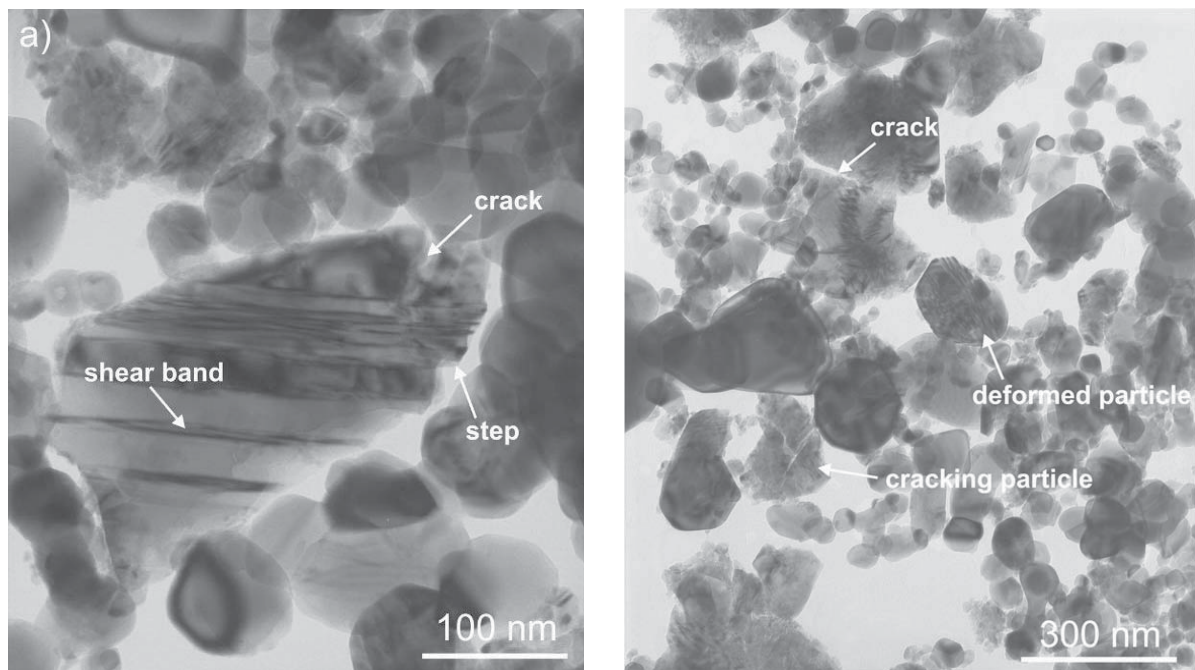
72

Figure 5.10.: TEM images of tin dioxide milled for 1.5 hours

In the sample, highly deformed particles with inner stresses can be observed. In contrast to the brittle bulk material, the nanosized SnO_2 particles behave plastically as expected below the brittle-to-ductile transition size. It is very likely that the achieved particle sizes (≤ 300 nm) are smaller than x_{BDT}, although an exact calculation of the transition size was not possible, because of lacking material data for SnO_2. In many particles, a strong shear band formation was detected (see left image of Fig. 5.10). In the high resolution, some shear bands could be specified as a kind of twin bands, where their outer endings are formed by twin boundaries. Twinning results when a portion of a crystallite gets in an orientation that is related to the orientation of the untwinned lattice in a symmetrical way. The twinned portion of the crystal can be regarded as a mirror image of the initial crystal. The driving force for mechanical twinning is the applied stress (in contrast to growth twins). Mechanical twinning and slip by a dislocation movement can be considered as competing processes for plastic deformation. Twinning generally occurs when the slip systems are restricted so that the twinning stress is lower than the stress for slip. Tin dioxide in the cassiterite phase

yields a tetragonal rutile-type structure, where twinning is often facilitated in distinct directions due to its crystallographic structure. From HRTEM studies described in literature, typical defect structures for SnO_2 such as stacking faults, twin boundaries, or dislocations were identified [Sund 04], [Pan 97]. In the TEM images of the milled SnO_2, partly cracked particles were also found in the samples. Crack propagation is assumed to proceed stepwise, because the necessary energy for a complete spontaneous fracture cannot be stored in the particles' volume below a critical size anymore. In Schönerts words, the integral energy balance is no longer fulfilled and multiple stress events are required for nanoparticle breakage. Therefore, the fracture process can be regarded as a kind of fatigue mechanism. Due to the lack of flaws inside smallest crystallites, fracture can also start at sharp edges at the surface of the particles, where high local stresses are acting during impact. By means of high-resolution TEM, some other defects like 2-dimensional stacking faults can be identified as shown in Fig. 5.11.
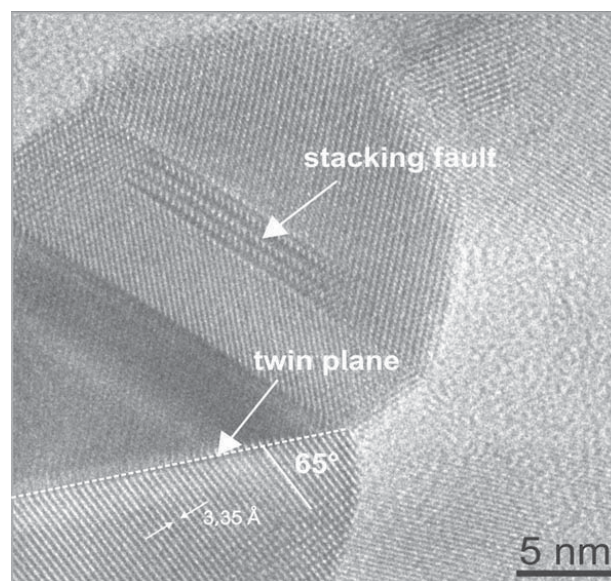

Figure 5.11.: High-resolution TEM image of tin dioxide milled for 1.5 hours

To facilitate the detection of defects, the method of the inverse Fast Fourier Transformation (IFFT) can be used. Therefore, a Fast Fourier Transformation (FFT) of a HRTEM image is accomplished and in the resulting diffraction pattern, two opposite spots are selected, which represent

a certain crystallographic plane. After all other spots were covered with a mask, an inverse image from the FFT pattern is created. This image only displays the selected plane and defects (only in this plane!) can be visualized. In Fig. 5.12, a HRTEM image (of the same particle as illustrated in Fig. 5.11, but with a lower magnification) with the related IFFT image are presened. In the IFFT image, a dislocation line in the crystal plane can be identified.
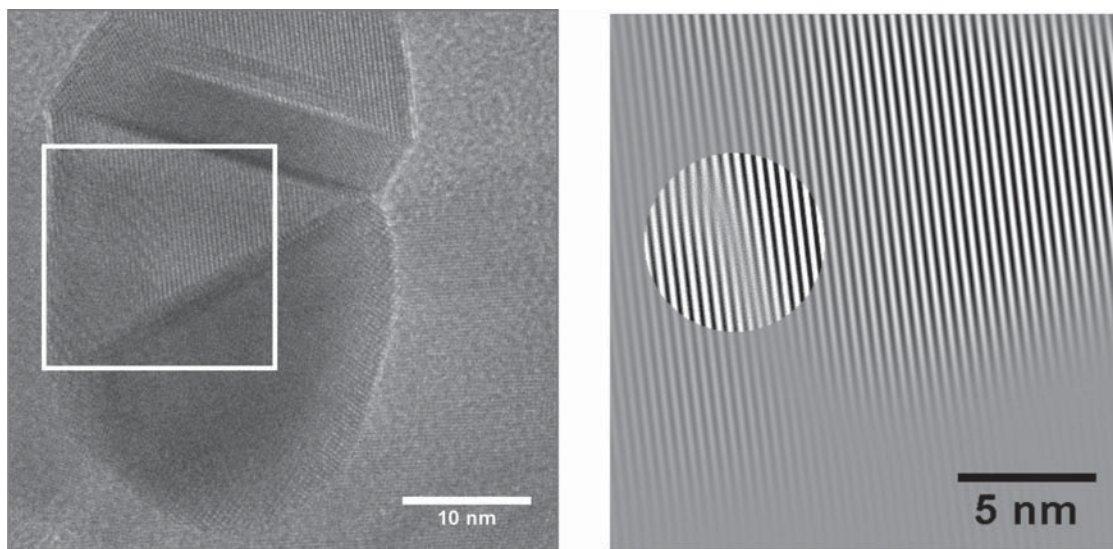

Figure 5.12.: High-resolution TEM of milled SnO_2 (left) and IFFT image showing a dislocation line (right)

The evolution of the particles' microstructure under loading is also investigated by means of Molecular Dynamics simulations at the Institute of Particle Technology by M. Sc. Patrick Armstrong. In Fig. 5.13, the microstructure of a 30 nm tin dioxide particle after compression between two flat punches is given [Arms 09]. Beside two Hertzian cones in the contact zone between particle and flat punch, the formation of twin bands in the direction of maximal shear stress (45°) can be observed. These MD results properly reflect the experimental findings in the microstructure of stressed tin dioxide particles. Further similarities between experiment and simulation were found during milling of CaF_2 particles. Therewith, MD simulations become a powerful tool to predict the microstructural evolution during mechanical stressing and can help to gain new insights in fracture processes.
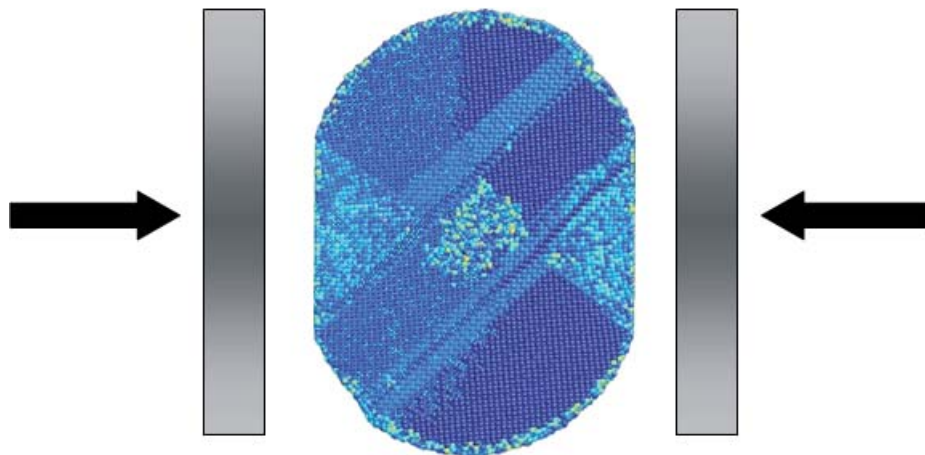
75

Figure 5.13.: MD simulation of a 30 nm SnO_2 particle after compression [Arms 09]

At long grinding times after reaching the grinding limit, the finest crystallites were also analyzed by HRTEM (Fig. 5.14). Due to the lacking stabilization, the crystallites are highly agglomerated. Defects could not be detected in the finest crystallites having a size between 5 to 10 nm. The TEM investigations are therewith in good agreement with the XRD results. Earlier studies from Fecht et al. show that long-term high-energy milling of metal particles lead to the formation of almost dislocation-free grains. The authors assume that at this stage, further refinement of the grains is impossible. They explain this phenomena by the high stresses required for dislocation movement in very small crystallites that hinder further plastic deformation of the grains and therewith further size reduction [Fech 90].
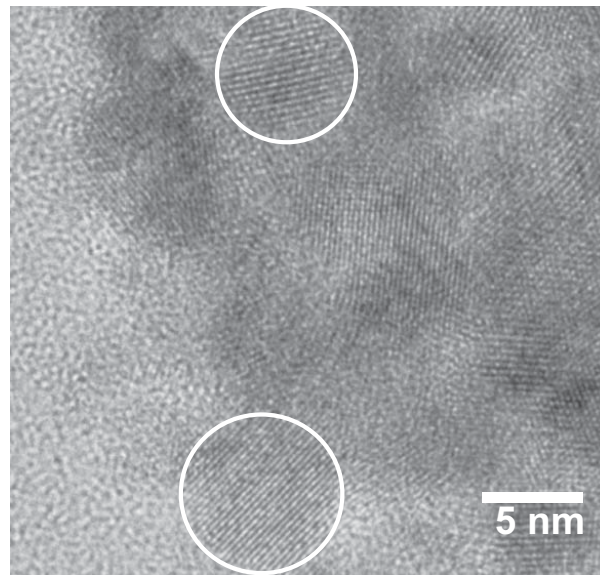
Figure 5.14.: HR-TEM image of SnO$_2$ milled for 24 h

5.2.4. Breakage mechanism of tin dioxide

According to the TEM and XRD studies, the following breakage mechanism (see Fig. 5.15) is assumed to apply for nanosized tin dioxide particles under cyclic loading. Energy is applied to the initial polycrystalline particles in terms of repeated impact between the grinding media. The resulting stress inside the particles is consumed on the one hand for fracturing the particles and on the other hand for microstructural deformation processes. Beside twin bands and stacking faults, the presence of dislocations could also be detected. Lattice defects, especially the 1-dimensional dislocations compared to twin boundaries or point defects, significantly raise the free energy inside the crystallites. During the cyclic loading, further fracture becomes possible due to the following reasons:

- defects accumulate to new grain boundaries or micro voids which can act as nuclei for crack generation,

- at high dislocation densities their movement is hindered so that higher stresses are required for further deformation (strain hardening). As a consequence of the lower ductility, higher stresses can be built up in the material allowing further fracturing,

- defects in the crystal enhance the elastically stored energy, which can be used in addition to the transferred energy from the grinding media for crack propagation.
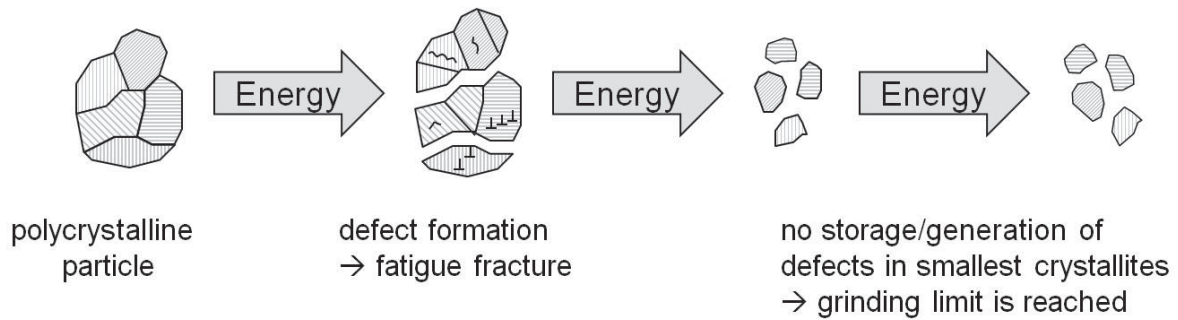

Figure 5.15.: Schematically concept of SnO_2 size reduction in the nanometer range

Below a critical grain size, which equals the primary particle size since tin dioxide becomes monocrystalline during the grinding process, defect structures can hardly be identified in the smallest crystallites. The obtained defect-free grains should yield a strength in the dimension of the theoretical strength of ideal materials. Only the surface of the particles can be regarded as an irregularity. At sharp edges, a stress concentration can originate during impact, which may theoretically cause further crack propagation. However, this mechanism is also limited. Several discussions have been carried out in literature about the low defect density in small crystallites. Whereas point defects are still observed in crystals in the dimension of only several nm, the presence of crystal twins or dislocations is assumed to be size dependent [Yu 10], [Grya 91]. This dependence can be explained by either a lack of defect generation or their instability below a critical size. The absence of dislocations is mainly related to an instability below a critical size. Thereby two mechanisms can apply:

The smaller the crystallites, the shorter is the distance of the dislocation line to the surface, which results in an increase of the image force driving the dislocation line to the crystallite surface. If the image force exceeds the Peierls force of the material, a spontaneous movement of the dislocation line takes place and it disappears at the surface. This theory was first introduced by Gryaznov et al. [Grya 89] and adopted by several other authors [Hebe 06], [Chen 09]. A very similar explanation for the dislocation

78

instability is given by Nieh et al. [Nieh 91]. This explanation is based on the minimal separation distance of two dislocations under equilibrium conditions caused by the repulsive forces between the two defects. Eckert et al. and Banfield at al. used the considerations of Nieh in their calculations [Ecke 92], [Penn 98]. Banfield was the first person who calculated a miminal grain size for the dislocation instability in ceramic particles. The author found a limiting size for titania particles of about 8 nm, which could be confirmed by experimental findings.

Some other groups argue that no dislocation multiplication can occur in the smallest crystallites since Frank-Read sources no longer exist in such crystals or the required stresses to reach a bowing of the dislocation line between two very close obstacles cannot be reached anymore [Chri 98]. Nevertheless, the activation of dislocations at surface sites should be possible even in the smallest crystallites.

Investigations concerning twin formation or their stability reveal that the formation process is strongly dependent on crystal size. Yu et al. found for titanium alloy pillars that the plastic deformation process changes from mechanical twinning to ordinary dislocation plasticity below a critical size [Yu 10]. In addition, the required stresses for the activation of a twin nucleus show a strong exponential increase with decreasing grain size as published by Meyers et al. [Meye 06]. No hints concerning an instability of crystal twins are given in literature. Hence, it can be assumed that the twin formation is the limiting process and the existing twin bands at larger grain sizes vanish when the crack crosses along the twin boundaries.

In the following sections the influence of process and environmental conditions on the above presented breakage behavior and the grinding limit is analyzed. The investigations are focused on the questions whether the value of the grinding limit can be shifted to different plateau levels and if the grinding process can be controlled in a way to achieve this limit with lower energy effort.

5.3. Influence of feed material

To prove if the breakage behavior of tin dioxide as presented in Fig. 5.7 is influenced by the initial microstructure of the particles or impurities in the powder, the milling behavior of tin oxide from three manufacturers with different initial mean particle and crystallite sizes (see Tab. 5.1) was studied. The grinding results under the same process conditions are presented in Fig. 5.16.

Table 5.1.: Tin dioxide feed materials used in this work

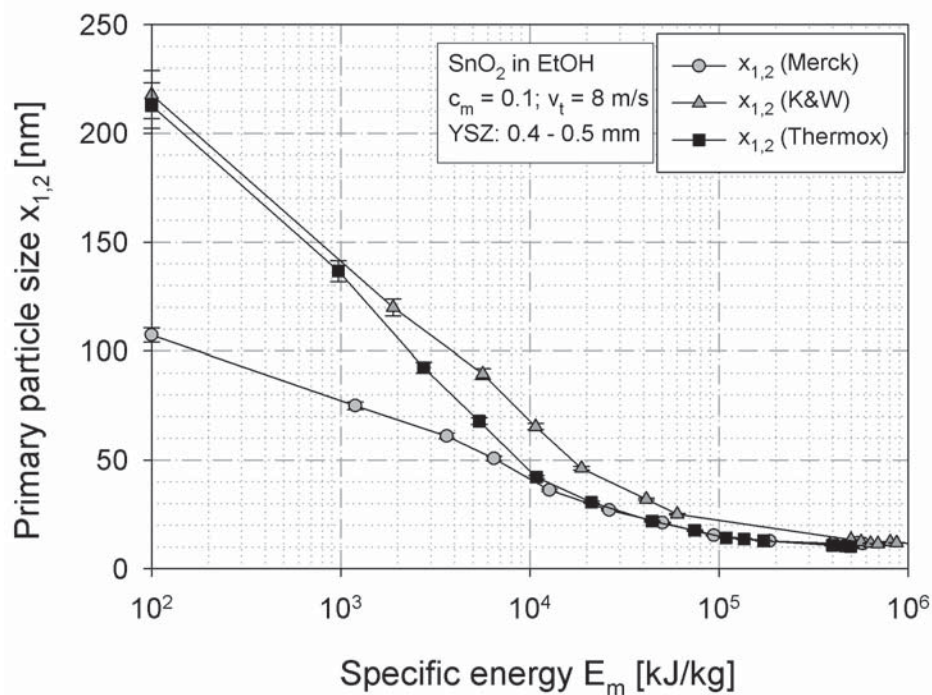| MANUFACTURER	PRIMARY PARTICLE SIZE	CRYSTALLITE SIZE	PURITY
Merck	105 nm	65 nm	$\geq 99.0\ \%$
Keeling & Walker	216 nm	81 nm	$> 99.8\ \%$
Thermox	211 nm	52 nm	$> 99.8\ \%$

Figure 5.16.: Influence of different feed materials on breakage behavior of SnO_2

Independent of the initial primary particle size, crystallite size, or purity, all three feed materials end up at the same particle size of about 10 nm at

the end of the milling experiments. Hence, the grinding limit is not affected by the quality of the initial powder as long as the same crystallographic material is used. Differences in the breakage behavior are observed in the kinetics of size reduction, i.e. the change of particle size with specific energy input. Starting with larger feed particles leads to a faster size reduction, since larger particles break energetically more favorable compared to smaller ones since larger particles exhibit statistically larger flaws which reduce the necessary breakage stress according to Griffith's law. Not only the overall particle size determines the breakage behavior, but also the inner microstructure. The powders from Keeling & Walker and Thermox have nearly the same initial primary particle size but different crystallite sizes. A closer look at the evolution of particle and crystallite size is given in Fig. 5.17.
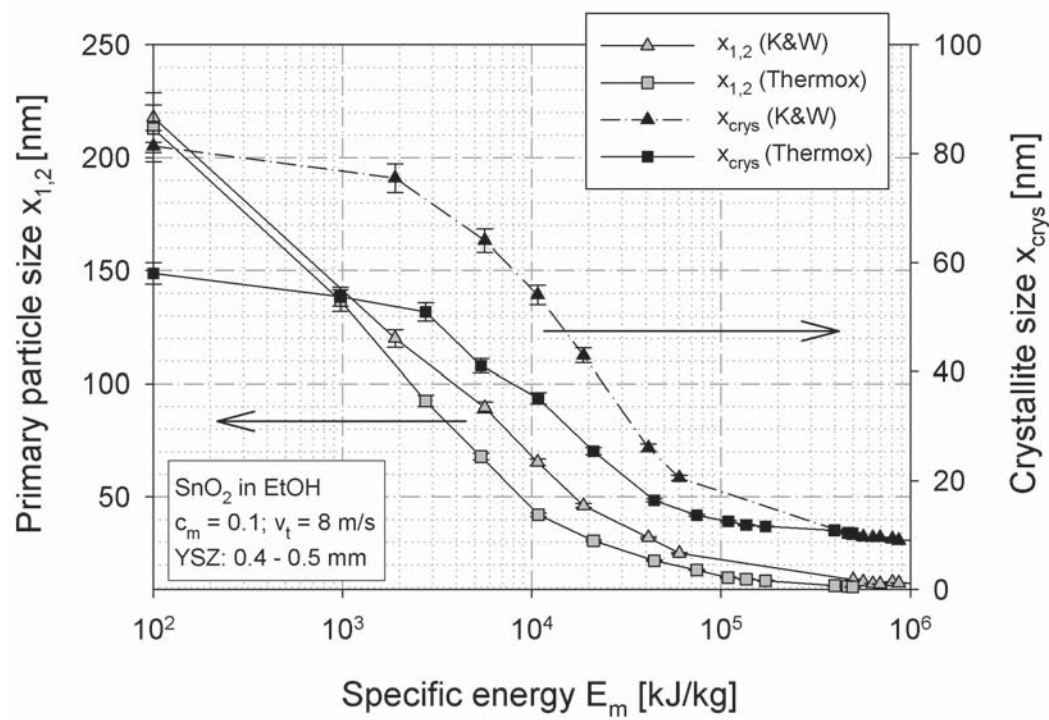

Figure 5.17.: Influence of initial microstructure on breakage behavior of SnO_2

The powder with the finer microstructure (Thermox) shows a slightly larger breakage rate than the Keeling & Walker powder although they yield the same primary particle sizes. This effect can be ascribed by the higher

number of crystallites and therewith grain boundaries. As tin oxide breaks preferably at the grain boundaries (intercrystalline fracture is dominated in tin oxide as shown above), a faster size reduction is observed until the particles become monocrystalline.

5.4. Influence of process conditions

In the following sections, the influence of various process and environmental conditions such as grinding media size, stirrer tip speed, suspension viscosity, or temperature on the breakage behavior of tin oxide is investigated. The main focus of attention is put on the questions, if the grinding limit can be shifted towards larger or smaller values and how the breakage kinetics can be influenced so that the grinding limit is reached with less energy input.

5.4.1. Influence of stress energy

Beside the specific energy input, the most important parameters on the grinding result in media milling are the stress energy SE and the stress number SN. Since the product of stress energy and stress number is proportional to the mass specific energy input, the same grinding result is observed, if two parameters are kept constant. The stress energy is a measure for the kinetic energy of the grinding media and can be calculated using the following equation:

$$SE = \rho_{GM} \cdot v_t^2 \cdot d_{GM}^3 \tag{5.3}$$

As the stress energy is directly coupled with important process parameters, the influence of stress energy is investigated by changing stirrer tip speed and grinding media size in the following. The grinding results are summarized in Fig. 5.18 [Knie 11a].
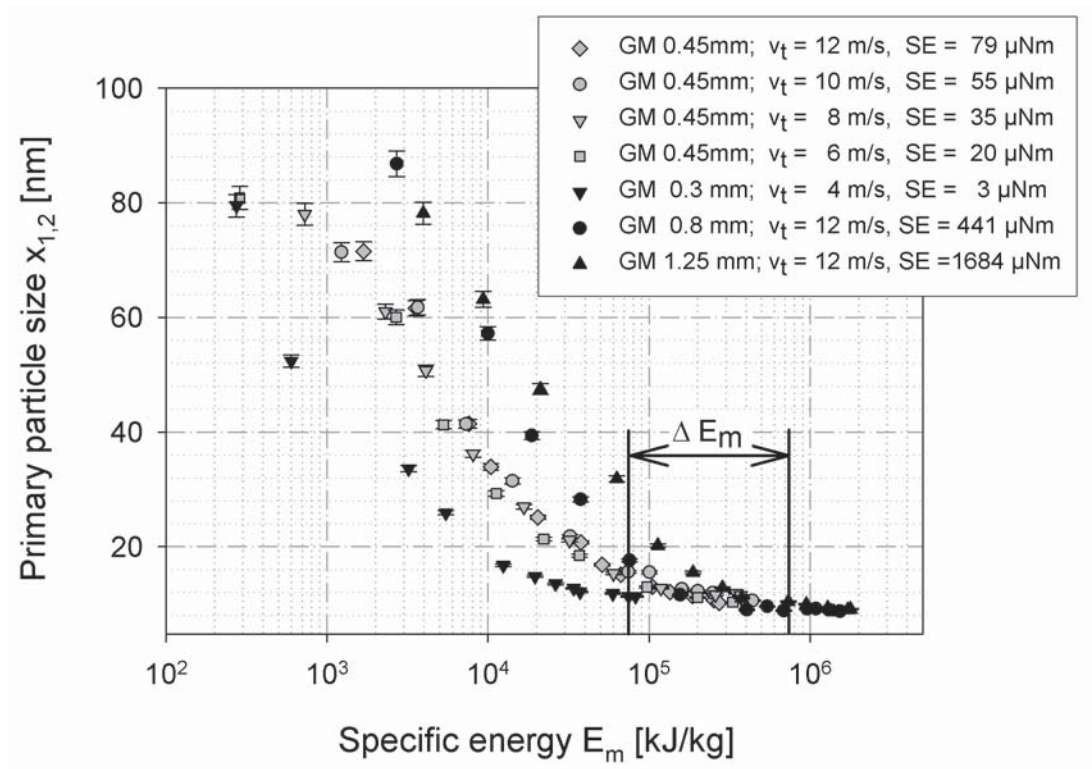
82

Figure 5.18.: Influence of stress energy on breakage behavior of SnO_2

In all experiments, the primary particle sizes decrease with increasing specific energy input until a plateau in particle size -the grinding limit- is reached. Although the stress energy was increased by a factor of 560, no change in the grinding limit could be detected. Changing the revolution speed of the stirrer (grey symbols) does not lead to significant changes in the stress energy and therewith in the evolution of particle size. Since the stress energy has a cubic dependency on the milling bead size, the latter influences the breakage kinetics more strongly. Smaller milling bead sizes (0.3 mm, SE = 3 μNm) lead to larger breakage rates. With increasing grinding media size, the grinding performance gets worse indicating that the optimal stress energy is in a range of about 3 μNm or smaller. The use of smaller grinding media allow a much higher number of grinding beads in the milling chamber at same filling ratio. As a consequence higher stress numbers can be realized, which makes the grinding process more efficient. In Fig. 5.19, the achieved particle sizes as a function of the stress energy for three different specific energy inputs are presented.
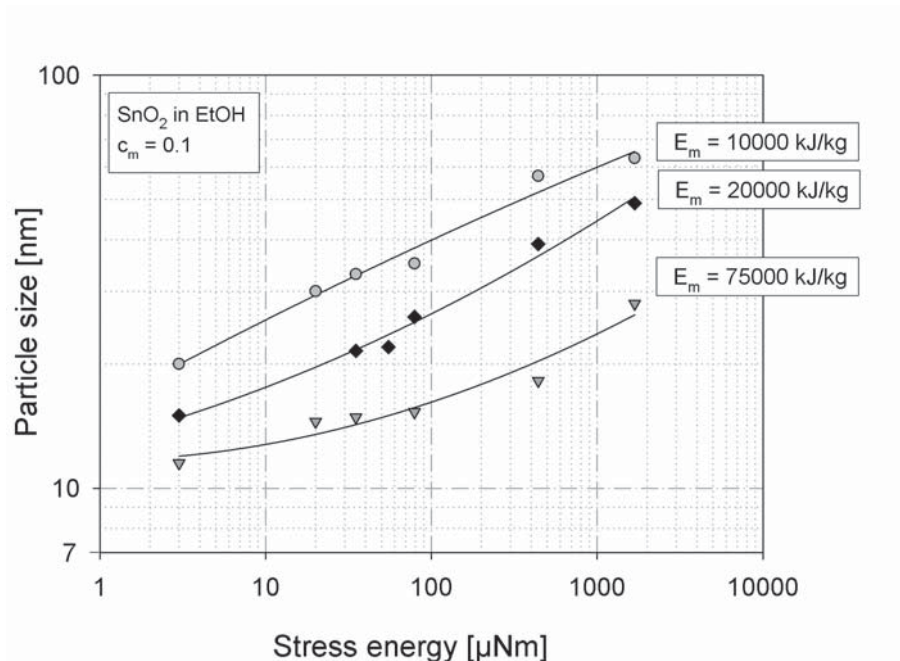
Figure 5.19.: Achieved particle sizes as a function of SE at different energy inputs

It is obvious that with smaller stress energies, the grinding process becomes more energy efficient and the same particle sizes can be reached with much less energy input. These findings were already shown by Kwade for micro-sized particles [Kwad 96] and by Mende for particles in the nanometer range [Mend 04b]. Accordingly, the grinding limit can also be reached with much less energy input. In Fig. 5.20, the consumed energies to reach the grinding limit are given as a function of SE.

Plotting the energy input to reach the grinding limit over the corresponding SE gives a straight line in the double logarithmic scale for the investigated regime. The dotted line represents the expected development for smaller SE values, which was confirmed for other material systems [Kwad 96]. However, with a stress energy of 3 μNm, the grinding limit can be achieved with less than 10 % of the total energy input which is required in the experiment with the largest stress energy (SE = 1684 μNm).
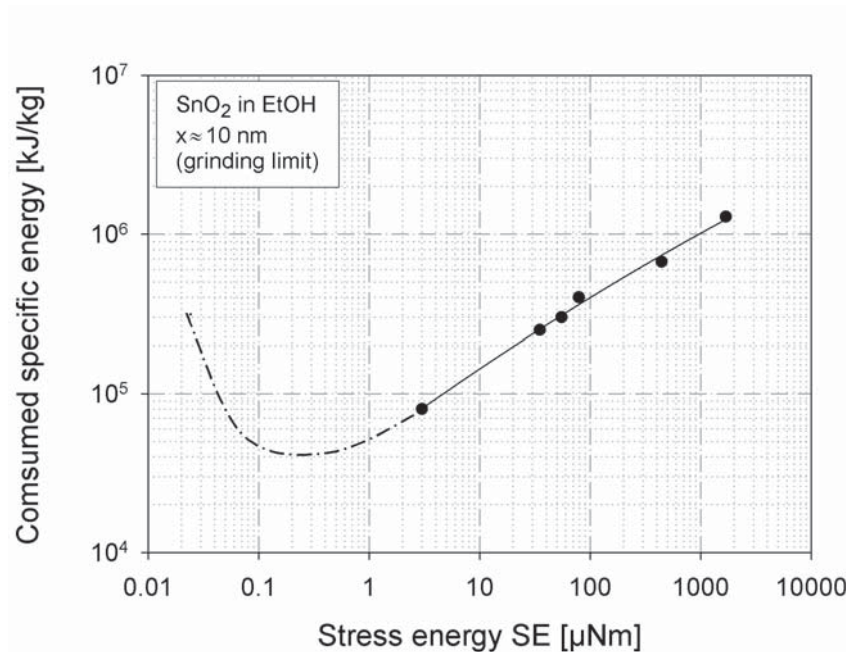
Figure 5.20.: Specific energy to reach the grinding limit as a function of SE

Influence of overstressing

In order to study the influence of an unnecessarily high energy input on the product quality, the suspensions ground with a stress energy of 3 μNm and 1684 μNm were analyzed regarding amorphous content and amount of grinding media wear. The amorphous content was determined via X-ray diffraction using an internal standard as reference. Inductively coupled plasma mass spectroscopy was used to measure the attrition content of the grinding media in the final ground powders. The analytical results are summarized in Tab. 5.2. The much longer grinding time in the case of the lower stress energy is a result of the lower revolution speed of the stirrer n, which strongly reduces the power input ($P \sim n^3 \cdot d^5 \cdot \rho_s \cdot Ne(Re)$).

The results reveal that an overstressing strongly reduces the quality of the product particles. Although the final crystallite sizes are almost identical (both sample have achieved the grinding limit) the amorphous content is nearly twice the content of the powder ground under milder conditions. Strong impacts between the grinding beads destroy the crystalline lattice and lead to an amorphization of the material. Moreover, the contamination of the milled powders by grinding media wear is also higher for higher stress

Table 5.2.: Product quality after milling with different SE

	SE = 3 μNm	**SE = 1684 μNm**
Specific energy	$8.2 \cdot 10^4$ kJ/kg	$1.8 \cdot 10^6$ kJ/kg
Milling time	97 h	44 h
Crystallite size	11.3 nm $\pm$ 0.1 nm	10.1 nm $\pm$ 0.2 nm
Amorphous content	27 ± 2 wt%	51 ± 2 wt%
Attrition content	3.8 wt%	5.1 wt%

energies. From this, it follows that not only energy savings of more than 90 % can be reached by an appropriate adjustment of process parameters, but also a better product quality can be gained.

5.4.2. Breakage mechanisms at different SE

As already discussed in the previous section, an appropriate choice of the stress energy will help to reduce the energy consumption and achieve a higher quality of the product suspensions. Now the question arises if the same breakage mechanism takes place, although the samples are stressed with an almost 600 times higher intensity. Therefore, samples of both experiments are compared by means of SEM analysis. Since the breakage behavior strongly depends on the particle size, samples with comparable specific surface areas were analyzed. Both samples exhibit particle sizes well above their grinding limit. In Fig. 5.21, the breakage patterns of the tin dioxide particles stressed at different SE are presented. Since no stabilizer was used in the experiments, the primary particles are highly agglomerated.

At low stress energies, more or less homogeneous isotropic fragment shapes can be observed in the sample indicating a dominating brittle failure mode. At high stress energies, the breakage pattern is totally different. Large platelike particles are present in the suspension. The SnO_2 particles were squeezed almost completely flat between the grinding beads. During impact, a stress field arises inside the particles, which depend on the stress energy of the grinding media. If the resulting stresses in the whole particle exceed the yield stress of the material, a complete breakage-free deformation of the particles can take place. This observed behavior was already predicted by
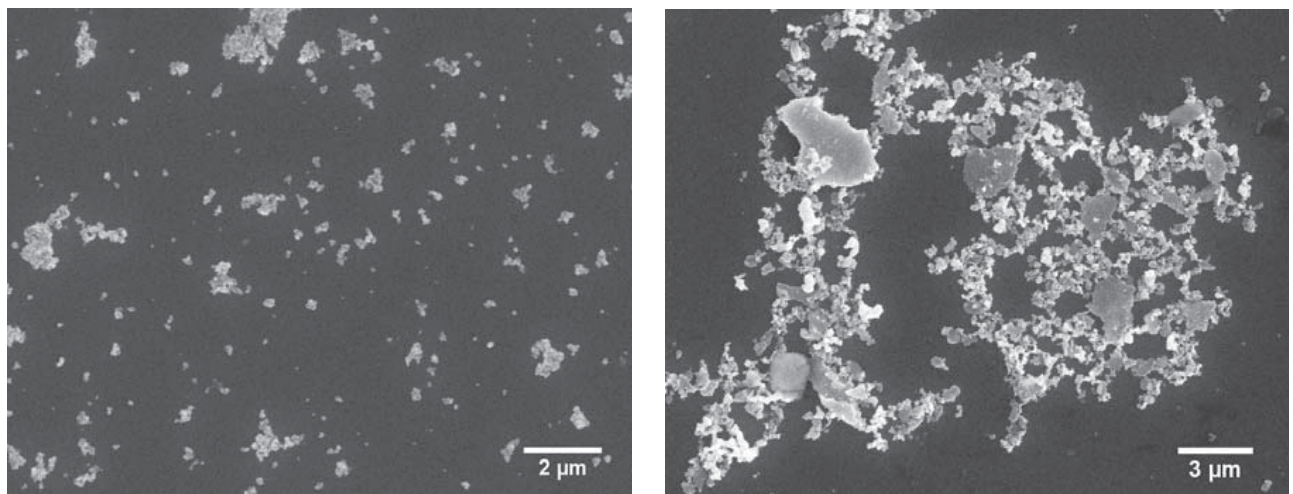
Figure 5.21.: SEM images of milled SnO_2 particles at different stress energies: SE = 3 μNm (left); SE = 1684 μNm (right)

Schönert, Kendall, and Hagan (see chapter 2.2) for sizes below the ductile-to-brittle transition and described as the limit of grinding. Their conclusion is right for single compression experiments, but cannot be confirmed under cyclic loading as shown in this study. It can be assumed that the initial tin dioxide particles yield sizes already below the ductile-to-brittle transition. If the smashed particles will be caught again by the grinding beads, they arrange in a way that the flat side is stressed once more. Thus, the particles will become increasingly thinner until a crack arises from the surface or edge and the particle breaks gradually. Due to the cyclic loading, a size reduction is possible even below the brittle-to-ductile transition size. Thereby, the size reduction can be theoretically realized in a dominating brittle or ductile manner as schematically shown in Fig. 5.22.

Below the ductile-to-brittle transition size x_{BDT}, a possible flaw inside the material is so small that the necessary breakage stress exceeds the yield stress of the material. Hence, under loading, the material starts to yield instead of fracturing. However, during cyclic loading, the necessary breakage stress can be much lower (depending on the number of cycles) than the ultimate tensile stress of the material. Therefore, it is theoretically possible to break a particle with stresses even below the yield stress as long as the loading is larger than the fatigue limit. As a consequence, brittle failure (or better said semi-brittle failure, since a plastic zone is in the most cases

87

Fatigue fracture

Cyclic loading

$x < x_{BDT} \rightarrow$

$\sigma_{yield} < \sigma_{breakage}$

$\sigma < \sigma_{yield}$

(Semi)-brittle failure
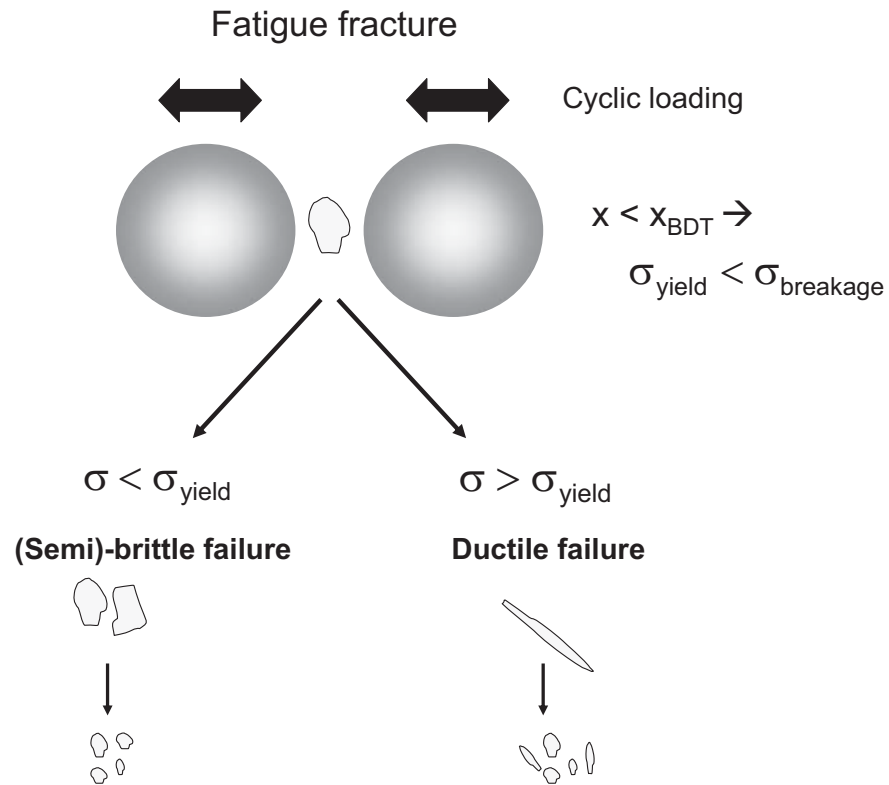
$\sigma > \sigma_{yield}$

Ductile failure

Figure 5.22.: Size reduction by fatigue fracture

formed around the crack tip) could take place at a sufficiently high number of cycles. Crack propagation proceeds from pre-existing flaws or surface edges by a subcritical crack growth mechanism. This means that under cyclic loading below the short-term strength slow crack propagation takes place until the crack reaches a critical length (Griffith criterion is fulfilled) and a catastrophic failure of the material occurs.

Subcritical crack growth is often observed in ceramic materials and makes their usage for cyclic loading applications due to the sudden failure event difficult. This failure mode is limited to pre-existing flaws inside the material or sharp edges on the surface, which can act as crack nucleus. If the stress inside the particle is locally higher than the yield stress of the material, plastic deformation occurs. Dislocations are formed and move through the particle resulting in a distorted lattice. During cyclic loading, an accumulation of defects reduces the ductility of the material (strain hardening), enhances the elastically stored energy in the lattice, and leads

to crack nucleation by the formation of new grain boundaries or microvoids, for instance.

The crack nucleation now allows further stepwise propagation of the crack until the whole particle is broken. Thereby, the fracture can yield both brittle and ductile characteristics depending on the applied stress. The ductile fracture is governed by a severe plastic deformation of the particles prior to fracture. At very high transferred stresses, the yield stress is exceeded in the whole particle leading to a complete plastic deformation as observed in the milling experiment with the highest stress energy. Nevertheless, independent of the degree of deformation, below a certain crystallite size, dislocations become unstable and inhibit further plastic deformation, and therewith crack nucleation, which limits further size reduction.

Conclusively, cyclic loading allows a size reduction of nanoparticles by a fatigue fracture. Thereby, the breakage mechanism strongly depends on the generated stress inside the particle relative to its yield stress and can take place in a more brittle or ductile manner. A pure brittle (or semi-brittle) failure below the brittle-to-ductile transition size is nonetheless very unlikely since the activation of dislocation is normally less energy consuming than crack propagation processes.

5.4.3. Influence of grinding media shape

In further grinding experiments, another grinding media material was used. Instead of the spherical yttria-stabilized zirconia (YSZ) beads, milling experiments were carried out with an irregular shaped alumina split in a size range of 0.18 - 0.3 mm. Changing the product particles or the grinding media material will affect the portion of energy transferred from the grinding media to the particles and a comparison of different grinding results becomes difficult. Hence, a product related stress energy SE_P and a product related specific energy input $E_{m,P}$ has to be introduced to allow a comparison between the grinding results. The product related specific energy input $E_{m,P}$ can be calculated using the following equation:

$$E_{m,P}(t) = \frac{\int_0^t (P(\tau) - P_0)\,d\tau}{m_P} \cdot \left(1 + \frac{Y_P}{Y_{GM}}\right)^{-1} \qquad (5.4)$$
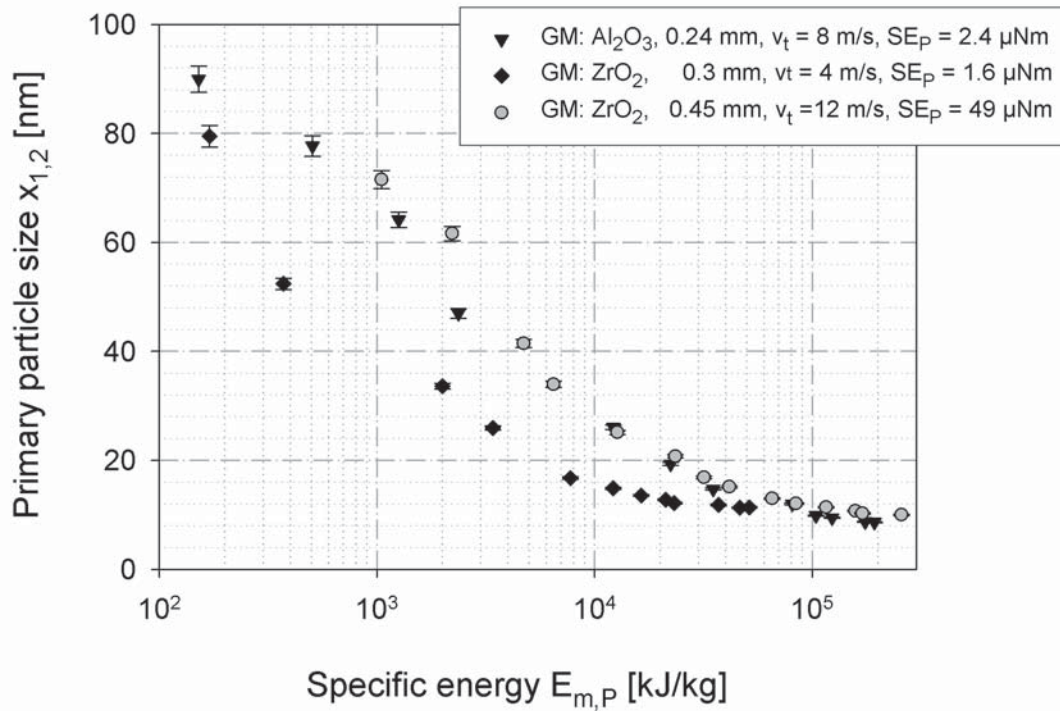

Figure 5.23.: Influence of grinding media shape on breakage behavior of SnO$_2$

The grinding results are illustrated in Fig. 5.23. According to the concept of stress energy and stress number, it is assumed that the same stress energy and same specific energy input yield the same particle size. This theory does not seem to hold for the alumina split as grinding media, where the same grinding performance as for the small zirconia beads was expected, because their product related stress energies are almost identical. In contrast, the particle sizes are shifted to higher energy inputs. Hence, the irregular shape of the alumina split is assumed to reduce the grinding efficiency as the active volume is smaller compared to the volume between spherical beads and lowers therewith the probability of capturing the product particles.

90

5.4.4. Influence of suspension viscosity

Higher suspension viscosities can lead to a dampening of the milling bead motion so that smaller stress intensities are transferred to the product particles. A huge amount of the kinetic energy of the grinding media is consumed for fluid displacement. Frances and Laguerie already examined the influence of the viscosity on the grinding behavior of micro sized alumina hydrate particles in a media mill. They observed a fall in the grinding performance with increasing viscosity of the slurry [Fran 98]. To investigate if those findings are valid for nanoparticle breakage as well and if the suspension viscosity also affects the grinding limit, tin dioxide was milled in ethanol ($\eta = 1.18$ mPas at 20 °C), ethylene glycol ($\eta = 21.3$ mPas at 20 °C), and water ($\eta = 1$ mPas at 20 °C) under standard conditions. The grinding results are presented in Fig. 5.24.
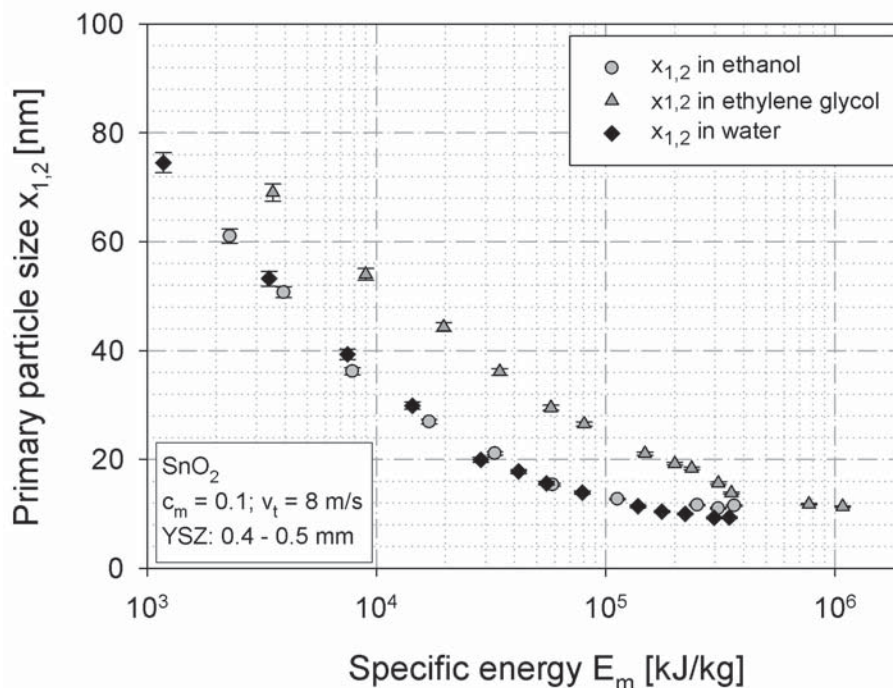

Figure 5.24.: Influence of suspension viscosity on breakage behavior of SnO_2

Obviously, the breakage rate of tin dioxide milled in ethylene glycol is strongly reduced, whereas no differences in the breakage behavior between the experiments in water and in ethanol are observed. But independent

from the dispersing media, the same grinding limit was achieved again for all investigated suspensions. To get an impression of the viscosity differences, rheology measurements have been carried out of the final milling suspensions and are presented in Fig. 5.25.
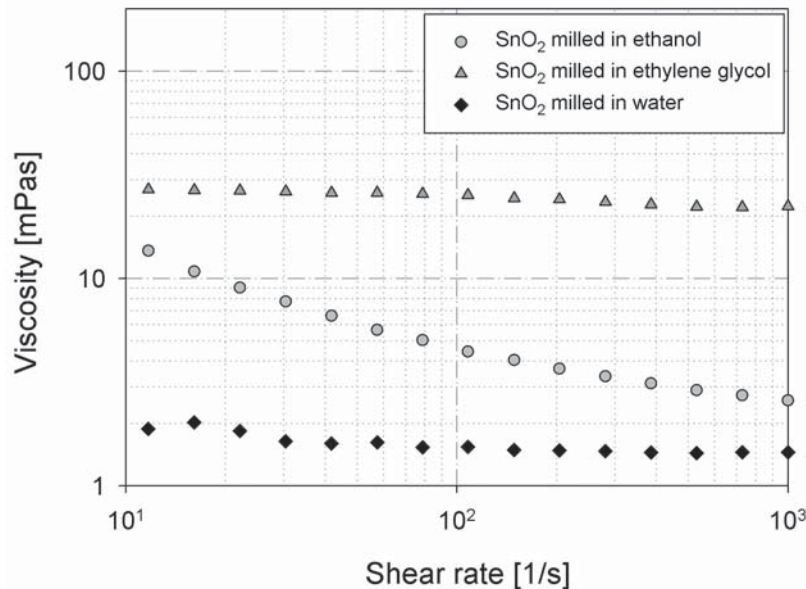

Figure 5.25.: Suspension viscosities of SnO_2 milled in different media

The suspensions based on ethylene glycol and water show almost New-tonian behavior, whereas the ethanolic suspension behaves shear thinning. The shear thinning behavior can be explained by the strong instability of the ethanol based suspension. Clusters formed by the particles are destroyed with increasing shear rate, which results in lower suspension viscosities. At high shear rates, which predominate in the milling chamber, the viscosity of the ethylene glycol suspension is about one order of magnitude larger than the viscosity of the aqueous and ethanolic suspension. A stronger damp-ening of the grinding media takes place and results in a worse grinding performance. Since the grinding limit itself is very insensitive concerning variations in the transferred stress energies as shown above, the different suspension viscosities do not influence the grinding limit at all. The vis-cosity differences between the aqueous and the ethanolic suspension at low shear rates can be explained by the suspension stability. Without the addi-

92

tion of any stabilizer the ethanolic suspension is very unstable, whereas the pH value of the aqueous tin oxide suspension increases during the grinding treatment into a stable regime, where high negative zeta-potentials ($\zeta = -50$ mV) were reached. The instability leads to higher viscosities of the ethanol based suspension in the low shear rate range, which is mainly determined by interparticle interactions rather than hydrodynamic forces. Similar results in aqueous systems for alumina particles dispersed in water were observed by Stenger et al. [Sten 03].

Although the grinding limit itself is not affected by the suspension viscosity, the possibility to reach this limit is not necessarily given: It was shown in the work of Stenger that a strong increase in viscosity and yield stress due to a higher solid content or more pronounced particle-particle interactions can lead to an early stop of the experiment since the suspension cannot be pumped anymore. Thus, both a sufficiently low viscosity and a moderate related yield stress are necessary preconditions to reach the true grinding limit at all. The correlation between suspension viscosity and grinding progress is currently investigated in more detail at the Institute for Particle Technology at the University in Braunschweig. A critical viscosity is estimated at which the whole kinetic energy of the grinding beads is consumed for fluid displacement instead of particle stressing. The most important results are summarized in a joint publication [Knie 10b].

It is often discussed in literature, whether the environmental conditions such as the surrounding medium may influence the breakage behavior of the powder particles as claimed by Rehbinder et al. The authors argue that the adsorption of special molecules reduce the surface energy γ_s and facilitate therewith crack propagation according to the Griffith equation. However, the crack resistances R is several orders of magnitude higher than the surface energies for most of the materials, because of micromechanical processes (e.g. plastic zone formation), which consume additional energy. Hence, reducing the surface energy cannot have any effect on the breakage behavior if R $>> \gamma_s$. Nevertheless, for materials held together only by weak van der Waals forces where R $\approx \gamma_s$, a reduction of surface energy may improve the fracture or rather the dispersion process.

93

5.4.5. Influence of suspension stability

The influence of suspension stability was analyzed as next parameter. A different grinding performance is theoretically possible, because i.) the transferred energy is divided to several individual particles forming the agglomerate, which leads to a faster breakage kinetics if the stress energy per particle is still sufficient to cause fracture at all. ii.) It is also possible that the presence of agglomerates will facilitate a capturing of the particle cluster between the grinding media, due to a higher inertia compared to single particles. iii.) The suspension stability affects the viscosity, which in turn was shown to have an influence on the grinding performance by dampening effects.

In Fig. 5.26, the influence of suspension stability on particle breakage is demonstrated. The evolution of the primary particle size is given for a grinding experiment under totally stable conditions in water at pH 11 (adjusted by the addition of NaOH), under adequate stable conditions in water without the addition of any stabilizer, and under complete unstable conditions in ethanol.
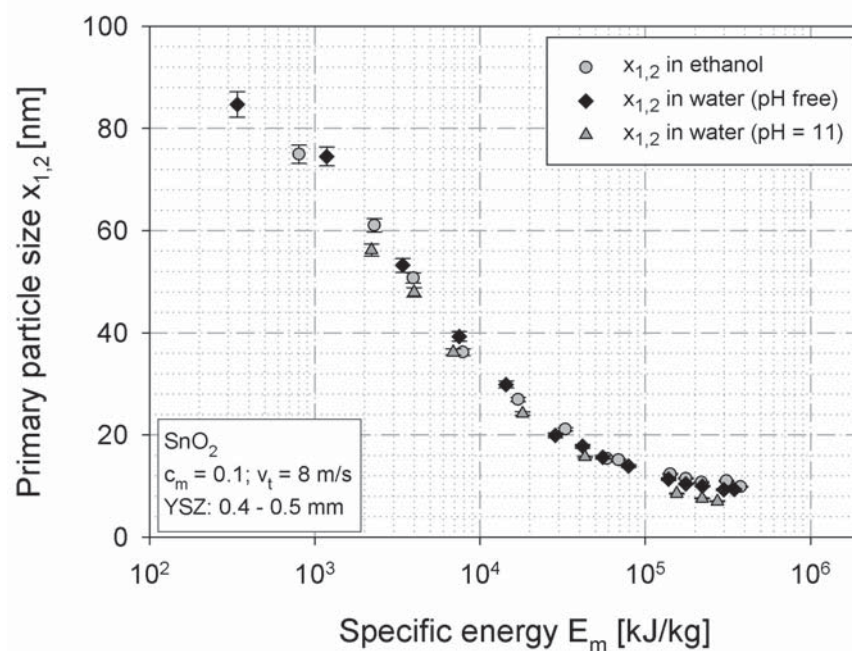
Figure 5.26.: Breakage behavior of SnO_2 milled at different stability conditions

94

By DLS measurements, the degree of agglomeration can be estimated. The milling experiment in water at pH 11 ends up at a $x_{50,3}$ value of 48 nm, the experiment in pure de-ionized water at 82 nm, and the ethanol milling at about 350 nm, depending on pre-dispersing conditions. Comparing the milling results, it becomes clear that the formation of agglomerates in the ethanolic suspension does not influence the breakage behavior. The primary particle sizes show nearly the same evolution in all three media and finally end up at almost the same plateau of about 10 nm. The measured $x_{1,2}$ values of the experiment in water at pH 11 yield slightly smaller sizes, which might be caused by the presence of the stabilizer that was still on the surface during the BET measurements. X-ray diffraction analysis confirms that the final crystallite sizes of all experiments are identical. Additional rheology measurements reveal, that at high shear rates, the viscosities of the suspensions are in the same order of magnitude, so that the same stressing conditions in the grinding treatment apply. It is assumed that the agglomerates in the ethanolic suspension are only weakly attached to each other and deagglomerate in the shear field in the milling chamber. Nevertheless, these results should not be generalized because on the one hand stronger agglomerates may behave differently and on the other hand the investigated suspensions have only low solid contents (c_m = 10 wt %). At higher solid concentrations larger differences in the viscosities may exist even in the high shear rate regime and the yield stress may exceed a processable limit, especially for unstable suspensions.

5.4.6. Influence of process temperature

Finally, the influence of the process temperature has been investigated. Therefore, the tin dioxide powder was ground in ethanol at -5 °C and 45 °C, so that a total temperature variation of 50 °C could be realized with the experimental setup. To reach a temperature of -5 °C inside the milling chamber, the tip speed of the stirrer was slightly decreased to 6 m/s. Such small decrease of stirrer tip speed does not influence the grinding behavior as shown in Fig. 5.18. The evolutions of the primary particle sizes are presented in Fig. 5.27 [Knie 11a].
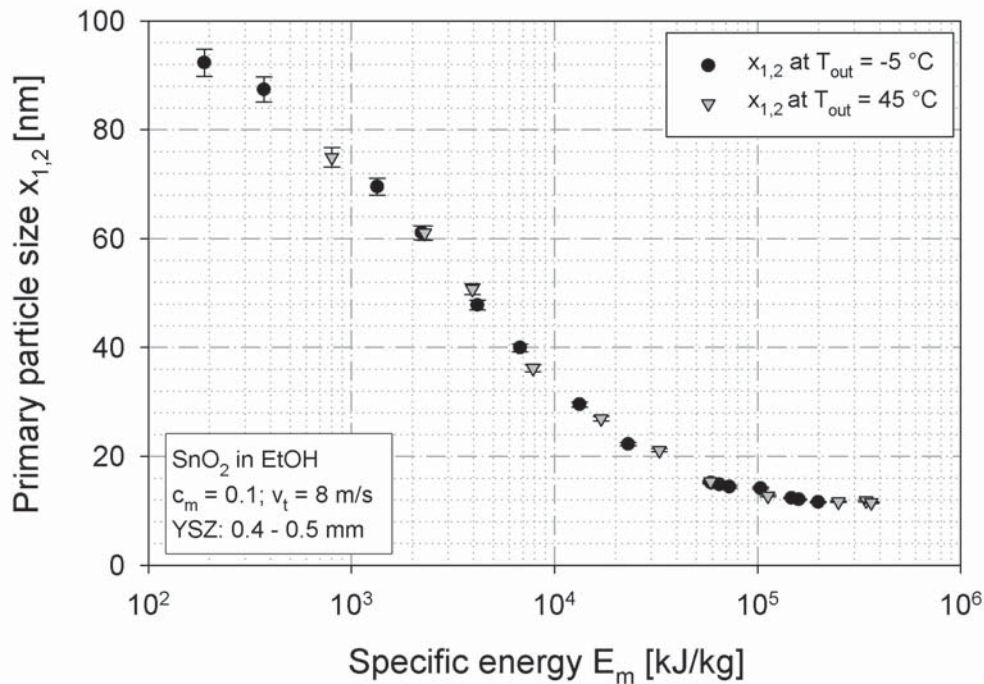
Figure 5.27.: Influence of suspension temperature on breakage behavior of SnO_2

Reducing the temperature from 45 °C to -5 °C does not influence the grinding behavior of the tin dioxide particles. Both the breakage kinetics and the grinding limit are not affected by the temperature variation in the analyzed range. Since oxide particles are innately very brittle materials, a decrease in temperature of only 50 °C will hardly change their material properties.

Beside breakage and stability, the temperature can also influence the suspension viscosity, which itself can affect the breakage by dampening of the grinding media as already shown above. Hence, rheology measurements of the final milling suspensions were carried out at the particular temperatures and are presented in Fig. 5.28. Since it was not possible to measure viscosities at temperatures below 0 °C with the available rheometer, the viscosity was determined at 0 °C. No significant changes in viscosity are observed in the high shear rate regime (consider the logarithmic scale). At a shear rate of 1000 s^{-1}, the suspension viscosity at 45 °C is about 5.6 mPas, whereas the viscosity yields a value of about 2.8 mPas at 0 °C. Hence, comparable stressing conditions can be assumed in the milling chamber, which explain
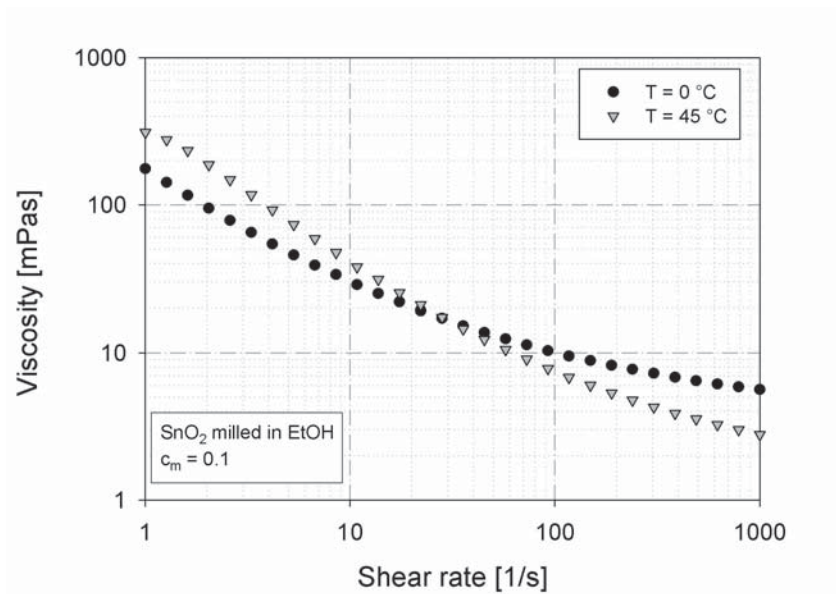
96

Figure 5.28.: Suspension viscosities of milled SnO_2 at different temperatures

the similar breakage behavior. For low shear rates, much higher viscosities are achieved at higher temperatures indicating stronger interparticle interactions.

5.4.7. Conclusion of process variations

Changing the process conditions namely the grinding media size and shape, the revolution speed of the stirrer, the suspension viscosity and stability as well the process temperature leads to the conclusion that the grinding limit is hardly affected by the process itself in the analyzed range. Not even an increase in impact intensity by a factor of almost 600 could shift the grinding limit to smaller values. From these observations, it follows that the grinding limit must either be primary material dependent or a consequence of machine limitation. Both aspects will be discussed in the following sections. In contrast to the grinding limit, a strong influence of process parameters on the breakage rates is observed. A less energy consuming size reduction can be achieved, if the stress energy is set to its optimal value. The grinding limit can be achieved with only a fraction of energy which is required with larger SE values. Moreover, high suspension viscosities cause a dampening of the grinding media and also reduce the

grinding efficiency. Not only huge amounts of energy can be saved by proper choice of process parameters, but also a higher product quality in terms of crystallinity and attrition content can be gained, if an overstressing of the product particles is avoided.

5.5. Breakage behavior of various inorganic materials

5.5.1. Milling behavior of zirconia and alumina

After the breakage mechanisms for tin dioxide and its influencing factors have been intensively investigated, the question arises if the observed findings are also valid for other ceramic materials. Therefore, grinding experiments of different inorganic materials were carried out. A closer look was given on the brittle oxide ceramics alumina and zirconia. Both materials were milled under the same standard conditions as the SnO_2 particles (LabStar LS 1, solvent: ethanol, v_t = 8 m/s, YSZ: 0.4 - 0.5 mm). First, the grinding results of zirconia are presented in Fig. 5.29. The solid content in the experiments was set to 20 wt%.

A very similar evolution of the external and internal structure during the grinding treatment is obtained. Both primary particle size as well as crystallite size decrease with specific energy input. At the end of the grinding experiment, both curves still yield a certain slope, which becomes visible in the double logarithmic scale (Fig. 5.35). A final primary particle size of about 4 nm was reached. Since a size reduction of only 0.3 nm is observed in the last 6 hours of grinding, it can be assumed that the grinding limit is reached and the fall towards smaller sizes is only caused by the changing width of the size distribution.

The initial particles already yield a certain strain level, which might be related to a pretreatment of the powder. However, the strain increases to a maximal value and finally decreases to nearly zero. It has to be emphasized that nanoparticles always contain a certain microstrain which increases with decreasing particle size due to the bending of the surface that causes slight distortions of the lattice. However, this strain level is much smaller than the strain resulting from lattice defects. Again, the grinding limit is reached almost simultaneously to the drop of strain. Very early in the experiment
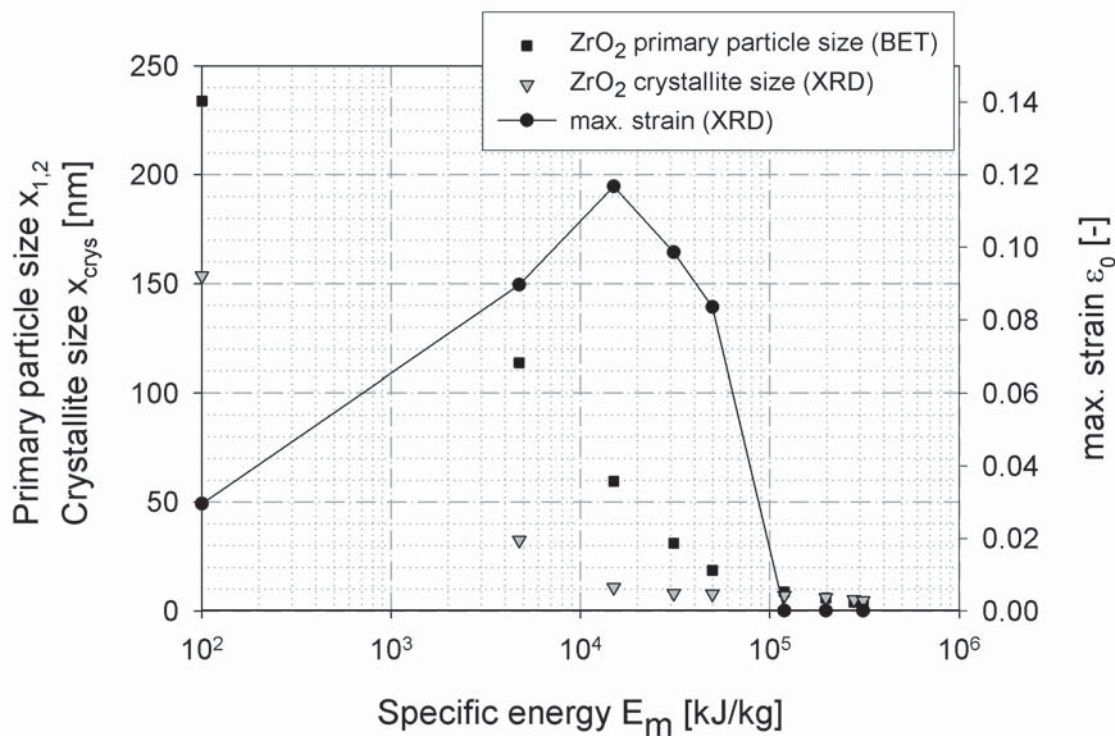
98

Figure 5.29.: Breakage behavior of zirconia milled in ethanol

the final crystallite size is reached, whereas the fracturing of the particles follows more slowly.

Interesting is the evolution of the amount of crystallites per primary particle N as presented in Fig. 5.30. A totally different development as compared to the SnO_2 particles is observed. A steep increase in the amount of crystallites takes place at the beginning of the grinding treatment. This can be explained by a dominating grain refinement (probably by a subgrain formation) at the beginning of stressing. The final amount of crystallites per particle can yield values below one, which can be explained by the different average weighted sizes. Whereas the median Sauter diameter is a surface weighted diameter, the crystallite sizes are volume-averaged values, which lead to larger sizes in polydisperse systems. Due to the double logarithmic scale, small deviations in size will appear more significantly in the diagram. In addition, the influence of grinding media wear is still unclear. During grinding of hard materials such as alumina or zirconia, high attrition amounts are found in the ground powders. Hence, the measured BET sur-

face area can be affected. Since the morphology of the media wear is still unknown and probably depend on the milling material and conditions, it is difficult to estimate in which direction the primary particle sizes are falsified.
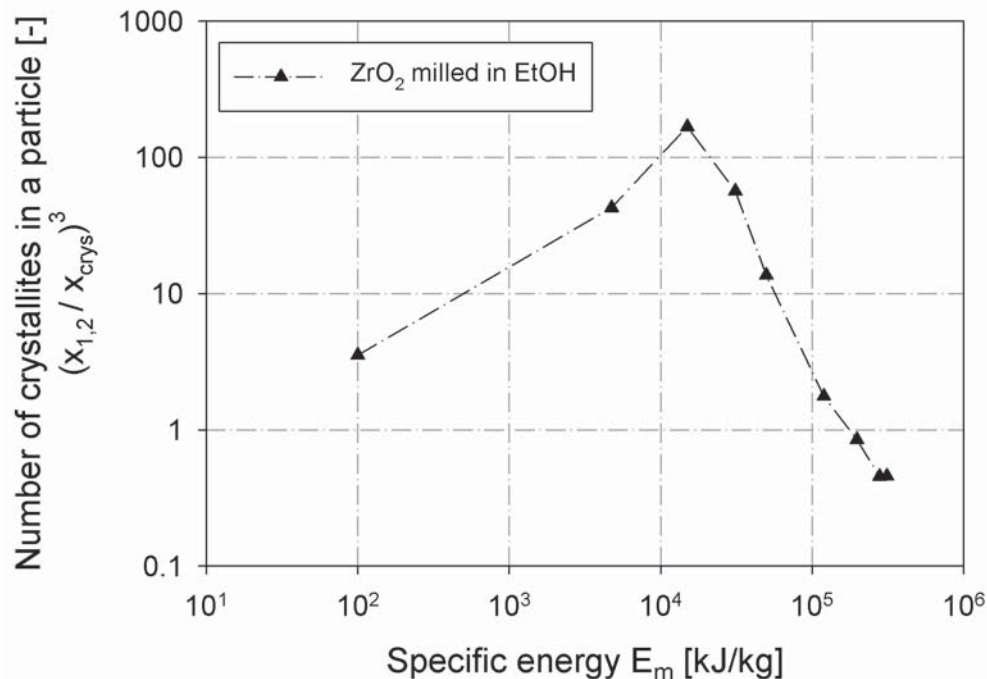

Figure 5.30.: Evolution of the number of crystallites per ZrO_2 particle during a grinding experiment

As the next material system, the breakage behavior of alumina particles dispersed in ethanol is investigated (see Fig. 5.31). A grinding limit for the alumina particles is also observed for long comminution times. The limit is reached at a final particle size between 11 and 14 nm. At that time, the particles still contain a certain strain level. The determination of the strain inside the particles is carried out with the software TOPAS 3.0. Only very little information is given about the physical background and exact determination of the microstrain. In addition, the use of the 1-dimensional VANTEC-1 detector leads to a poor resolution of the pattern and only moderate GOF ("goodness of fit") values are obtained. Although the qualitative evolution of the strain during a grinding experiment could be confirmed by measurement with a point detector at the Institute of

100

Mineralogy (University Erlangen-Nürnberg), their absolute values should be treated with care. More reliable rms (root means square) strain data should be obtainable by an evaluation of the X-ray patterns by means of a Williamson Hall plot, for instance.
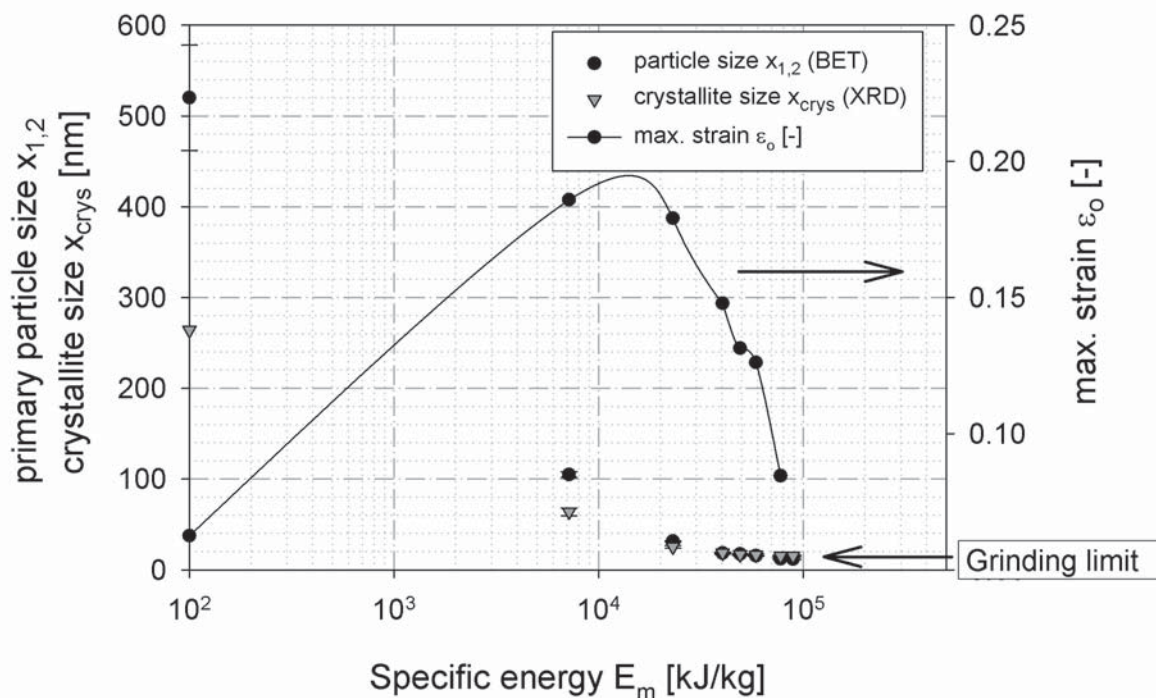

Figure 5.31.: Breakage behavior of alumina milled in ethanol

Regarding the evolution of the number of crystallites per particle in Fig. 5.32, a very similar breakage behavior to the tin dioxide particles is observed. Although the evolution of the external structure of the three investigated systems is almost identical, their internal structure differs as revealed with the amount of crystallites per particle.
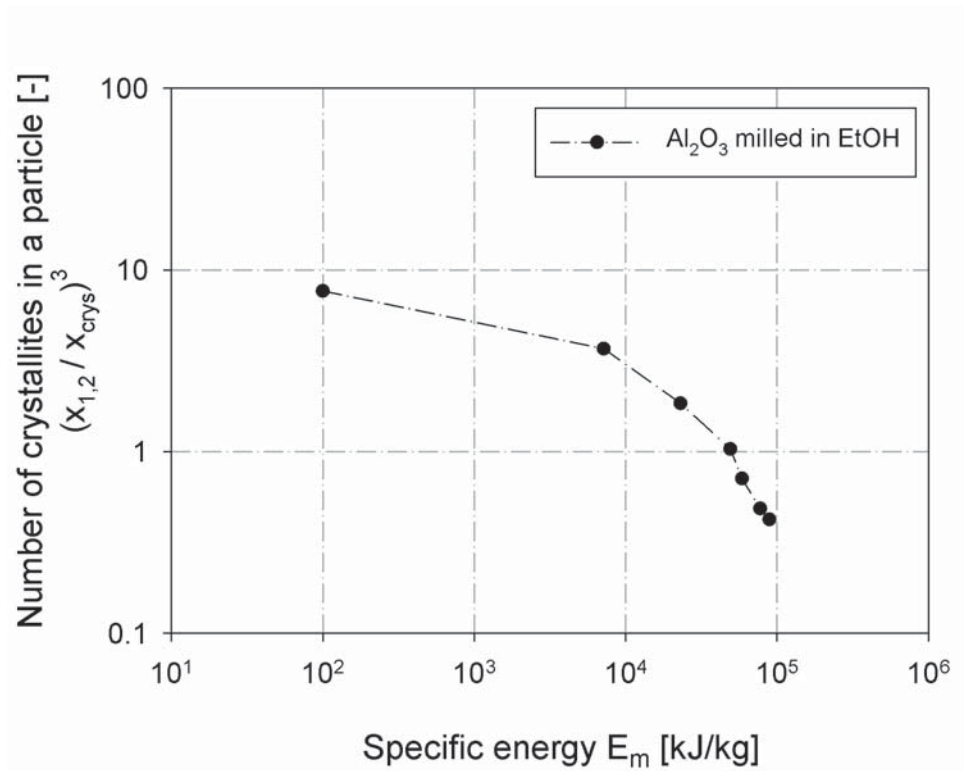
Figure 5.32.: Evolution of the number of crystallites per Al_2O_3 particle during a grinding experiment

In Fig. 5.33, the two different observed cases are illustrated schematically. Whereas zirconia shows a strong grain refinement at the beginning of the grinding treatment, the two other materials react on the stressing mainly with particle breakage. The slope of crystallite size reduction kinetics is very flat compared to the particle size reduction until all grain boundaries were broken and fracture continues as monocrystal-breakage. This behavior explains the evolution of the number of crystallites per particle N for tin dioxide and alumina particles. As grain refinement is the dominating process in zirconia, the final crystallite size is already reached in the poly-crystalline state. ZrO_2 is known to behave more ductile than other ceramic materials, which explains the strong grain refinement by plastic deformation processes. The primary particles achieve the grinding limit much later in the comminution process. Since the inserted energy is preferably used for grain size reduction, a drastic increase in the number of crystallites per particle is observed. Further explanations for the different breakage behav-

102

ior might be beside the lower activation energy for dislocations in zirconia, a higher grain boundary energy in tin dioxide and alumina which facilitates an intercrystalline fracture.
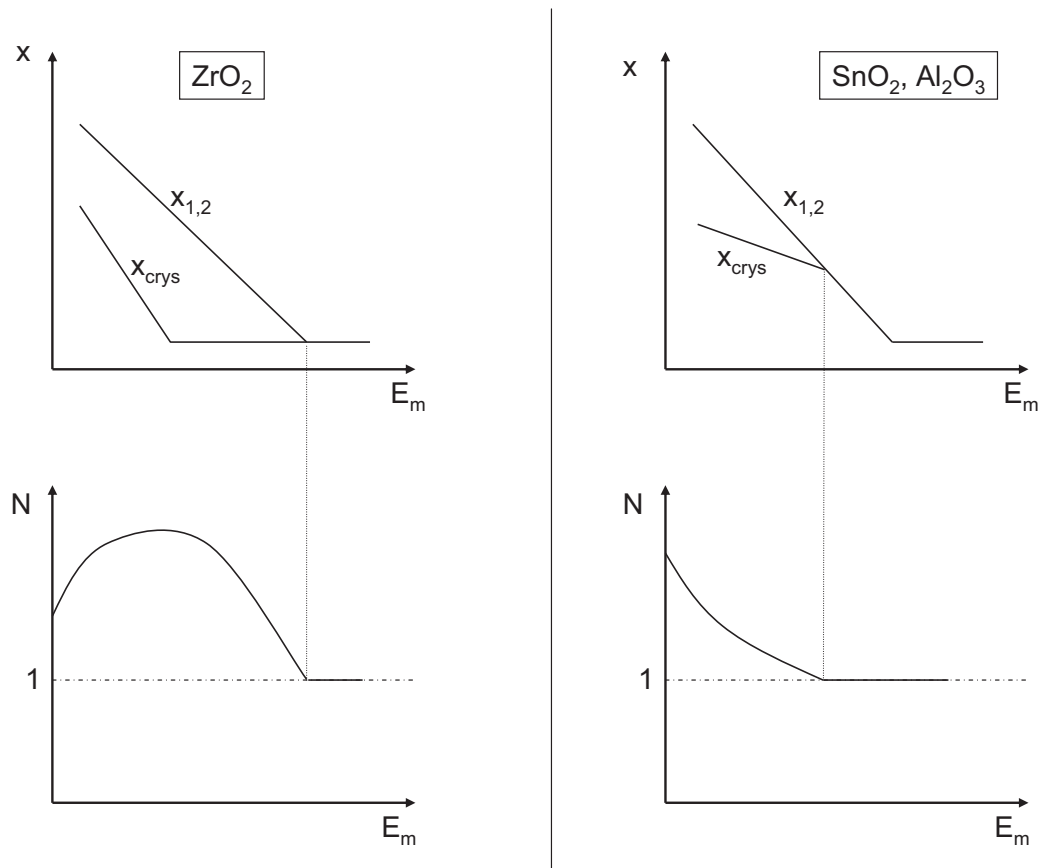

Figure 5.33.: Breakage behavior of different ceramic materials (schematically)

During milling of SnO_2, the stress energy has a strong influence on the breakage kinetics but the grinding limit remains unaffected. To demonstrate that these findings are not only valid for tin dioxide, alumina particles were also milled at different stress energies in ethanol. Since milling of the hard alumina particles causes huge amounts of grinding media attrition that affect the BET results, the comparison is carried out by illustrating the crystallite size evolutions as shown in Fig. 5.34. In the X-ray diffraction patterns, zirconia peaks also arise, which indicate that at least a part of the attrition is crystalline with a median crystallite size of less than 10 nm.

103

However, a separate evaluation of the alumina phase is possible by means of XRD. ICP-MS measurements reveal that zirconia contents up to 20 wt% were found in the milled powders (depending on SE, specific energy input and solid content).
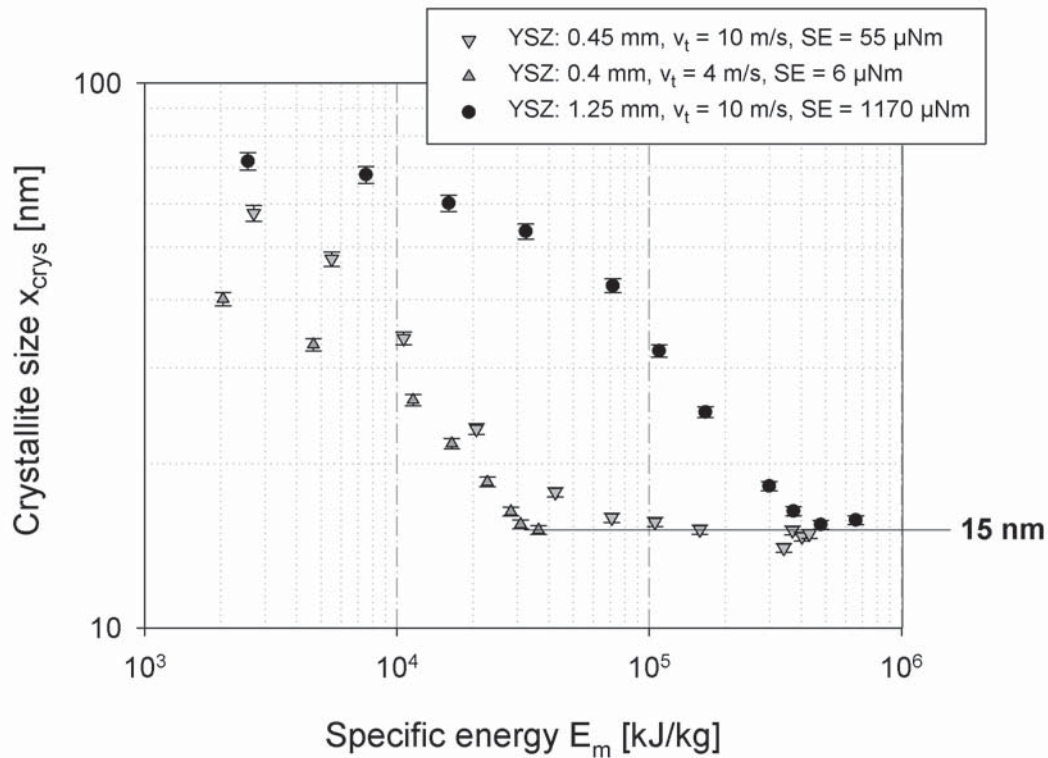

Figure 5.34.: Influence of stress energy on the breakage behavior of alumina

Again, a strong influence of stress energy on the breakage behavior is observed. With lower SE values, a more economic grinding treatment can be realized. But similar to the SnO_2 investigations, the grinding limit reaches almost the same value ($x_{crys} \sim 15$ nm) in all three experiments even though the stress energy was varied by a factor of about 200. It is often observed in the Al_2O_3 experiments that the limiting sizes obtained from BET measurements differ from the crystallite sizes. It seems that the differences become more significant at higher stress energies. Maybe a much higher attrition content or changes in the particle morphology falsify the BET results and are responsible for the observed deviations.

104

Besides the breakage behavior of ceramic materials, some applications for the produced nanoparticle suspensions have been investigated. Highly filled alumina suspensions with particle sizes down to 20 nm were used to produce thin films in a tape casting process with subsequent sintering. The usage of nanoparticles enables an inprovement of product quality regarding mechanical strength, optical transparancy, sintering temperature, and surface roughness of the final tapes [Vozd 10]. In another application, the produced ceramic nanoparticles were homogeneously introduced during accumulative roll bonding (ARB) into aluminum sheets by airgun spraying. A considerable strengthening effect is observed due to nanoparticle reinforcement [Schm 11].

5.5.2. Comparison of different materials

Besides SnO_2, ZrO_2, and Al_2O_3 other inorganic material systems were investigated. All particles were milled in ethanol at comparable SE_P values. The grinding results are presented in Fig. 5.35.

As expected, different materials exhibit different breakage kinetics as well as a different grinding limit. The breakage rates strongly depend on the stressing conditions and each material system yields its own optimal SE, which is in addition a function of particle size. Hence, a comparison of the breakage kinetics of the different materials is not possible. But under the assumption that the grinding limit is not affected by the stressing conditions as shown for tin dioxide and alumina particles, a comparison of the materials can be carried out. So far, it seems reasonable to assume that the grinding limit is reached if defects cannot be generated or stored in the smallest crystallites and the lattice strain falls below a certain threshold. Hence, no accumulation of imperfections can result in crack nucleation and an increase in elastically stored energy. The few generated dislocations at surface sites under loading leave the crystal after the grinding media impact, so that the inserted energy is lost. No further fracture of the particles is possible at this stage unless the theoretical strength of the material can be overcome by the milling machine, which is very unlikely.
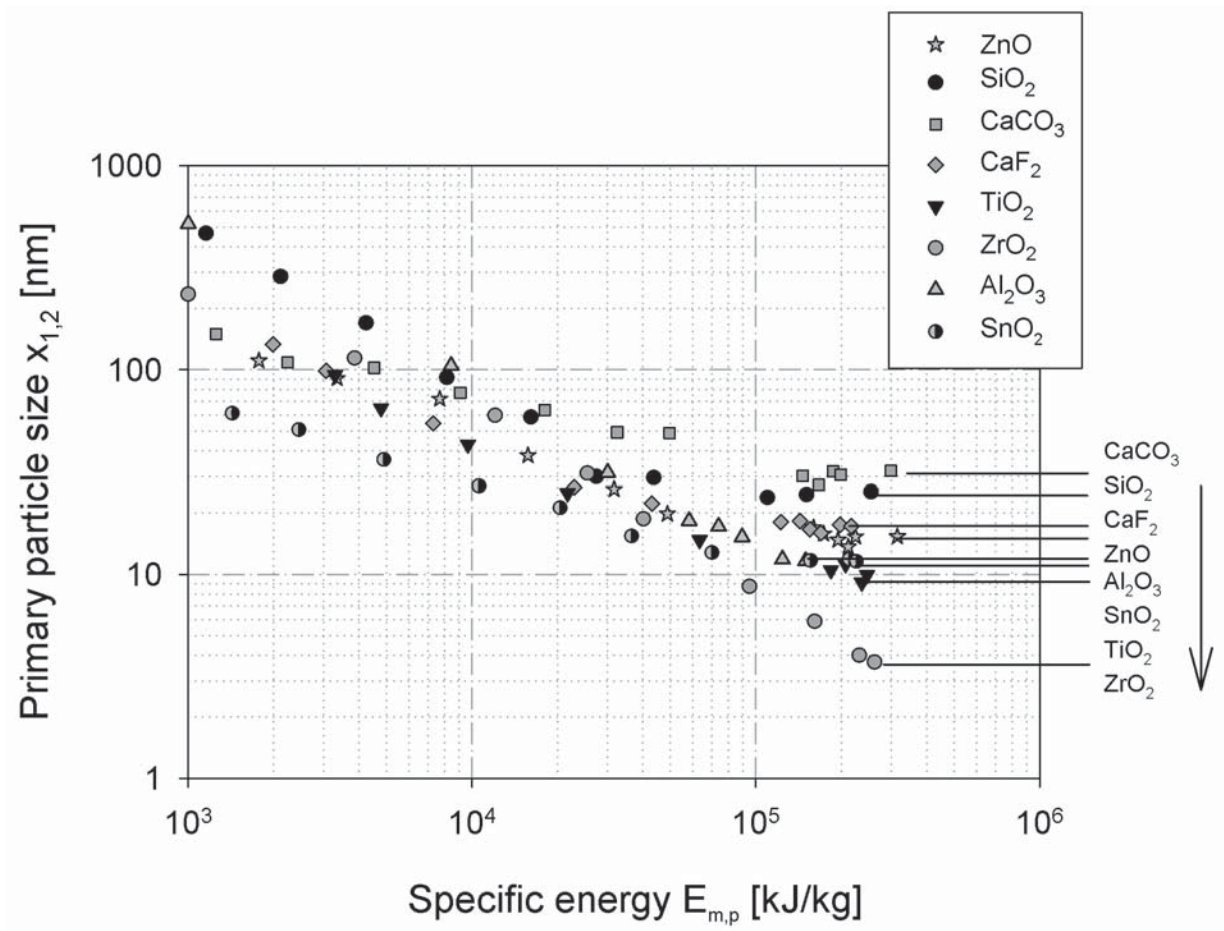
Figure 5.35.: Breakage behavior of various inorganic materials milled in ethanol

As already mentioned, dislocations leave the crystals if they come either too close to the surface or to another dislocation line. Both effects can take place in the smallest grains. The limiting size scales inversely with the acting Peierls stress of the material. Since material data like the Peierls stress are hardly known for most of the ceramic materials, a correlation with the grinding limit is difficult. However, the Peierls stress is a measure for the resistance against dislocation movement through the lattice and depends on the bond forces which has to be overcome during the movement. Therefore, the Peierls stress should somehow depend on the melting temperature of the materials, which in turn reflect the bond forces in the crystal. In Fig. 5.36, the grinding limits are plotted versus their melting temperatures.
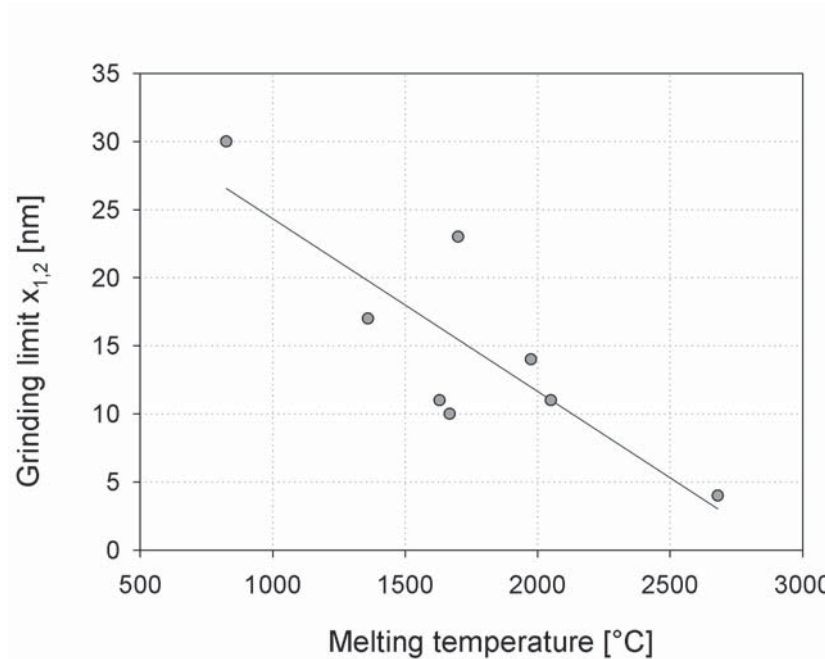
106

Figure 5.36.: Correlation of grinding limits with the melting temperatures of the materials

A vague trend of the grinding limit with melting temperature can be assumed from the experimental data. However, real processes are much more complex and the dislocation movement is in addition a strong function of the crystal structure with its number of related slip systems. Moreover, the limiting size for dislocation instability also depends on other parameters such as the shear modulus, the Burgers vector, and the Poisson's ratio (see Eq. 3.8). An exact calculation of the critical sizes is not possible, since much material data are not known for ceramic particles. Besides, some material data scale with grain size in the lower nanometer range for the larger ratio of surface-to-volume-atoms. Nevertheless, a rough estimation of the minimum separation distance between two edge dislocations is given for alumina and zirconia based on the equation of Nieh et al. (Eq. 5.5, [Nieh 91]). The material data used are given in Tab. 5.3 with their literature sources.

$$L = \frac{3Gb}{\pi(1 - \nu)H} \tag{5.5}$$

The calculated separation distances reveal smaller sizes than achieved in the milling experiments. But one has to keep in mind that some of the material data used are subjected to fluctuations depending on the literature

Table 5.3.: Estimation of minimal separation distance between two dislocations

	ALUMINA	ZIRCONIA
Shear modulus G	163 GPa [Wang 04]	100 GPa [Wu 02]
Burgers vector b	0.476 nm [Pezz 98]	0.3 nm [Fu 84]
Poisson's ration ν	0.26	0.3
Hardness H	11.2 GPa [Ting 08]	10 GPa [Shar 07]
Separation distance L	9 nm	4 nm
Achieved grinding limits (grain sizes)	15 nm	5 nm

source. Beside the grain size, the orientation within the crystal or a pre-treatment are also known to have an influence on the used values. Hence, reliable calculations of the minimal separation distance are almost impossible. In addition, it is not clear for the time being, if the crystallites need to be free of dislocations to obtain the grinding limit or just need to undergo a certain defect density.

5.5.3. Grinding limit as a result of machine limitation

It is often discussed if the grinding limit is the result of machine limitation. This can either be the case if the product particles are so small that they will be displaced with the liquid medium instead of being captured between the grinding media or if the particles are smaller than the roughness of the beads and vanish in the irregularities of the surface. The roughness of the YSZ grinding media was measured at the Institute for Particle Technology in Braunschweig. 0.3 - 0.4 mm YSZ grinding beads yield mean roughness values of about 20 nm. Since the collision between two grinding beads in the media mill is mainly an oblique impact accompanied by a rubbing of the faster bead over the surface of the slower one, it is very unlikely that the surface protuberances of one bead do not enter the holes of the other bead surface similar to a tooth system. Besides, if the roughness of the grinding beads would be the limiting factor, the same grinding limits should have been reached independently of the milled material. Furthermore, the usage of the alumina split as grinding media lead to the same final grinding limit as achieved with the YSZ beads although they exhibit different surface

108

roughnesses. Therefore, a limitation by the grinding media roughness can be excluded. The trapping of the product particles between the grinding beads was already investigated by G. Mende. First approximations show that the particles are strongly accelerated during the approach of the grinding media, but a part of them remain in the active volume captured in the stagnation point [Mend 04a]. Also, in the here presented results, no evidence that the displacement determines the grinding limit is found. Increasing the grinding bead diameter would lead to a stronger displacement flow so that larger grinding limits should have been obtained. The experimental findings reveal that the same final sizes are always achieved independent of the bead diameter. Hence, a lack of capturing the product particles can also be excluded as the reason for the grinding limit. Since even a strong variation of impact intensity does not affect the final particle sizes, it seems to be likely that the grinding limit is mainly material dependent.

5.5.4. Phase transition during grinding

During the grinding treatment, some materials undergo a phase transition. In particular, the milling of calcite and anatase in ethanol bear new crystallographic phases after the grinding treatment. In Fig. 5.37, the diffraction patterns of calcite milled in ethanol at different milling states are presented. New peaks appear whereas the calcites peaks vanish with time. The new peaks can be related to the aragonite phase, which is known to be the high-pressure phase of $CaCO_3$. The effect of phase transition from calcite to aragonite is often observed during dry grinding in high energy planetary ball mills, whereas the transition was never described in wet media milling [Mart 81], [Pese 08], [Garc 02].
Evaluation of the patterns by a Rietveld refinement gives the crystallite sizes of calcite and aragonite as well as their phase content as a function of the specific energy input. The results are given in Fig. 5.38. At the beginning of the grinding treatment, the primary particle sizes as well as the calcite crystallite sizes decrease. After an energy input of about 8000 kJ/kg, an aragonite phase can be detected. Their crystallite sizes seem to increase in size until they achieve almost the crystallite sizes of the calcite phase, before their grain refinement due to the grinding treatment occurs. At the
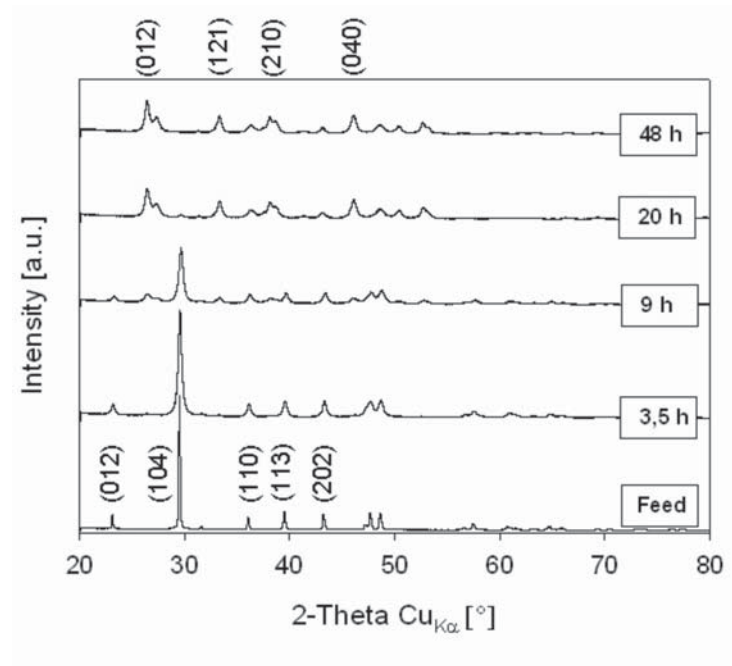
Figure 5.37.: X- ray diffraction patterns of CaCO$_3$ milled in ethanol at different grinding times

end of the milling procedure, nearly 100 % aragonite phase was detected in the suspension. As the aragonite crystallites reach their maximal value, the primary particle size seems to increase about 10 nm in size, before they were finally ground to a limiting diameter of about 35 nm. Further experiments were carried out under different stressing conditions and in a different dispersing medium. Although same stressing conditions were realized, no phase transition was observed during grinding in water. This leads to the conclusion that the phase transition is not only mechanically driven but also introduced by chemical processes. It is assumed that the solubility plays a major role in the phase transition mechanism.

However, pure stirring of the calcite feed material in ethanol does not show any changes in its crystalline composition. Hence, a combination of both mechanical and chemical aspects must enable the phase transition in ethanol. Therefore, the measured data have to be treated carefully, since solubility processes might go on after sampling and drying of the suspensions may cause a crystallization of solved ions, so that the measured BET and XRD results may be falsified. This effect and/or changes in the particle
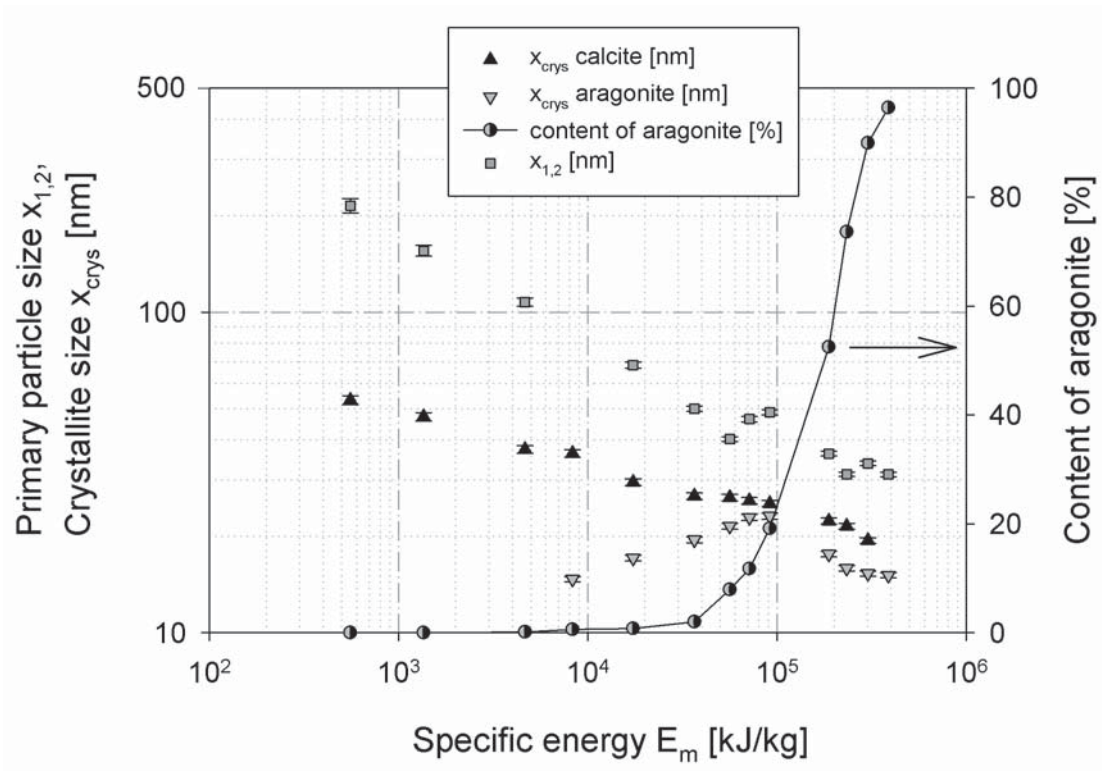
110

Figure 5.38.: Phase transition from calcite to aragonite during milling in ethanol

morphology during the phase transition might explain the observed (reproducible) increase of the primary particle size in the milling process. For the time being, the mechanism of the phase transition is not fully understood. Further investigations on this topic are in progress and may enlighten the observed findings.

5.6. Scale-up of nanomilling

For industrial applications, much larger suspension volumes have to be processed. Therefore, it is important to know if the grinding results in the laboratory scale are also valid in the industrial scale. The company NETZSCH Feinmahltechnik GmbH provides different kinds of stirred media mills in different size ranges. According to NETZSCH, the LabStar LS 1 is the smallest mill, which allows a scale-up of the grinding results to larger NETSZCH mills. In general, during scale-up of a stirred media mill, it is of great

importance to keep the ratio of power input P to the surface area of the grinding chamber A_{GC} constant in order to assure the same temperatures of the outlet suspension [Steh 06]:

$$\frac{P}{A_{GC}} = const \tag{5.6}$$

Concurrently, it has to be considered that the surface area of the grinding chamber does not scale linearly with the grinding chamber volume V_{GC}, but:

$$V_{GC} \propto D^3; \quad A_{GC} \propto D^2 \qquad \Rightarrow A_{GC} \propto V_{GC}^{2/3} \tag{5.7}$$

Under consideration that the same specific energy input leads to the same grinding result, Eq. 5.8 has to be followed:

$$E_m = \frac{P}{\dot{m}} = const \tag{5.8}$$

From the equations above, it results that the mass flow as well as the power input grow disproportionately with the milling chamber volume:

$$P \propto \dot{m} \propto V_{GC}^{2/3} \tag{5.9}$$

In the following experiments, the scale-up ability of the LabStar LS 1 to the larger stirred media mills Zeta RS 4 and LMZ 10 is investigated [Knie 11b]. As already discussed in chapter 3.1.2, both the specific energy input E_m and the stress energy (or stress number) has to be kept constant in order to achieve the same grinding result. Whereas suspension volumes of 2 l were processed in the LabStar LS 1, a 15 l approach and a 50 l approach were realized in the Zeta RS 4 and LMZ 10, respectively. A detailed overview about the conditions in the scale-up experiments is given in Tab. 5.4. In all experiments, alumina (CT 1200 SG) was used as feed material and a circuit mode comminution was chosen as operation mode. The setup is comparable to the setup of the LabStar LS 1 described in chapter 4.1.1. Since different grinding media materials were used in the investigations, the product related stress energy SE_P was used to specify the grinding conditions. The grinding results are shown in Fig. 5.39.

Table 5.4.: Overview about scale-up experiments

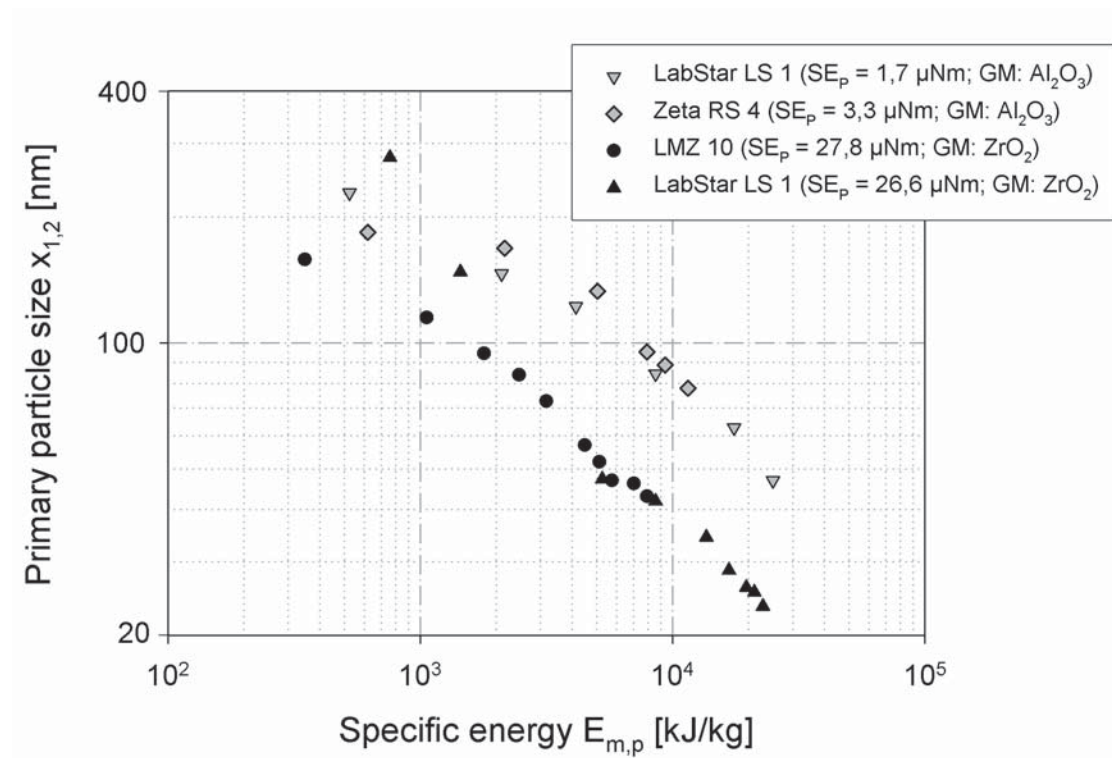|	2L APPROACH	15L APPROACH	2L APPROACH	50L APPROACH
Mill	LabStar LS1	Zeta RS 4	LabStar LS1	LMZ 10
V_{GC}	0.67 l	4 l	0.67 l	10 l
GM material	Al_2O_3	Al_2O_3	YSZ	YSZ
GM size	0.18 - 0.3 mm	0.18 - 0.3 mm	0.5 - 0.63 mm	0.4 -0.5 mm
Y_{GM}	400 GPa	400 GPa	265 GPa	265 GPa
c_m	47 wt%	49 wt%	20 wt%	59 wt%
v_t	8 m/s	11 m/s	8 m/s	11 m/s
SE_P	1.7 μm	3.3 μm	27.8 μm	26.6 μm

Figure 5.39.: Scale-up experiments of nanomilling

As can be seen in the diagram, the laboratory scale results and the industrial scale results are almost identical for same SE_P values and can be roughly described by straight lines for large specific energies. Differences are observed for small specific energy inputs which can be explained by the filling procedure at the beginning of the experiments. In the large scale experiments, huge powder volumes had to be slowly dispersed in the fluid

phase in order to avoid lump formation that can choke the sieve. It took more than half an hour to fill the LMZ machine with 32 kg of alumina powder in the 50 l experiment. During this time, the powder already passed the mill and was comminuted without detection of the power input. This results in smaller particle sizes related to a certain energy input.

However, small deviations in the grinding results can be explained by differences in the stress energy distributions as shown by Stender [Sten 02]. He presented that an upscaling of the grinding chamber geometry can lead to a different stress energy distribution in the milling chamber, so that the grinding results can no longer be described by the maximum stress energy SE_{GM} anymore. Instead a mean stress energy $\overline{SE}$ has to be introduced, which depends on the maximum stress energy SE_{GM} and an additional factor taking the stress energy distribution into account.

Nevertheless, a good scale-up ability was found for different NETZSCH mills by keeping E_m and SE_{GM} constant, so that the gained results of this work should be scalable to larger media mills without any difficulties.

5.7. The limit in dry grinding processes

Dry grinding processes are commonly carried out in planetary ball mills, in which the highest energy densities can be realized due to a superposition of two directions of motion. Planetary ball mills are often used in the field of mechanical alloying or as "mechano-reactors" for synthesis reactions. To fulfill the investigations concerning the grinding limit in ball milling applications, a rough discussion about the mechanisms in dry grinding processes is given in this section.

Therefore, two grinding experiments were carried out in the planetary ball mill PM 400 with different grinding media sizes. Again tin dioxide (Merck) was used as the feed material. A ratio of powder mass to grinding media mass of 0.05 was realized. Steel beads with a diameter of 3 mm and 28 mm were used as grinding media . In the experiment with the larger grinding media, only five beads were used. The sun wheel speed was set to 300 rpm in both experiments. The grinding process had to be interrupted at least every 1.5 h to allow a cooling of the machine. A total grinding time of

114

101 h was realized. During the milling operation a huge amount of powder stuck to the grinding media surface and the inner wall of the jars. Hence, the powder was scratched from the walls at different times to return it to the grinding process. Samples were taken at defined grinding times and were characterized by X-ray diffraction measurements since only a very low powder amount is necessary for this method. The samples were prepared by dispersing a certain powder amount in ethanol by means of ultrasonication and subsequently drying the suspensions on low background silicon wafers. Of the final powders additional BET measurements were carried out. During the grinding experiments, the temperature was controlled from time to time: at the outer walls of the milling jars, a temperature of about 44 °C and 56 °C was detected for the jar with the larger beads and the smaller beads, respectively. It can be expected that the temperatures inside the jars are much higher than measured at the outer walls. Since the power input cannot be recorded with the available mill, the evolutions of the crystallite sizes are presented as a function of grinding time in Fig. 5.40.
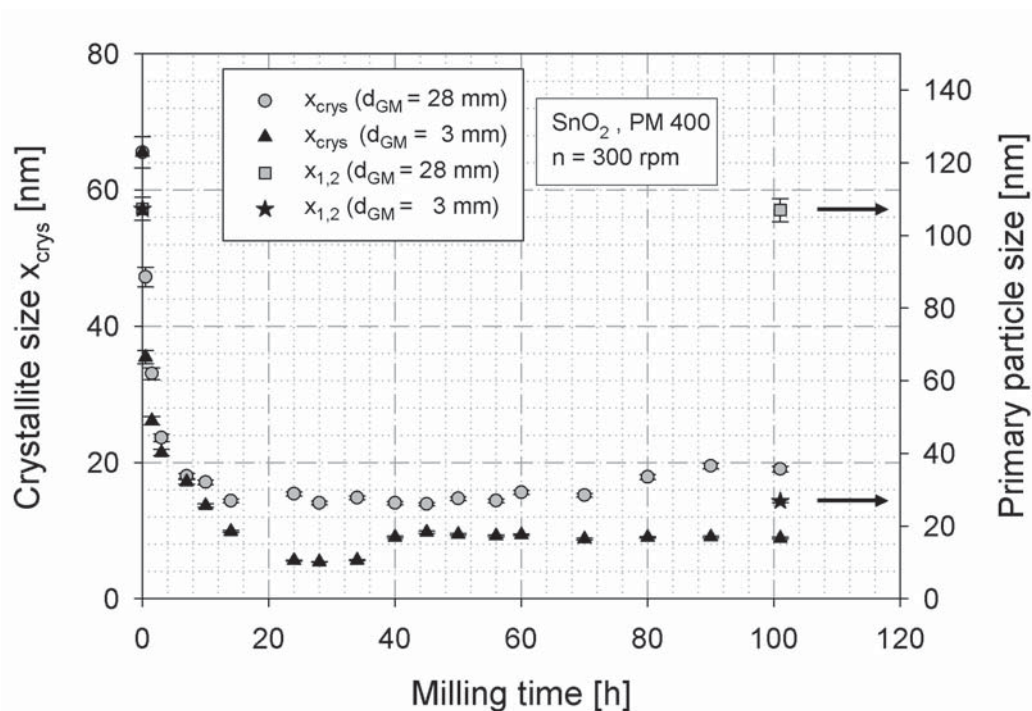

Figure 5.40.: Evolution of crystallite sizes during dry grinding of SnO_2 in a planetary ball mill

At the beginning of the grinding experiment, both curves exhibt a very similiar behavior: a fast domain size reduction from about 65 nm to 15 nm is observed within the first few hours of comminution. In the experiments with the 3 mm beads, the crystallite sizes decrease after a grinding time of 24 h to a minimal value of about 6 nm and stays almost constant for another 10 h, before the size increases to a final value of approximately 9 nm. These values are comparable to those reached in the wet grinding experiments. The development of the domain sizes using larger beads is slightly different: no distinct minimum can be detected. The achieved crystallite size of about 14 nm remains constant for more than 50 h of grinding treatment. After 80 h of stressing an increase in crystallite size to about 20 nm is observed. As these results show, the milling behavior during dry grinding with high impact energies is different to the grinding behavior in wet media milling. No increase of the crystallite size is observed during wet comminution, where a liquid phase causes a dampening of grinding media impact, acts as a spacer between the particles and transfers the produced heat. Hence, no welding takes place during wet grinding operations. During high-energy dry grinding, high local stresses and temperatures are acting, which can induce particle welding or even crystallite coalesence. As a consequence, an increase even in the crystallite size is observed. In a publication of Karagedov et al. [Kara 03], a scheme is presented for the particle and crystallite size evolutions during dry grinding in high-energy mills. This scheme is shown in Fig. 5.41.

Curve 3 represents the evolution of particle size, whereas curve 2 shows the development of the crystallite size. Both curves are determined by a superposition of size reduction and healing processes. The final equilibrium size depends on the rates of size reduction and recovery processes, which are both influenced by material and process parameters explaining the different size levels achieved in the experiment. During fine dry grinding, the particles remain typically polycrystalline, because welding of the primary particles occurs often as a consequence of the highly agglomerated powders. The achieved primary particle sizes confirm this consideration: the final size is around 106 nm in the case of the larger beads, which is almost identical with the initial powder size and the final particle size using the
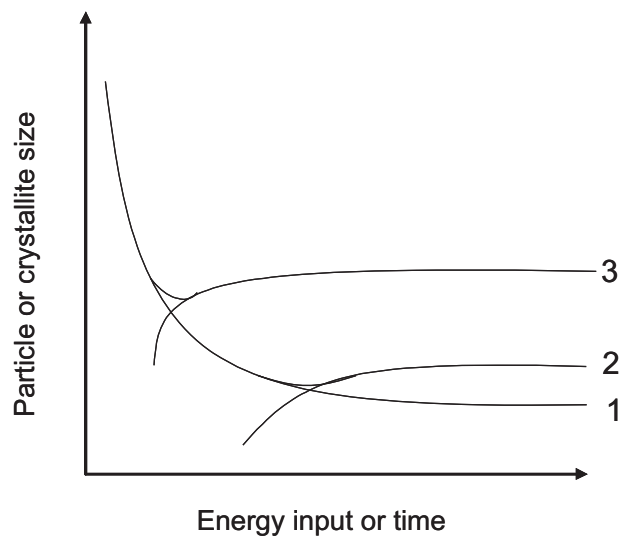
116

Figure 5.41.: Schematic evolution of particle and crystallite sizes during dry grinding [Kara 03]

smaller grinding media exhibits a value of 27 nm. Curve 1 represents the theoretical evolution of crystallite size if only size reduction without any welding processes occurs. In this case, a limiting size is also observed. Eckert defined this size limit as the size of a crystallite that can just sustain a dislocation pile-up within its lattice [Ecke 95]. Since no recovery occurs during wet grinding (otherwise the grinding limit would depend on process conditions), the limit in curve 1 represents the grinding limit in wet media milling, which can be regarded as an overall limit in grinding operations because is it mainly determined by the material itself. The equilibrium size in dry milling applications can be described according to Eckert with the diagram presented in Fig. 5.42.

The steady state or equilibrium grain size can be regarded as the size where the recovery rate (A/B; solid curves) equals the refinement rate (G_1/G_2; dashed lines). Larger recovery rates and/or smaller refinement rates will shift the steady state size to larger values (e.g. $d_2 \rightarrow d_1$). Whereas the refinement rate yields a linear dependency on grain size, the recovery processes are more complicated. The main driving force is the energy stored in the grain boundaries. With decreasing grain size, the grain boundary area drastically increases leading to a higher driving force for recovery. The
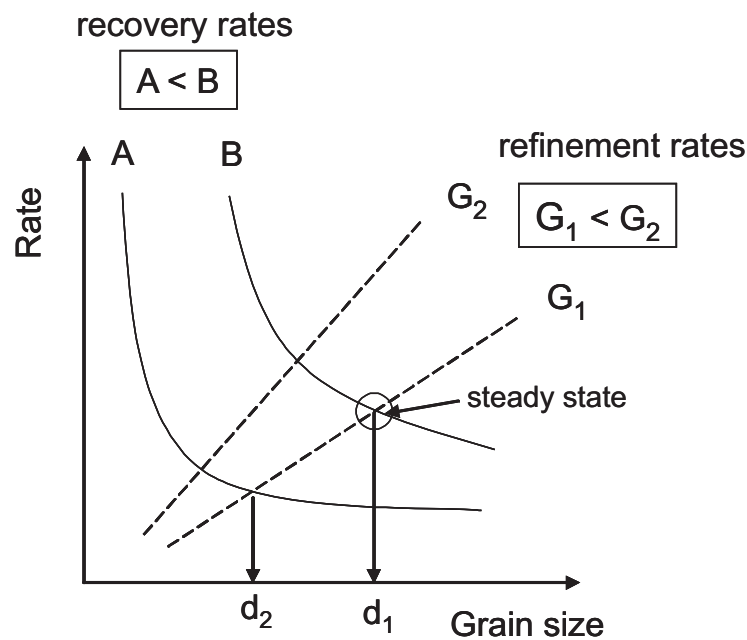
117

Figure 5.42.: Equilibrium size as function of refinement and recovery rates [Ecke 95]

observed minimum in the experiments (mainly in the experiment with the smaller grinding media) can be ascribed by either a non-steady state conditions due to a time shift between refinement and recovery processes or by an increase in recovery rate for long grinding times shifting the equilibrium size to larger values. An increase in recovery rate can be caused, for instance, by an increase in temperature or an increase in grain boundary energy due to a highly distort structure or change in the composition (e.g. solute atoms from grinding media attrition). It is expected that the larger crystallite sizes in the experiment with the larger grinding beads are caused by both, a smaller refinement rate due to the low number of milling beads and a higher recovery rate resulting from the large impact intensities.

Finally, the question arises how these findings can be brought into line with the discussions about the grinding limit in wet media milling. In dry milling, the size reduction is overlaid by recovery processes causing the achieved sizes to be larger, which is observed clearly for the primary particle size and for the crystallite sizes in the case of the larger beads. The final crystallite sizes in the experiment with the 3 mm balls, exhibit almost the same size than in wet milling. This indicates that the recovery rate using small grinding beads is very small. That even smaller grain sizes (6 nm) are obtained than

the claimed limit of grinding for tin dioxide (10 nm) can be explained by a larger degree of amorphization during dry milling, because no liquid phase dampens the bead impacts.

The amount of grinding media attrition was identified by weighing the grinding beads before and after the experiment. A total weight loss of 3 wt % was observed for the larger beads and a weight loss of about 3.5 wt % was found for the smaller ones. Since no additional phases were found in the X-ray diffraction patterns, it is assumed that the iron attrition is amorphous.

Altogether, a limit in size reduction is also observed in dry grinding processes. Whereas welding phenomena does not allow a strong size reduction of the primary particle size, a very fine microstructure is obtained. Due to a superposition of grain refinement and recovery, the achieved crystallite sizes are a little larger than obtained in wet grinding operations. However, reducing the recovery rate by using smaller grinding beads, comparable grain sizes can be reached.

6. Delamination of Graphite

So far, the breakage behavior of brittle oxide and non-oxide materials in the nanometer range has been investigated. These materials show strong bond forces almost independently from the orientation within their crystalline lattice. For most systems, a more or less isotropic breakage behavior resulting in globular fragment sizes is observed unless the particles are not completely squeezed flat as a result of very high stress energies. In the following chapter, the breakage investigations will be extended to another material class, the layered systems. Layered materials are characterized by a lamellar structure and a strong anisotropy in the bond forces. A typical example of a layered material is the graphite crystal, which was chosen as a model system in this study. Some of the results presented here are already published in [Knie 10a].

Graphite is built up from parallel graphene sheets which are stacked together with a distance of 0.335 nm. Between the sheets, only weak van der Waals forces exist, whereas strong covalent bond forces are acting within a layer where the carbon atoms are arranged in a hexagonal lattice. From this anisotropy in the bond forces, a strong anisotropy in the mechanical, thermal, and electrical properties of graphite crystal originates. Since the discovery of stable graphene sheets by Novoselov and Geim in 2004 [Novo 04] with a simple "scotch-tape method", the one atom thick carbon material has attracted great interest because of its outstanding properties. Since that time, scientists have been trying to find new production routes for this unique 2-D material. Mechanical methods are predicted to provide graphene materials with the highest quality since no oxidation of the bulk material is necessary and the produced sheets are not connected to a carrier material that may affect the outstanding properties. Although there had been intensive research to develop new synthesis routes (see chapter 2.3), a high-yield production of graphene is still challenging for the time being.

6.1. Breakage behavior of graphite

6.1.1. Preliminary experiments

As already described by other groups in literature, layered materials tend to delaminate under mechanical shear stress. A flake formation was observed by milling graphite particles in a planetary ball mill in n-dodecane from Milev et al. [Mile 08] and Janot et al. [Jano 02]. Also in an electrical mortar grinder, a delamination of graphite particles dispersed in water was observed under low energy pure shear milling [Anti 06]. The produced graphite flakes exhibit a thickness in the order of 10 nm. In the context of the discussion about the limit of grinding, the question arises how thin a graphite sheet can become in a milling process. Under the consideration that a strong industrial demand exist for very thin sheets down to graphene monolayers with a large lateral dimension, the production of graphite flakes with high aspect ratios is investigated in the following.

As feed material for the grinding experiments which were carried out as batch mode comminution in the laboratory stirred media mill PE 075 (NET-ZSCH, Feinmahltechnik GmbH, Selb, Germany), a synthetic graphite (GS 6, Remacon GmbH, Bad Säckingen, Germany) with a median particle size of about 4 μm was used. A SEM image of the feed material is given in Fig. 6.1.
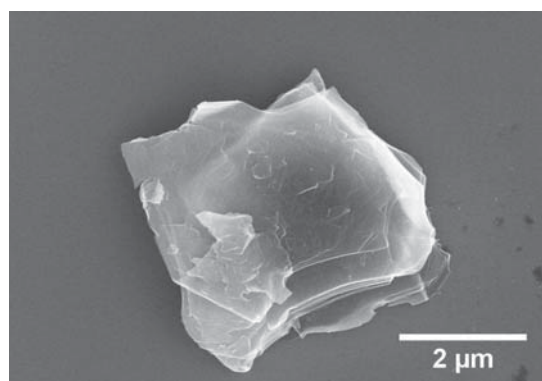

Figure 6.1.: Synthetic graphite GS6 (feed material)

In the SEM image, the layered structure of the graphite particle can be clearly recognized. For the grinding experiments, the graphite particles have to be dispersed in a liquid medium. In terms of an economic and nonhazardous process, de-ionized water was used as the solvent in the delamination experiments. To allow a wetting of the nonpolar graphite surface by water, the anionic surfactant sodium dodecyl sulfate (SDS) was added. The surfactant molecules adsorb on the particle surface resulting in a high negative charge. Electrostatic forces between the particles and delaminated sheets prevent agglomeration and lead to stable suspension conditions. Since the surfactant is only physically bound on the particle surface, an adsorption-desorption equilibrium prevails and free surfactant molecules are always present in the solvent. To reach an optimal stabilization of the delaminated sheets, an appropriate concentration of SDS is necessary. By means of surface tension measurements, the adsorption isotherm of SDS on the graphite surface was determined. A defined amount of graphite with known surface area was added in different concentrated surfactant solutions and shaken for about 12 h at room temperature to reach equilibrium conditions. Afterwards, the graphite particles were centrifuged and the surface tensions of the supernatants were measured and compared with the surface tensions of the pure surfactant solutions. From the differences in the concentrations without and with the former presence of graphite at same surface tensions, the adsorbed amount of surfactant on the graphite surface could be calculated. Fig. 6.2 presents the adsorption densities of SDS molecules on the graphite surface as a function of equilibrium concentration.

The adsorption isotherm exhibits two plateau regions. According to Zettlemoyer, this effect can be ascribed by a change in conformation of the SDS molecules on a graphitic surface [Zett 68]. At the lower plateau, the molecules lie parallel to the graphite surface resulting in a lower packing density. With increasing SDS concentration, the conformation changes to a molecular arrangement perpendicular to the graphite surface. Wanless et al. found by means of AFM measurements that SDS molecules adsorb as hemicylindrical structures resulting in higher packing densities [Wanl 96]. As can be seen in Fig. 6.2, the graphite surface is completely covered with SDS molecules at an equilibrium concentration of about 5.5 mmol/l. It should be noted that this concentration is below the critical micelle concen-
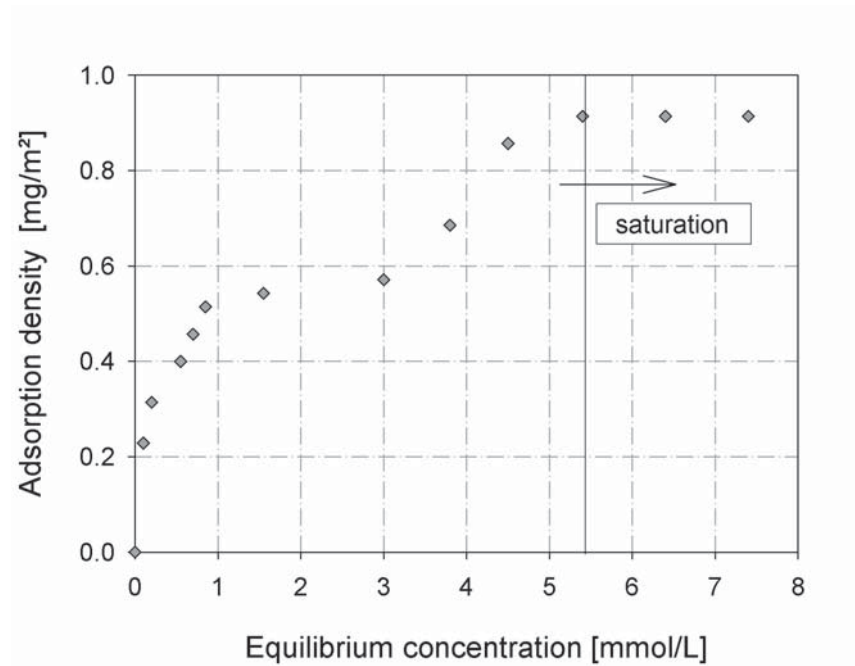
Figure 6.2.: Adsorption isotherm of SDS on graphite particles in water

tration of 8.1 mmol/l (25 °C) [Haya]. In subsequent grinding experiments a concentration around the saturation concentration was chosen. Thus, the formation of micelles that may influence the stability of the suspension was avoided.

In the milling process, the graphite particles are stressed between the milling beads. Compressive and friction forces act on the particles and can lead to a delamination of thin graphite sheets. This selective, orientation-dependent size reduction is enabled by the anisotropy in the bond forces inside the graphite crystal. The aspect ratio of the produced flakes strongly depends on the process parameters of the milling procedure. The acting shear forces have to be large enough to overcome the weak van der Waals forces between the graphene sheets. Concurrently, the compressive forces have to be reduced that no in-plane fracture occurs. Hence, mild milling conditions are necessary to obtain sheets with high aspect ratios. Fig. 6.3 shows SEM images of delaminated graphite sheets resulting from the stressing of a 1 wt% graphite suspension in the stirred media mill using 100 μm zirconia beads. The sheets are well dispersed and separated on the sili-

124

con wafer. In the right image, the surface of a stressed graphite particle is shown. A thin flexible graphite layer is crumpled and partially folded on the graphite surface. The peeling procedure for this sheet was not completed at the end of the experiment.
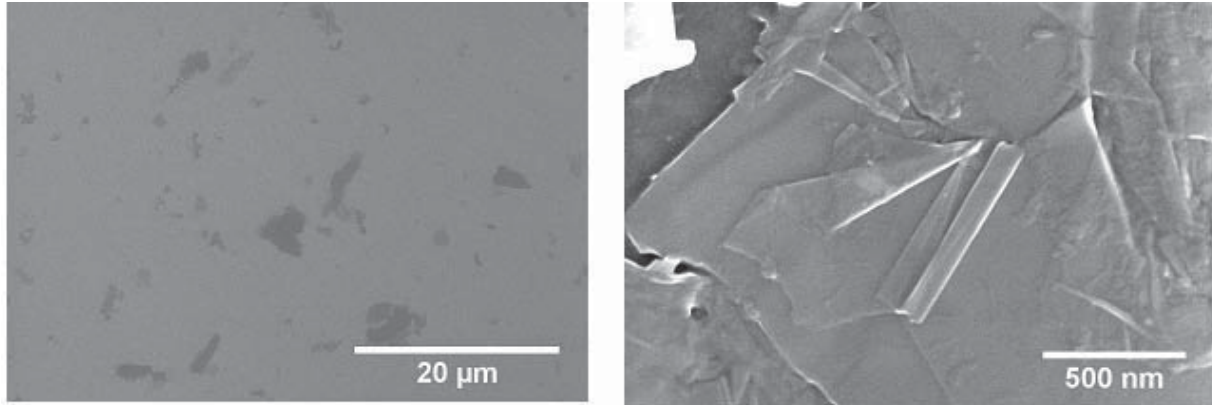

Figure 6.3.: SEM images of stressed graphite particles: highly dispersed flakes (left); partially folded sheet on top of graphite particle (right)

The SEM images confirm the expected formation of thin graphite flakes under mild milling conditions. The produced suspensions are highly stable against agglomeration and sedimentation. The anionic surfactant molecules adsorb on the graphite particles and lead to a high negative charge on the surface. Zeta-potentials of about -50 mV could be achieved indicating stable suspension conditions. No settling of the suspensions was observed even after months of rest.

6.1.2. Mechanism of delamination

First of all, the question arises if a pure shear flow can transfer the necessary energy to reach a delamination of thin sheets from a thick graphite particle. Delamination takes place if the acting shear forces overcome the attractive van der Waals forces between the sheets. A graphite particle in a pure shear flow with the important dimensions is schematically shown in Fig. 6.4. The shear force acting on the front wall of a sheet with the thickness h_1 and the width b can be calculated using the following equation:

$$F_{shear} = \sigma_{shear} \cdot A = \dot{\gamma} \cdot \eta(\dot{\gamma}) \cdot b \cdot h_1 \qquad (6.1)$$
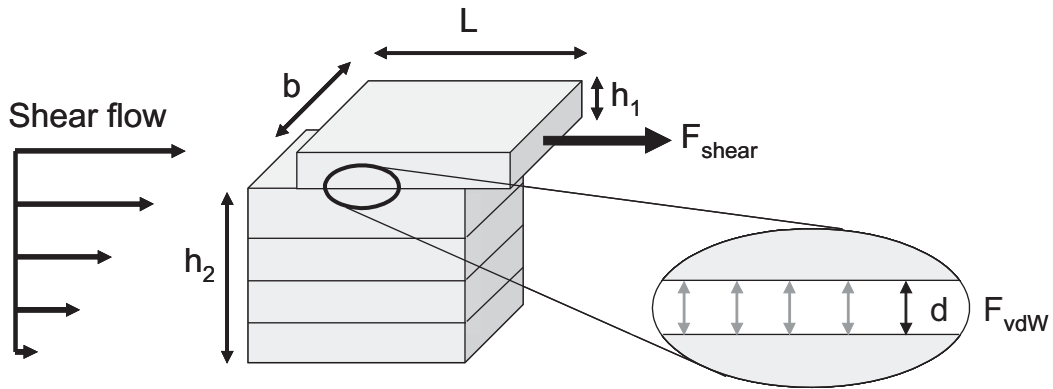
125

Figure 6.4.: Schematic graphite particle in a shear flow

This force has to be larger than the van der Waals force between the sheet and the remaining particle of the thickness h_2. F_{vdW} can be calculated according to Tadmor [Tadm 01] as

$$F_{vdW} = \frac{A}{6\pi}\left(\frac{1}{d^3} + \frac{1}{(d+h_1+h_2)^3} - \frac{1}{(d+h_1)^3} - \frac{1}{(d+h_2)^3}\right)\cdot b\cdot l \quad (6.2)$$

In Fig. 6.5, the available shear force and the van der Waals force are illustrated as a function of sheet thickness h_1. The values used for the calculations are summarized in Tab. 6.1. The thickness of the remaining particle was set to 4 μm, which equals the median size of the graphite particles used in the experiments.

Table 6.1.: Values used for the calculations in Fig. 6.5.

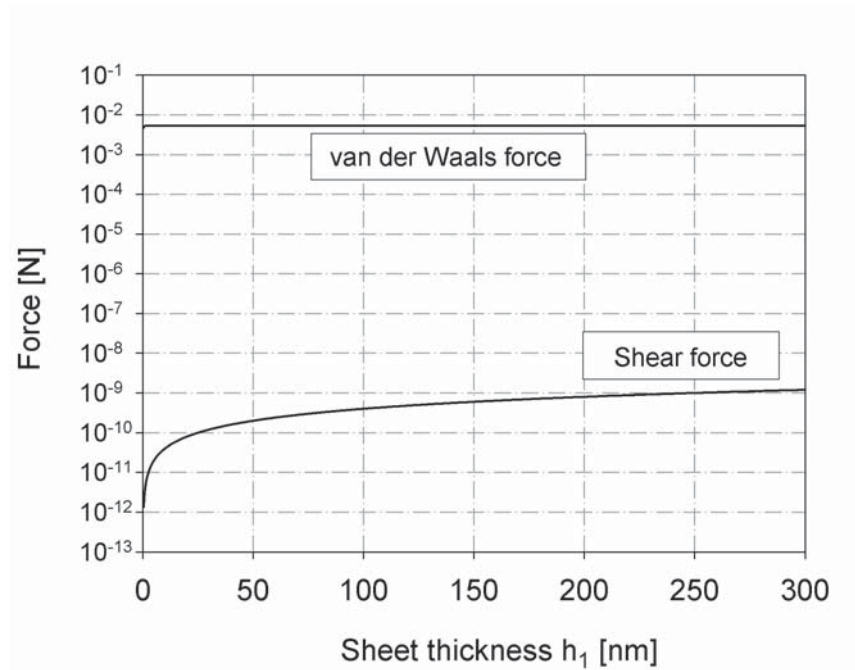| DIMENSION	PARAMETER	VALUE
$\dot{\gamma}$	shear rate	1000 s^{-1}
$\eta(\dot{\gamma})$	dynamic viscosity	1 Pas
d	interlayer distance	0.335 nm
h_1	thickness of delaminated sheet	varied
h_2	thickness of remaining particle	4 μm
b	width of delaminated sheet	4 μm
l	length of delaminated sheet	4 μm
A	Hamaker constant of graphite	2.38·10^{-19} J [Dryz 94]

126

Figure 6.5.: Comparison of shear force and van der Waal force as a function of sheet thickness

As can be seen in Fig. 6.5, the acting van der Waals force is much larger than the available shear force. The van der Waals force is almost constant and shows a decrease to smaller values only for very thin sheet thicknesses, whereas the shear force directly scales with h_1. Nevertheless, for the given conditions no delamination of the graphite is possible in a pure shear flow. Intercalating the graphite and increasing therewith the interlayer distance, will strongly reduce the attractive forces between the graphene sheets. Additionally, higher viscosities as in the case of polymer melts, for instance, will enhance the shear forces, so that both values achieve the same order of magnitude for very thick platelets. However, for non-intercalated feed particles, additional forces are required to reach a delamination of thin sheets. In a stirred media mill, graphite particles are stressed between moving milling beads. Compressive and friction forces act on the particles so that a delamination of thin graphite sheets can be realized in a kind of peeling process. In Fig. 6.6, possible delamination mechanisms in the presence of grinding beads are schematically shown.
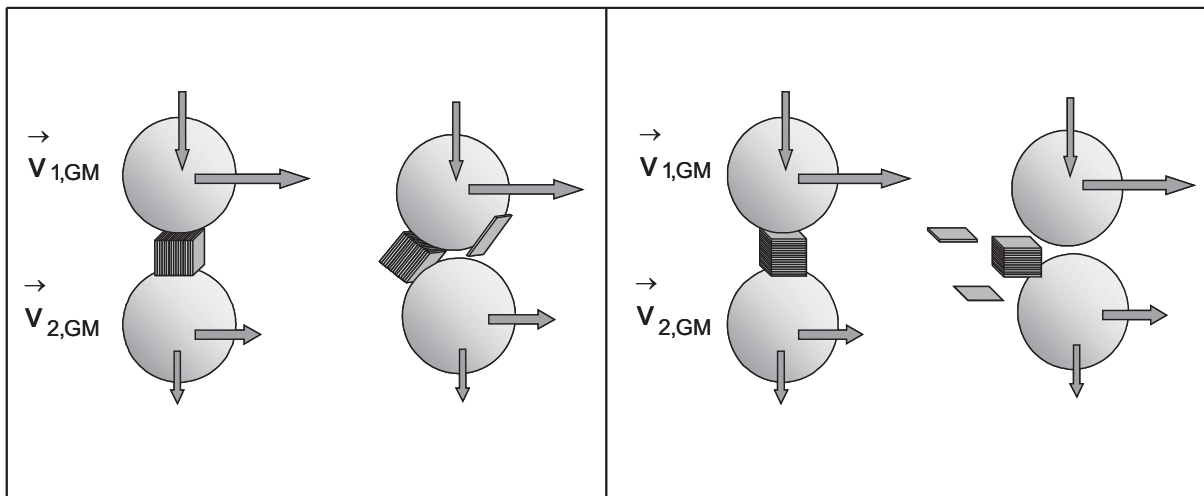
127

Figure 6.6.: Delamination mechanisms: normal force induced delamination (left); shear force induced delamination (right)

Which mechanism takes place, depends on the orientation at which the graphite particles are trapped between two colliding milling beads. If the particle is caught with the graphene layers in direction of the shear forces, a shear or friction force induced delamination occurs (right image). If the particle is caught with the sheets oriented in the direction of the normal forces, the particle will be squeezed between the beads and the resulting delamination is normal force induced (left image). The acting normal forces can be calculated from the relative velocities between two colliding beads. The friction (shear) force is directly proportional to the available normal force according to the Coulomb's law of friction. Friction forces result between bodies with different velocities under the presence of normal forces as illustrated in Fig. 6.7 for a graphite particle on a flat substrate with zero velocity and a moving grinding bead.

The resulting friction force acts in the opposite direction of the bead velocity v_{GM}. According to the Coulomb's law of friction, the resulting friction force can be calculated by

$$F_F = \mu \cdot F_N \tag{6.3}$$

where μ is the friction coefficient, which is in first approximation independent of the bead velocity. For a zirconia bead rubbing on the surface of highly oriented pyrolytic graphite (HOPG) plate, a friction coefficient
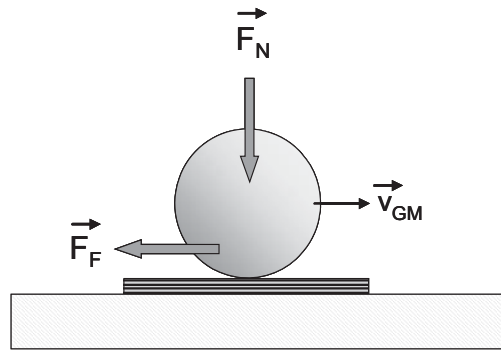
Figure 6.7.: Acting forces on a graphite plate during rubbing with a grinding bead

of 0.13 was determined in tribology measurements (UMT-3, CETR Inc., Cambell, USA). Hence, reducing the normal forces by a reduction of stress energy is always connected with lower friction forces for the delamination process.

Now the questions arise whether the transferred energies from the grinding beads are sufficient to reach a delamination of thin graphite sheets and if a peeling of thin sheets from the surface or a cleavage of the graphite into two halves is the dominating size reduction mechanism. To answer these questions, a closer look on the interaction energies in a graphite crystal is necessary. Borse et al. investigated the delamination behavior of clay particles dispersed in a polymer solution under pure shearing [Bors 09]. It was calculated that the stress required for cleavage of a clay particle is much higher than that for peeling thin sheets from the particle surface. The interaction energy E_A per unit area between two graphite plates of the thickness h_1 and h_2 can be determined in analogy to the van der Waals force with the parameters summarized in Tab. 6.1 using Eq. 6.4 [Tadm 01].

$$E_A = \frac{A}{12\pi} \left(\frac{1}{d^2} + \frac{1}{(d + h_1 + h_2)^2} - \frac{1}{(d + h_1)^2} - \frac{1}{(d + h_2)^2} \right) \qquad (6.4)$$

In Fig. 6.8, the interaction energy per unit contact area is presented as a function of sheet thickness h_1. With increasing thickness, the interaction energy between the two plates increases until a nearly constant energy is
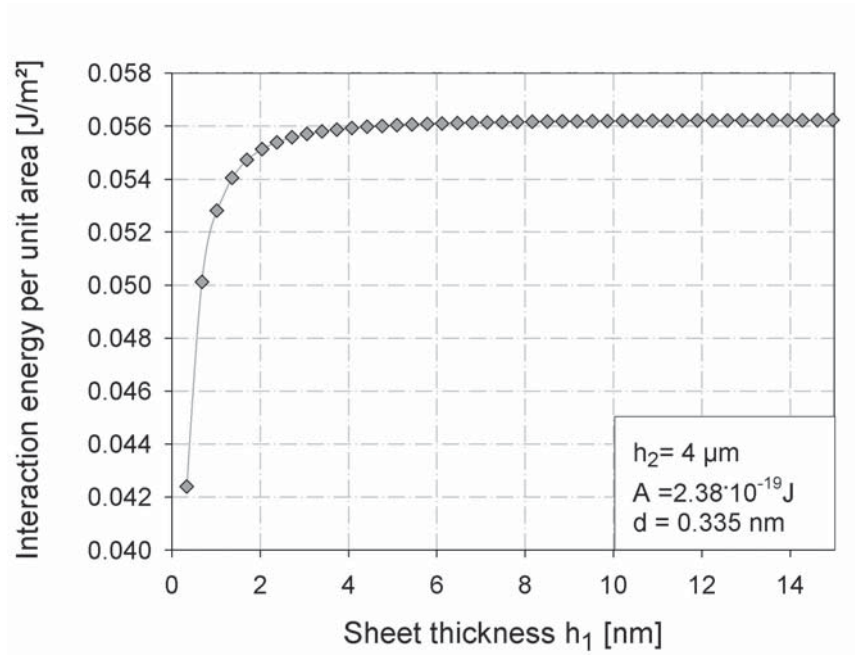
Figure 6.8.: Interaction energies per unit area between two plates of finite thickness

reached. The plateau is already reached at small thicknesses of h_1, because $d << h_1$, h_2 and therewith the first term in the brackets determines E_A. However, the mechanism of peeling only few layers from the graphite surface is energetically more likely. From the above analysis, the energy required to peel a 4 μm x 4 μm single layer platelet from a thick graphite particle can be estimated to be $90 \cdot 10^{-14}$ J. This energy has to be overcome by the grinding media. Since neighboring grinding media move in the same direction, the difference of both kinetic energies $\Delta E_{kin,P}$ can be transferred in maximum. Additionally, it also has to be taken into account that a fraction of the total grinding media energy is consumed for elastic deformation of the grinding beads and thus, has to be considered in the equation. Under the assumption that no energy is consumed for the acceleration of slower milling beads and the liquid phase, the energy transferred to the graphite particles can be expressed according to Kwade [Kwad 99] by:

$$\Delta E_{kin,P} = \frac{\pi}{12} \cdot \rho_{GM} \cdot d_{GM}^3 \cdot (v_{GM,1}^2 - v_{GM,2}^2) \cdot \left(1 + \frac{Y_P}{Y_{GM}}\right)^{-1} \qquad (6.5)$$

The parameters used for the calculation of $\Delta E_{kin,P}$ are given in Tab. 6.2.

130

Table 6.2.: Parameters for the calculations of the transferred energies

PARAMETER	SYMBOL	VALUE
Density of the grinding media	ρ_{GM}	6050 kg/m^3
Diameter of the grinding media	d_{GM}	100 μm
Velocity of faster bead 1	$v_{GM,1}$	2.35 m/s
Velocity of slower bead 2	$v_{GM,2}$	2.349 m/s
Young's modulus of the product	Y_P	230 GPa
Young's modulus of the grinding media	Y_{GM}	265 GPa

The complex movement of the grinding media in the milling chamber results in a wide velocity distribution. The velocity of the faster bead $v_{GM,1}$ was set to half of the circumferential velocity of the stirrer. For the velocity of the slower bead, a mean relative velocity of 1 mm/s was assumed. This value was estimated from bead velocity gradients determined by Particle Tracking Velocimetry measurements of an index-matched mill setup carried out at the Institute of Mechanical Process Engineering in Braunschweig [Theu 99]. According to Eq. 6.5 and Tab. 6.2, the minimal transferred energy of the milling beads can be determined to be about $400 \cdot 10^{-14}$ J, which is larger than the required energy determined above for delaminating a graphene sheet from a 4 μm thick particle. In addition, it cannot be discounted that the peeling procedure might also occur stepwise due to repeated stressing between the grinding media with lower individual transferred energies. These theoretical considerations have been confirmed by experimental observations, which showed that even after short grinding times ultrathin sheets already exist in the milled suspensions. Therefore, cleavage of the graphite particle into two halves cannot be the predominant mechanism while mechanical peeling from the surface seems to be more likely.

6.2. Characterization of delaminated sheets

The characterization of the delaminated sheets was carried out with different methods in this work. Especially atomic force microscopy and Raman spectroscopy are powerful tools for the detection of graphene monolayers.

Atomic force microscopy

In order to determine the exact thickness of the sheets AFM measurements were carried out. The samples were centrifuged (Centrifuge 5418, Eppendorf AG, Germany) for 60 s with a revolution speed of 3000 rpm prior to the spin-coating to remove the still unpeeled feed particles from the suspensions. After spin-coating the supernatants on cleaned SiO_2-wafers, a thin surfactant film still remains on the surface of the flakes. Accordingly, the real heights of the measured sheets by AFM technique will be slightly overestimated. To remove the surfactant from the particle surface, the coated wafers were washed with de-ionized water. By means of Auger electron spectroscopy, which was carried out at the Institute of Surface Science and Corrosion, Department of Materials Science and Engineering at the University Erlangen-Nürnberg, it was evidenced that putting a coated wafer for at least 5 minutes into a water bath will remove nearly all SDS molecules from the surface. Since SDS molecules will also exist between the sheets and the wafer, the washing procedure also removes some sheets from the wafer's surface. Fig. 6.9 shows the typical topography of graphite sheets after a 5 h grinding treatment and subsequent washing.

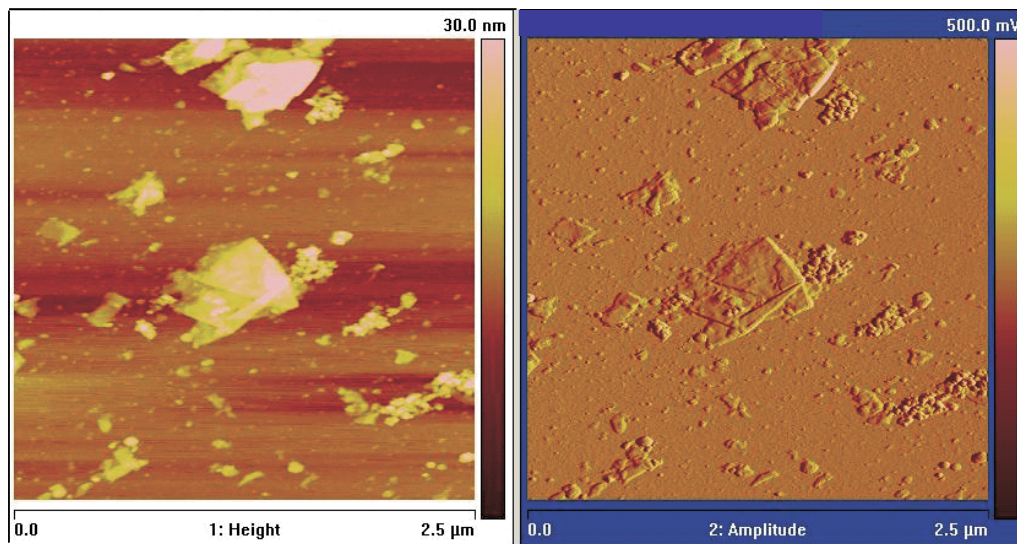
Figure 6.9.: AFM topography of delaminated sheets (left) and amplitude profile (right)

After peeling the initially 4 μm thick graphite particles in the media mill, mainly flat structures with thicknesses less than 10 nm are found in the

132

sample. Nevertheless, some of these structures are already broken into smaller fragments, indicating that either the stressing time or the stress intensity was too large. Hence, for future processing, it is advisable to continuously remove the already peeled sheets in a mechanical separation unit in order to avoid an overstressing of the produced sheets. The smallest sheets that could be detected in the samples yield heights of only 1 nm. In Fig. 6.10, the thinnest structures are illustrated. The sheets were produced by grinding a 1 wt% graphite suspension in water with sodium dodecyl sulfate as stabilizer. The concentration of SDS in water was set to the critical micelle concentration. 100 μm YSZ beads were used as grinding media. The grinding experiment was carried out for 5 h with a stirrer tip speed of 4.9 m/s. After spin coating the centrifuged sample, the wafer was put into a water bath for 5 minutes and dried afterwards under ambient conditions.
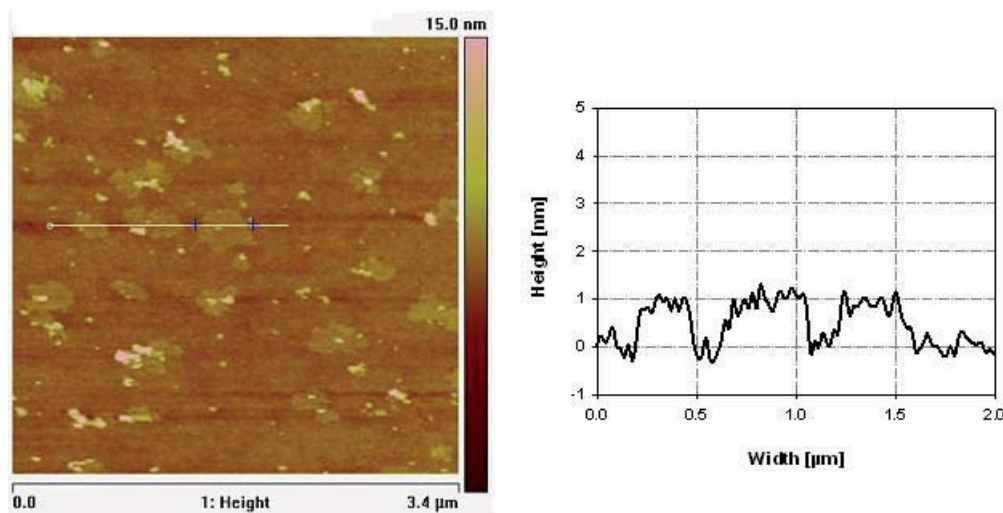
Figure 6.10.: AFM topography of graphene monolayers (left) and related height profiles (right)

The height profiles of the thinnest sheets show a thickness of about 1 nm, which can be considered as a monolayer for measurements under atmospheric conditions [Loty 09], [Ishi 07]. Additionally, residual moisture in the sample also increases the measured heights of the sheets. The lateral dimension of the flakes is about 0.5 μm, so that an aspect ratio of 500 is achieved. However, to give evidence of graphene monolayers, exclusive AFM

measurements are not sufficient, since they only exhibit information about the morphology and not about the chemical structure. It would be theoretically possible, that the measured thin structures belong to another material which is present in the sample. Therefore, additional analysis techniques have to be carried out to confirm the presence of graphene monolayers.

Raman spectroscopy

Raman spectroscopy is a powerful tool to determine the exact number of graphene layers for sheets with up to five layers. Graphitic materials can be characterized by a D-band (~ 1350 cm^{-1}), a G-band (~ 1580 cm^{-1}), and a 2D-band (~ 2700 cm^{-1}). The symmetry, the full width at half maximum (FWHM) of the 2D-peak as well as the intensity ratio of 2D to G-band can be used to distinguish between monolayer, bilayer, or multilayer graphene sheets [Graf 07], [Ferr 06]. Defects in the graphene lattice, which break the translational symmetry result in the presence of a D'-band. In addition, the ratio between D and G peak intensities I(D)/I(G) comprises information about the point defect density in single layer graphene sheets as long as the defects are Raman active [Canc 11].

The Raman spectrum shown in Fig. 6.11 was detected with a single stage spectrometer and an excitation energy of 2.33 eV. Therefore, delaminated sheets were deposited on top of SiO$_2$ wafers to enhance the Raman signal. The Raman measurements were carried out by C. Barthold (Institute of Particle Technology) and J. Englert (Institute of Organic Chemistry II). The Raman spectrum clearly comfirms the presence of graphene monolayers in the sample. First of all, the 2D-band is symmetric and can be fitted by one single peak, which is a major evidence for a graphene monolayer. Also the FWHM of the 2D-band with 29 cm^{-1} and the ratio of the intensities of 2D to G-band which is clearly larger than 1 verify that the analyzed material is graphene. Furthermore, the existence of a D'-band (~ 1620 cm^{-1}) indicates the presence of defects. Since the flakes have a lateral dimension which is smaller than the laser spot, these features may originate from edge effects. Besides graphene monolayers also thin multilayer sheets as well as thicker graphitic flakes were identified by their Raman signature, which is in good agreement with the AFM observations.

134
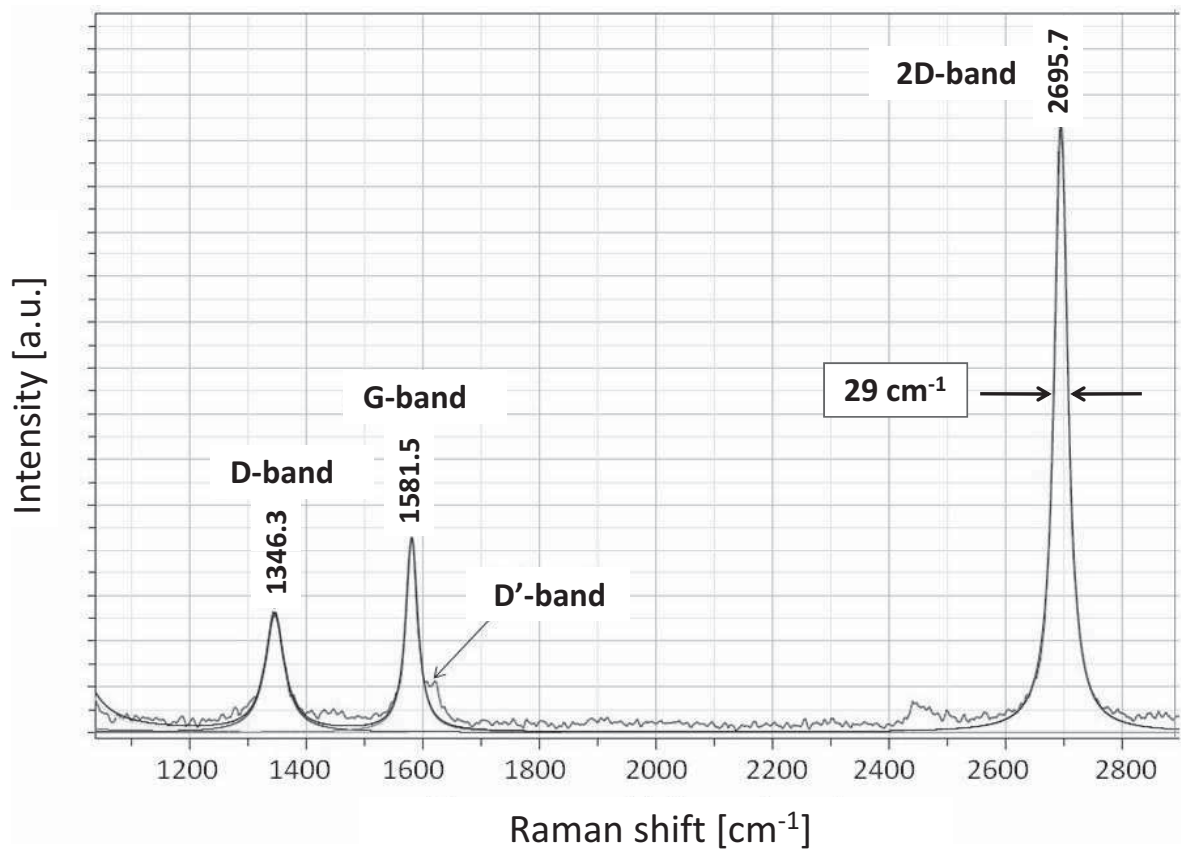
Figure 6.11.: Raman spectrum of delaminated graphene sheets

X-ray photoelectron spectroscopy

To investigate if the milling procedure causes defects in terms of oxides which strongly determine the electrical properties of the delaminated sheets, XPS measurements have been carried out at the Institute of Surface Science and Corrosion, Department of Materials Science and Engineering at the University Erlangen-Nürnberg. In the left diagram of Fig. 6.12, the normalized C1s spectra of the initial graphite powder and delaminated powder which was stressed for 5 h in the stirred media mill are compared. Both XPS spectra are almost identical. Hence, no oxidation of the initial graphite occurs during the grinding treatment. Nevertheless, fitting procedures show that besides the C-C line at a binding energy of 284.7 eV, some additional

lines are required to fully explain the spectrum. The right diagram shows the spectrum of the milled sample, which can be fitted beside the C-C line by a weak C-O peak (286 eV) and C=O peak (287.2 eV), respectively. The background of the spectrum has been removed. Hence, small amounts of oxygen are present in the samples. Since the milling procedure does not introduce further oxygen defects, the oxygen content could be reduced by using a feed material with a higher purity.
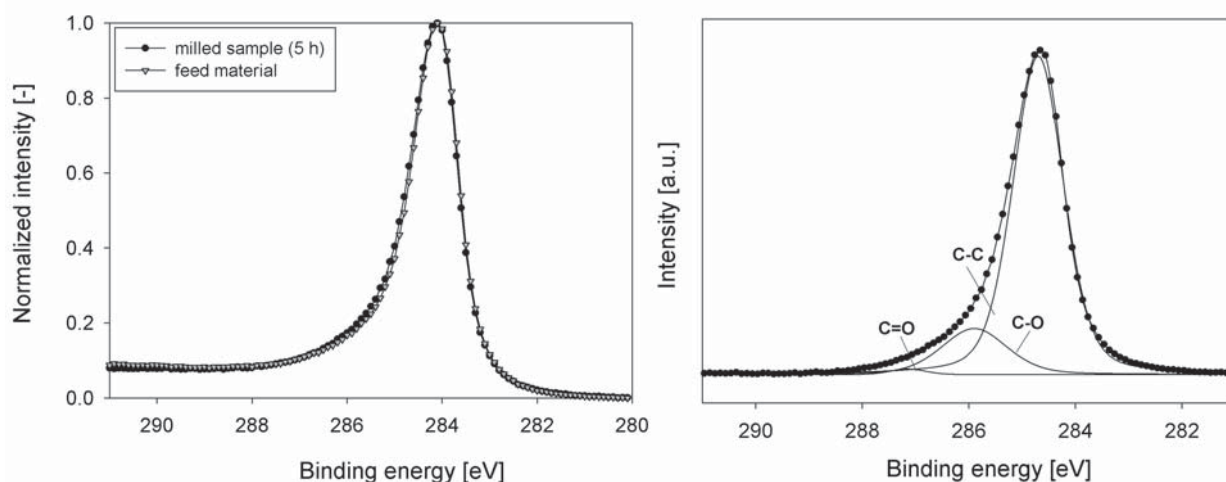

Figure 6.12.: C1s XPS spectra of milled and initial graphite powder (left); fitted C1s XPS spectrum of the milled sample (right)

HR-Transmission electron microscopy

HR-TEM investigations were carried out on a sample milled for 24 h with 50 μm grinding media and standard composition (1 wt% graphite content, c(SDS) = cmc). The sample was centrifuged (10000 rpm for 10 minutes, centrifuge 5418, Eppendorf AG) to remove thick fractions which may overlay the thinnest sheets in the microscope images. Afterwards, the sample was washed three times by a complete centrifugation of the sample and replacement of the supernatant with de-ionized water. Most of the SDS molecules should be removed from the flakes after the washing treatment. It is necessary to detach the surfactant molecules from the sample surface, because they can decompose in the electron beam of the TEM and affect the images. In Fig. 6.13, HRTEM images of the sample are given.

136
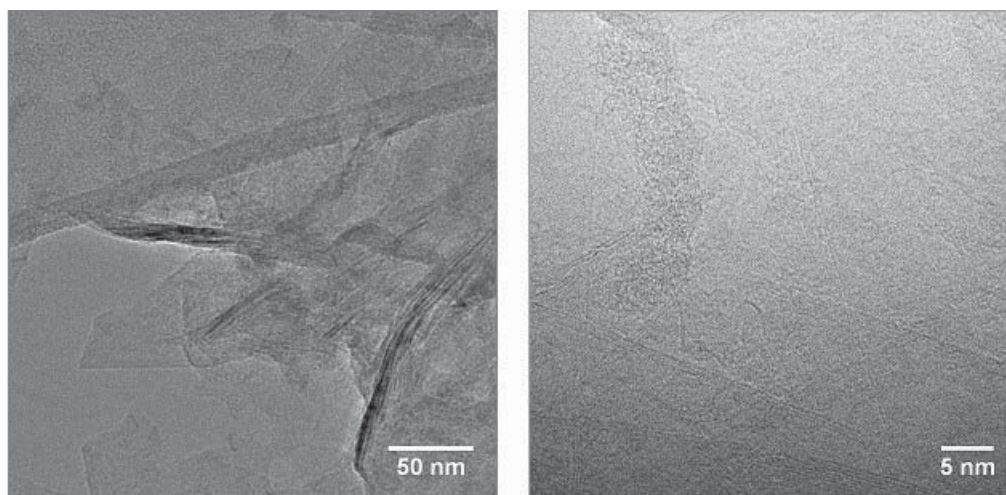
Figure 6.13.: HRTEM images of peeled graphite sheets

Very thin graphite layers can be detected in the sample. In some cases the sheets are so thin that they can hardly be visualized. In the right image some lines of dark contrast can be seen. Each line represents a single graphene monolayer. Having a closer look, mono-, bi-, three-, and multilayer parts in the sample can be discovered. Since the layers are strongly accumulated (the stabilizer was removed before the sample preparation), it is not possible to distinguish if the whole sheet consists of only one or two graphene layers or if only a part of a thicker sample is illustrated. In Fig. 6.14, another thin sheet is shown where the number of graphene sheets can be detected more clearly.

The image shows the side view of the delaminated flake. In total, the flake consists of five graphene layers stacked together. The outer endings of the sheets are slightly expanded, which facilitates further peeling in the milling process.

Figure 6.14.: HRTEM image of a thin graphite layer (side view)

X-ray diffraction

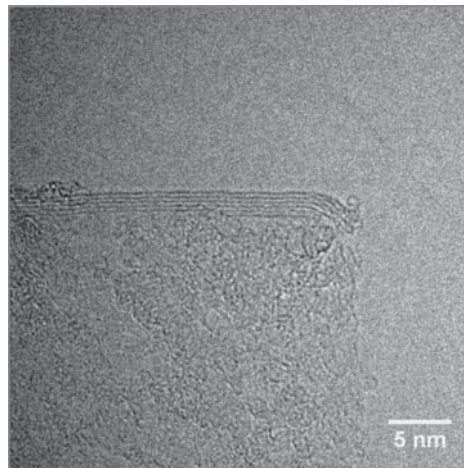X-ray diffraction can be used to analyze on the one hand the thickness and the lateral dimension of domains in the graphite particle and on the other hand it is possible by means of a Rietveld refinement to investigate the mean d-spacing between the graphene sheets. If solvent molecules or stabilizing agents intercalate between the sheets, the c lattice parameter will increase. In pristine graphite, the d-spacing exhibits a value of 3.35 Å, whereas in acid treated graphite (graphite oxide), the interlayer spacing can increase to about 6 - 7 Å. In the following table, the thickness of the graphite domains as well as the interlayer spacing of a milled sample and the feed material are summarized. The values are obtained by a Rietveld refinement of the (002)-peak in the diffraction pattern, which represent the c axis in the graphite crystal.

Table 6.3.: Domain thickness and interlayer spacing of pristine and milled GS6

Sample	Domain thickness	Interlayer spacing
GS6 Feed	68 nm	3.350 Å
Milled 5 h	65 nm	3.367 Å
Milled 5 h, centrifuged	23 nm	3.366 Å

During a 5 h grinding treatment, the domain thickness is hardly reduced. This can be explained by the continuous peeling process from the graphite

surface. Therefore, the domains located in the inner graphite particles remain untouched. As will be shown in chapter 6.4, the most part of the material is not peeled off after a grinding time of 5 hours at the given conditions. A much smaller grain thickness is obtained in the centrifuged sample. Here, the thicker unpeeled particles were separated from the suspension and only finer structures remained in the sample. Since not only thin delaminated sheets but also broken fragments are produced in the milling treatment, the measured domain thickness gives a median value of all detected grains on the sample holder. The interlayer spacing stays almost constant, which signifies that neither water nor surfactant molecules intercalate between the graphene sheets.

6.3. The role of stress energy

As already mentioned above, the transferred energy from the grinding media is proportional to their kinetic energy. High transferred energies from the grinding media can cause in-plane fracture of the sheets and mainly small graphite fragments are present in the final suspensions. The stress energy SE was used as a measure for the maximum energy of the grinding media, because an exact calculation of the velocity distribution is difficult. Since there exists a cubic dependency of the stress energy on the grinding media size, the most effective method to reduce SE is the use of smaller milling beads. To investigate the morphology of delaminated sheets at different stressing conditions, AFM statistics have been carried out. The height profiles and the lateral dimensions of 300 flakes were measured per experiment. In the grinding experiments, the following conditions apply: graphite (GS6) dispersed in water with SDS, 1 wt% solid content, surfactant concentration 8.1 mM (= cmc), grinding time 5 h, rotational speed 1500 rpm (v_t= 4.9 m/s). Only the grinding media size was varied in the experiments. To avoid any falsification of the statistics by unintentional removal of graphite sheets, the washing procedure to remove the surfactant described above was omitted. This led to an overall increase in the measured heights of the flakes. If a SDS molecule is completely stretched, its length can be estimated to be 1.6 nm [Coir 86]. Hence, if the SDS is adsorbed on both sides of the

flake, an increase in the overall sheet height up to 3.2 nm is possible. Another source of error could be the formation of thin SDS sheets which might influence the distributions in Fig. 6.15 till Fig. 6.17. The unambiguous determination of sheets with less than roughly 3-5 layers is possible by Raman mapping. For the characterization of thicker sheets counting by AFM is currently unavoidable. By the use of 100 μm yttria stabilized zirconia grinding media, stress energies of 0.134 μJ are achieved. In Fig. 6.15, the resulting thickness distributions (density and cumulative distribution) are shown. $Q_0(h)$ is the cumulative number distribution, which describes the amount of all flakes that have a thickness equal to or smaller than a certain thickness h.

Figure 6.15.: Thickness distributions of graphite flakes stressed with SE = 0.134 μJ; number density distribution (left), cumulative distribution (right)

From the thickness distribution, the mean value h_{50} was determined to be 2.7 nm, i.e. more than 50 % of the created sheets are thinner than 3 nm. Reducing the grinding media size to 50 μm and keeping all other parameters constant, stress energies of 0.0167 μJ are obtained. The corresponding thickness distributions after a stressing time of 5 h are presented in Fig. 6.16.

Although the reduction in SE resulted in a slightly larger h_{50} value, the total thickness distribution becomes narrower if smaller beads were used. In total, more than 97 % of the sheets are thinner than 5 nm when smaller
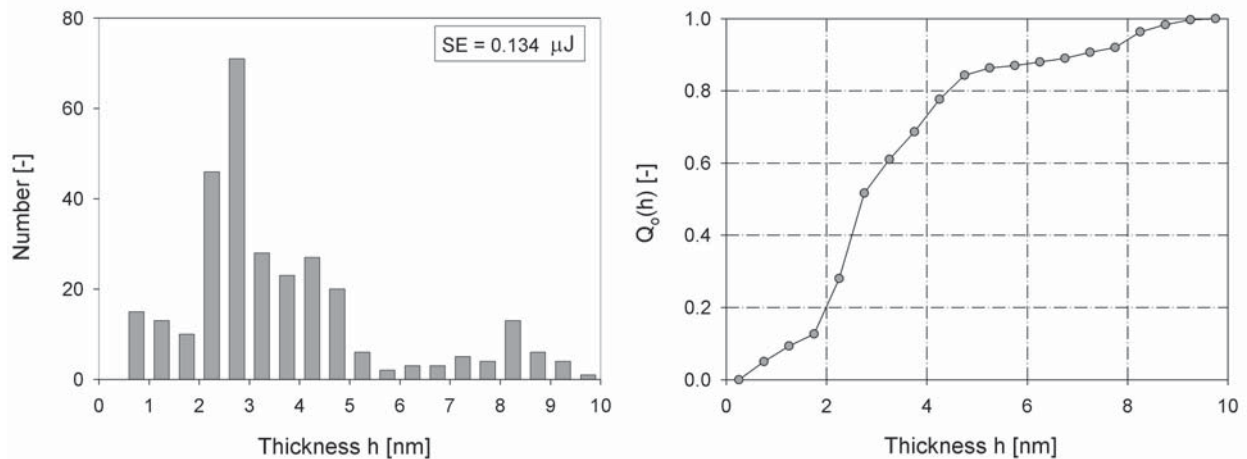
140
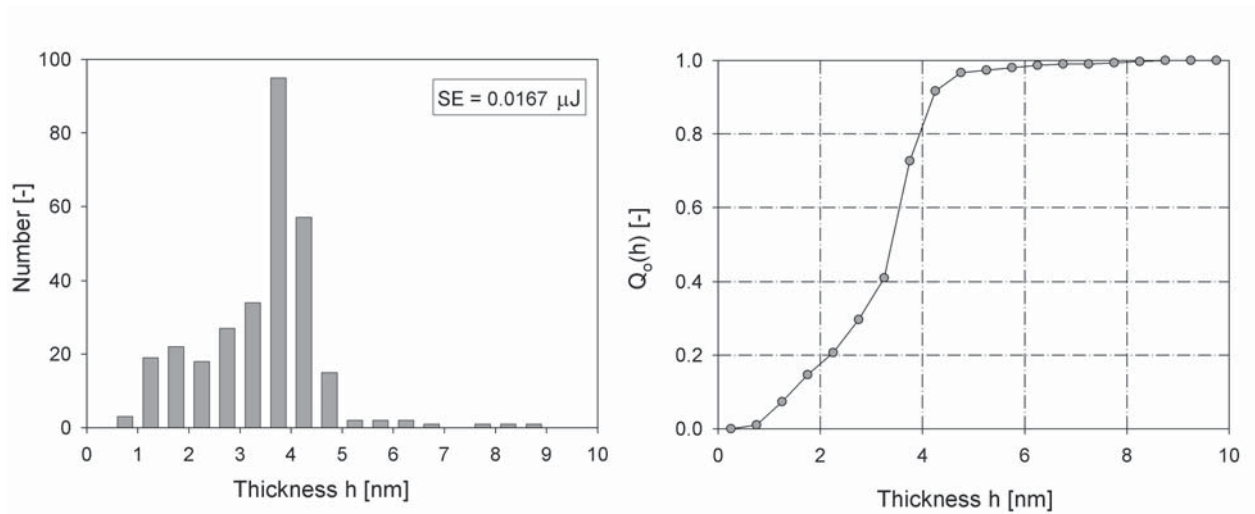
Figure 6.16.: Thickness distributions of graphite flakes stressed with SE = 0.0167 μJ; number density distribution (left), cumulative distribution (right)

grinding beads are used compared to only 86 % when larger stress energies are realized. In addition to the thickness distributions, the lateral dimensions of the sheets were measured for the discussed stressing conditions. The resulting cumulative distributions are compared in Fig. 6.17.
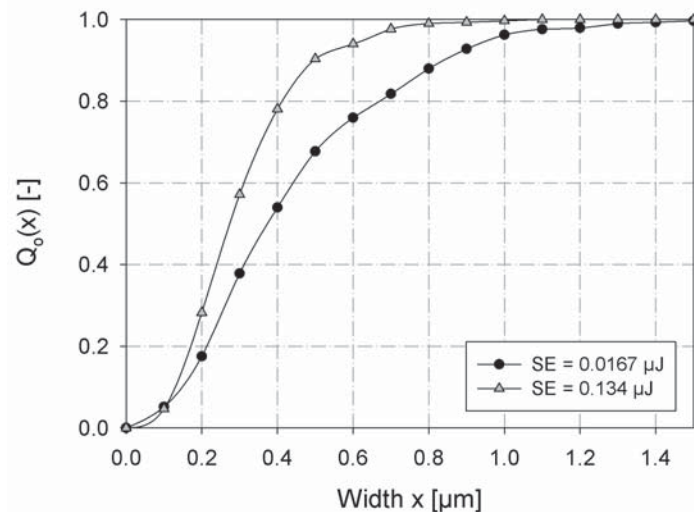
Figure 6.17.: Cumulative distributions of the lateral sheet dimension at different stress energies

The width of the produced sheets varies from about 100 nm to more than 1 μm. With increasing stress energy by almost one order of magnitude, the resulting size distribution is only slightly shifted to smaller lateral sizes of the sheets. As expected, a larger degree of in-plane fracture occurs if the stress energy is enhanced. Still unknown at this point is the role of the domain size in the graphite particle. It is assumed that the domain size especially in the lateral dimension is much smaller than the extension of the overall particle. Hence, fracture can be facilitated due to the disturbance of the grain boundaries so that a size reduction takes place even at smooth stress conditions. Nevertheless, the presented results clearly show that the morphology of the delaminated sheets can be controlled by the parameters of the milling process. Even larger sheets may be produced by choosing larger feed particles with larger domain sizes and optimized stress conditions.

6.4. Yield of delaminated sheets

In addition to the morphology of the sheets, the question about their yield is of great importance especially for economical reasons in industrial applications. Samples that were taken at different grinding times consist in general of both: already delaminated sheets and still unpeeled thicker graphite particles, which can easily be separated by centrifugation (Eppendorf centrifuge 5418, operating conditions: 60 s at 3000 rpm). The supernatant contains delaminated sheets as well as small fragments after the centrifugation. One possibility to estimate the carbon content in the supernatant is by the measurement of the optical absorption (UV-Vis spectroscopy) at a constant wavelength ($\lambda = 660$ nm). By means of calibration curves, the optical absorption of the sample can be assigned to a certain graphite concentration. Since the particle size and shape have an influence on the extinction coefficient, calibration curves were detected for different sizes (determined by CPS disc centrifuge, DC 24000, Lot Oriel Group). To consider the shape effect is much more complicated, because the determination of the sheet morphology of every sample by means of AFM statistics would be too time-consuming. In addition, a broad distribution of the aspect ratio is always present in the suspensions. Hence, for the generation of the calibration

curves, already milled samples, which are assumed to have a comparable morphology to the later investigated samples, were used. The calibration curves are presented in Fig. 6.18. To avoid multi-scattering and therewith a falsification of the measured concentrations, the samples were highly diluted in an appropriate background solution. To investigate the delamination process, samples were taken at different grinding times. After removal of the unpeeled thicker feed particles by centrifugation, the concentration was estimated from the particular calibration curve for a given median size. If the measured size was in between two calibration curves, the value was interpolated. The samples of the supernatant with increasing stressing time (from left to right) are illustrated in Fig. 6.19. It is obvious that the samples are getting increasingly darker with peeling time, indicating an enhanced concentration of delaminated sheets in the supernatant.
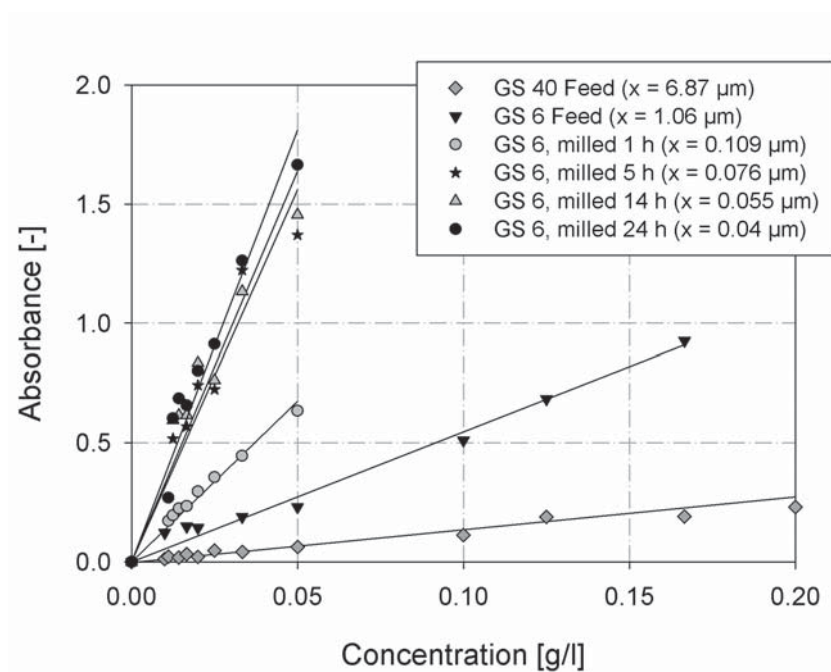
Figure 6.18.: Calibration curves: Absorbance as a function of carbon concentration for different particle sizes

An almost linear dependency of the graphene sheet concentration in the supernatant with peeling time was detected. This observation confirms the proposed mechanism of a continuous peeling process of the graphite particles between the grinding media. Starting with a solid content of 1 wt%, a

Figure 6.19.: Supernatants with increasing milling times (from left to right)

concentration of about 1 g/l of delaminated sheets could be achieved after a peeling time of 3 h. Hence, 10 % of the graphite particles had been delaminated under the chosen stressing conditions. In Fig. 6.20, the influence of solid content in the initial suspensions on the yield of delamination is presented.
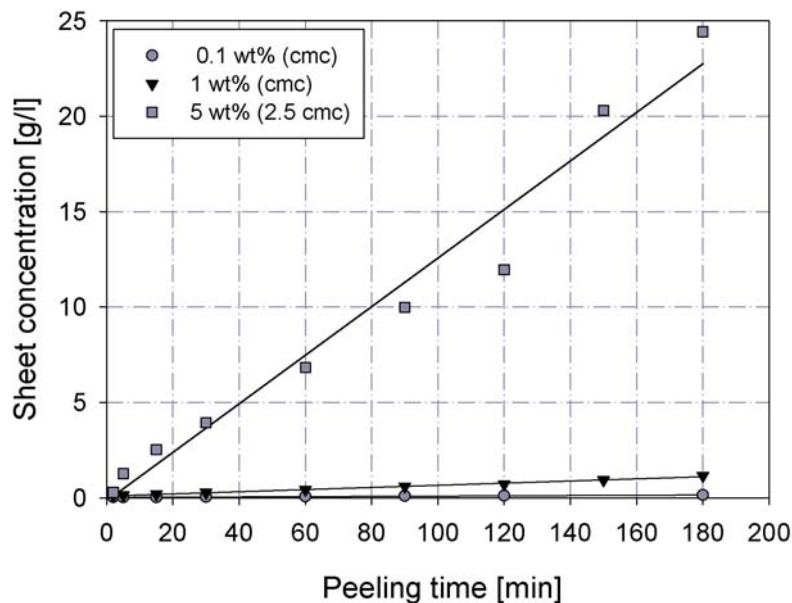
Figure 6.20.: Delamination kinetics as a function of solid content in the milling suspensions

Increasing the solid content leads to a higher yield of thin sheets as expected. Since a larger surface area has to be covered with surfactant at a solid content of 5 wt%, the amount of SDS was adjusted to 2.5 times the cmc. Milling a 5 wt% graphite suspension leads to a carbon concentration of about 25 g/l after a stressing time of only 3 h. It has to be taken into ac-

144

count, that the measured concentrations not only reflect the concentration of peeled sheets, but also small broken fragments, which could not be removed in the centrifugation step. Nevertheless, the achieved concentrations of mono- and multilayer graphene sheets in the presented process are much higher than those, which could be reached by the existing solution-based methods so far [Park 09]. In summary, stirred media milling as a scalable low cost process is capable to provide huge amounts of high-quality delaminated sheets down to graphene monolayers, which can directly be processed to the desired application.

6.5. First examples of application

Although the presented process is not optimized for the time being, first possible applications were started to be realized. Since graphene yield outstanding electrical properties and also graphite is an excellent in-plane conductor, their use as filler in polymers or as material for conductive films is of great importance, especially if their electrical properties are accompanied with an optical transparency. In the following, some first "proof of concepts" for possible applications are presented.

6.5.1. Production of filled polymers

As already mentioned, one important application for graphene materials is their use as filler in polymers to enhance their electrical and mechanical properties. Especially transparent and simultaneously conducting polymers have a broad application field and can be used as conductive coatings or films, for instance. In order to retain the optical transparency as well as the elastic properties of the polymer, low filler contents are required. This implies a homogenous distribution of the filler material in the polymer matrix as well as a good attachment of the polymer chains on the particle surface. Several other parameters are also known to influence the properties of the composite material such as filler content, filler size and shape, or the orientation of the filler material in the polymer. One characteristic of filled polymers concerning electrical properties is the percolation threshold, at which the filler material has built a conducting network throughout

the entire sample resulting in a drastic increase in conductivity. Based on theoretical considerations from Xie et al. graphene-based composites are predicted to have a slightly higher conductivity than those reinforced by nanotubes with the same volume fraction caused by the two dimensional structure of graphene [Xie 08]. In 2006, Stankovich et al. presented the first prepared graphene-based composites, which were produced from reduced GO dispersed in a polystyrene matrix [Stan 06a]. The composites yield an excellent conductivity even at very low filler contents and the achieved percolation threshold of 0.1 vol.% is the lowest reported value for any graphene-based composite material to this day.

The composites fabricated in this work are based on polyvinyl alcohol, because it is water-soluble and can be easily mixed with the aqueous graphene-SDS-suspensions. The milled samples were suspended in a 10 wt% PVA-water solution and were dried on special epoxy resin plates with interdigitated Cu electrodes for the impedance measurements. To remove the humidity in the samples which is known to strongly influence the electrical properties [Ogur 97], the samples were additionally dried in an exsiccator. In Fig. 6.21, the conductivity of different composites as a function of frequency and graphite filler content is given.

At low frequencies, the electrical conductivity is determined by the pure Ohm's resistance of the sample, which is independent of frequency. The increase in conductivity at high frequencies can be related to an intrinsic capacitive effect of the Impedance Analyzer. Hence, to describe the properties of the samples, the conductivities at low frequencies (extrapolated to zero frequency) are used in the following. The graphite sheets were produced in a 10 h grinding experiment under standard conditions (1 wt% solid content, 100 μm YSZ grinding media, c(SDS) = cmc, v_t= 4.9 m/s). Only the sample with 17 wt% filler content was produced under slightly different conditions: instead of the surfactant SDS the polymer PVA was used as stabilizer, also larger grinding media with a diameter of 0.3 - 0.4 mm were used to overcome the enhanced viscosity of the suspension. The results show an increase in conductivity of several orders of magnitude with graphite filler content as expected. A clearer illustration is given in Fig. 6.22 where the conductivity at zero frequency is plotted against filler content.

146
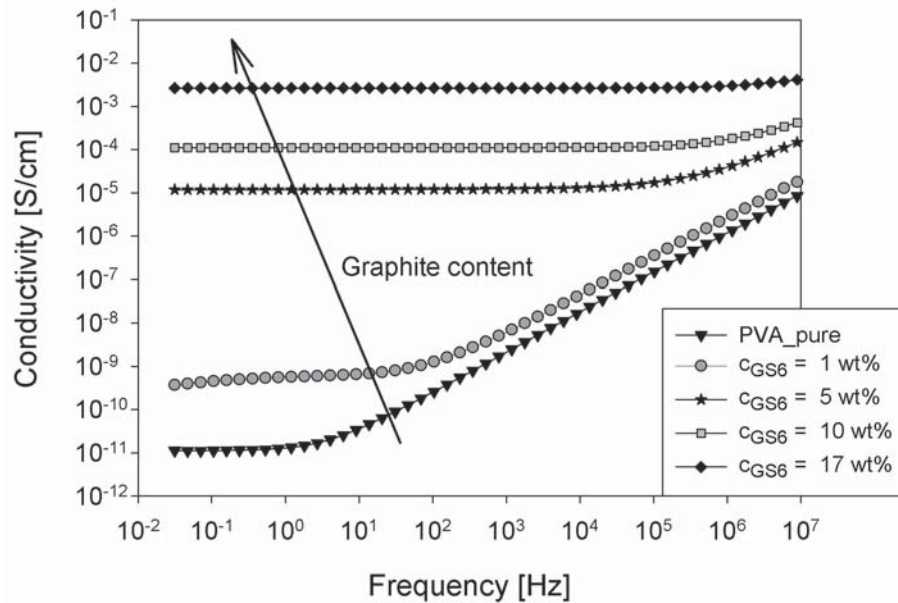
Figure 6.21.: Impedance measurements of PVA composites with different graphite filler contents

At low filler contents, a steep increase in conductivity is observed, whereas at high graphite concentrations the conductivity reaches saturation. Above the percolation threshold, the electrical conductivity of a composite can be treated with a power law, since the following correlation applies [Sand 03]:

$$\sigma \propto (p - p_c)^t \tag{6.6}$$

where p is the content of the graphitic filler, p_c the percolation threshold and σ the conductivity of the composite. To determine the percolation threshold of the composite, a so called "percolation plot" is designed with p_c as the fit parameter. The percolation plot of the investigated graphite-PVA system is given in the right diagram of Fig. 6.22. Attention has to be paid since only very few composites with different filler contents were investigated. Nevertheless, a percolation threshold is estimated from the plot as a rough approximate value. A filler content of $p_c = 0.55$ wt% (= 0.3 vol%) was shown to give the best fit values. This threshold is still larger than the current state of the art value of $p_c = 0.1$ vol% for graphene filled polystyrene, obtained by Stankovich et al. in 2006 [Stan 06a]. To
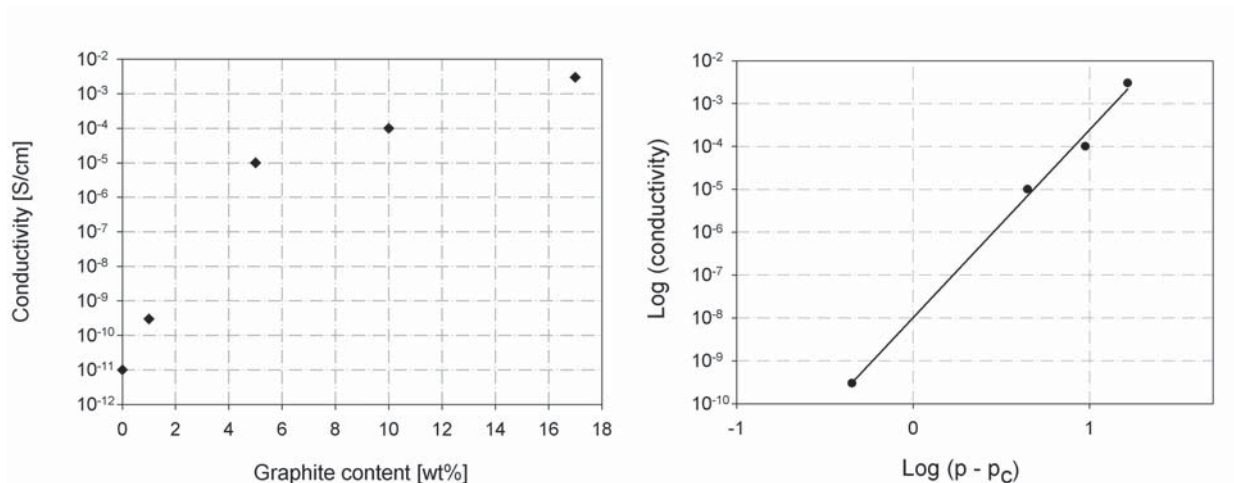
Figure 6.22.: Conductivity of graphite-PVA composites as function of filler content (left); related percolation plot (right)

get an impression of the influence of milling on the conductivity of the composites, samples with milled and unmilled graphite particles (both 5 wt% filler content) are compared in Fig. 6.23.

It can be seen that the milling process improves the conductivity by about 4 orders of magnitude. A subsequent drying step will further increase the conductivity, because the removal of residual humidity will cause a shrinkage of the composite resulting in a closer graphite network.

6.5.2. Preparation of conductive films

Another application for the produced graphene suspensions is their processing to conductive films. Therefore, the suspensions were dried on cleaned glass plates (10 mm x 10 mm x 1 mm), which were additionally plasma treated. Since spin-coating leads to the formation of very inhomogeneous films, some droplets were spread on top of the glass plates and dried under atmospheric conditions. With this method, homogeneous and closed films are obtained. The conductivity of the films was determined with the 4-point probe methods, where 4 electrodes were put in line on the film surface. Through the outer electrodes, a defined current is applied, whereas the resulting voltage between the inner ones was detected. In contrast to the 2-point probe method, a 4-point measurement eliminates the lead re-

148
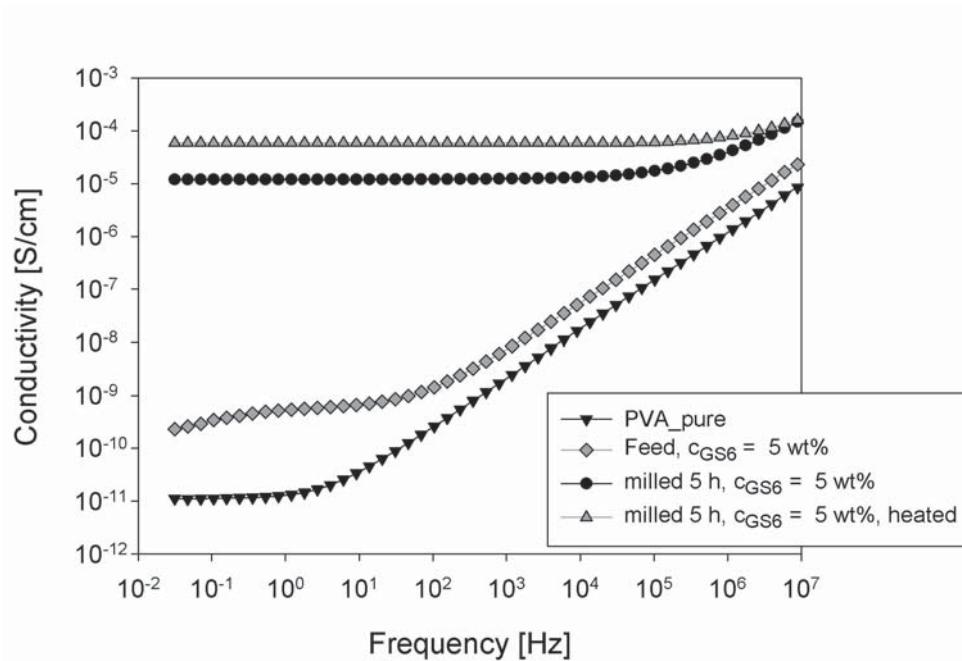
Figure 6.23.: Influence of milling treatment on the conductivity of filled polymers

sistance, which becomes significant at high film resistances. The graphite flakes were produced in a 3 h grinding experiment with 100 μm YSZ beads and a rotational speed of the stirrer of 1000 rpm. After the grinding treatment, the unpeeled particles were removed via centrifugation. As stabilizer, SDS (c = cmc, i.e. $m_{SDS}/m_{graphite}$ = 0.225) and PVA ($m_{PVA}/m_{graphite}$ = 0.098) were used. PVA was proven in preliminary experiments to be a good stabilizer of graphite particles in water.

The surface resistance R_s was calculated from the applied current and the measured voltage using the following equation for a 4-point probe measurement [Smit 58]:

$$R_s = \frac{\pi}{ln2} \cdot \frac{U}{I} \tag{6.7}$$

The conductivity of the film σ can be calculated considering the overall thickness of the film d_{film}:

$$\sigma = \frac{1}{R_s \cdot d_{film}} \tag{6.8}$$

The thicknesses of the films were obtained by cutting the glass substrates and visualizing the cross section in the SEM. In Fig. 6.24, the cross sections

149

of the films produced with the GS6 feed material (left) and a milled sample (right), both stabilized with SDS, are shown.
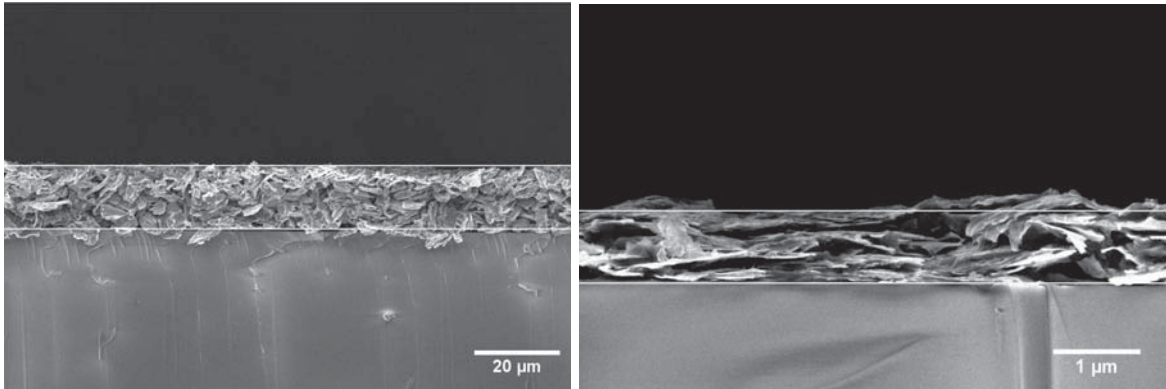
Figure 6.24.: Cross sections of prepared films: GS6 feed materials (left) and milled sample (right)

The differences between the two films are obvious: The feed material consists of thick particles which are randomly distributed on the glass surface leading to a large overall film thickness ($\sim 15\ \mu$m). The film produced from the milled sample yield a much lower thickness (~ 800 nm). The flake-like structure can clearly be seen in the image. Nevertheless, the observed film thickness is still too large to obtain an optical transparency. Hence, other film formation methods such as vacuum filtration should be used in future works instead of the drop-casting route. Using vacuum filtration will also lead to more densely packed films since the formed layers are compressed by additional forces. The polymer as well as the surfactant on the graphite particles are known to affect the conductivity of the films [Yu 07]. Therefore, the coated glass substrates were tempered at 400 °C for 2 hours under atmosphere to remove the major part of the additives. Whereas SDS decomposes at 380 °C, the polymer PVA is not fully removed at 400 °C. Nevertheless a temperature of 400 °C was chosen, because higher temperatures would lead to an oxidation of the graphite flakes. The conductivities and related film thicknesses measured before and after the heat treatment are summarized in Tab. 6.4.

The heat treatment strongly increases the conductivity of the films especially for the milled samples. The highest conductivity of 286 S/cm was

Table 6.4.: Film conductivities before and after heat treatment (400 °C, 2 h)

Sample	Film thickness	Conductivity	Film thickness, heat treated	Conductivity, heat treated
Feed, SDS	14.82 μm	1.69 S/cm	12.88 μm	1.71 S/cm
Feed, PVA	11.54 μm	0.28 S/cm	5.97 μm	3.69 S/cm
3 h, SDS	0.82 μm	8.82 S/cm	0.58 μm	190 S/cm
3 h, PVA	0.97 μm	2.60 S/cm	0.51 μm	286 S/cm

achieved with the PVA stabilized suspension. For the time being, it is unclear how much additive remained in the sample and if further removal, for instance at higher temperatures under inert gas atmosphere, would allow another enhancement in conductivity. The cross sections of the films after tempering are illustrated in Fig. 6.25. It seems that the heat treatment leads to more compact films, which additionally increases the final conductivity. Transparent and highly conductive graphene layers are fabricated in the group of Müllen by an acetylene-assisted thermolysis of GO. Via spin-coating, a sheet thickness of only 3.5 nm with a transmittance of more than 70 % at a wavelength of 500 nm was obtained. The conductivity of the graphene films on quartz substrates of 95 S/cm (after a thermal treatment of 600 °C) could be increased to about 400 S/cm under Ar and to 1425 S/cm under acetylene atmosphere at 1000 °C [Lian 09].
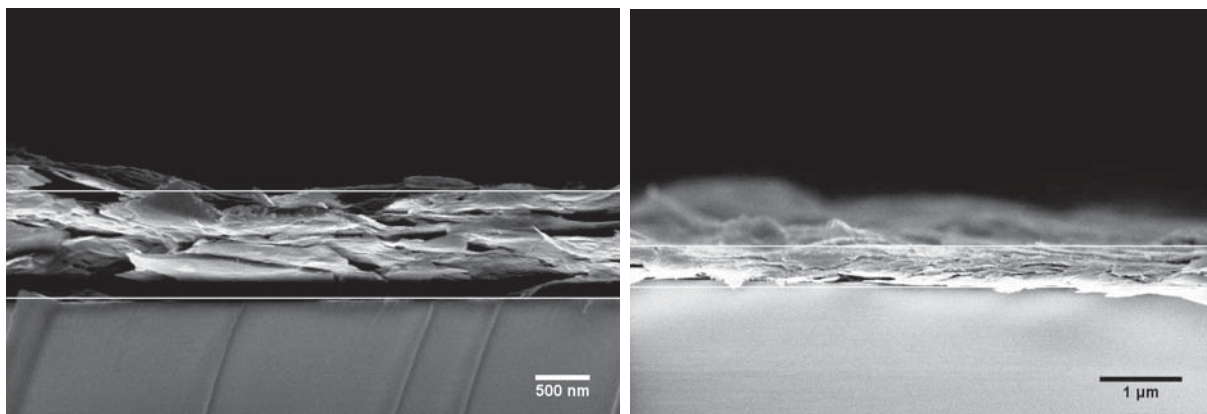

Figure 6.25.: Cross sections of a graphite film prepared from a milled sample stabilized with PVA before (left) and after heat treatment (right)

6.5.3. Coating of delaminated sheets with platinum nanoparticles

Beside its excellent electrical, mechanical, and thermal properties, graphene yields another interesting feature: its ultra-high specific surface area (theoretical value: 2630 m^2/g). Decorating this surface area with noble metal nanoparticles such as Au, Pt, or Pd leads to a new class of composite materials. It is already known from Me-NP-CNT composites, that such new structures exhibit useful properties for catalysts, batteries, sensors, or storage materials [Si 08]. A coating of the produced sheets with Pt-NP can be carried out either by wet impregnation (ion adsorption) or by colloidal deposition. During the impregnation, a precursor (platinum salt) is attached to the graphite surface and afterwards reduced to Pt-NP. The colloidal method includes a separate fabrication of Pt-NP and their adhesion to the graphite surface in a subsequent mixing step. For catalytic applications, which are in the focus of the following investigations, platinum particle sizes in a range between 2 nm and 8 nm are favorable, since they yield a high catalytic activity combined with a high specific surface area. Additionally, the formation of free NP as well as their agglomerates should be avoided for economical reasons.

In Fig. 6.26, TEM images of coated delaminated graphite sheets are illustrated. Supporting information about the detailed coating procedures are provided in the appendix.

The Pt-NP used in the colloidal deposition approach were produced via reduction of hexachloroplatinic acid (H$_2$PtCl$_6$) in an ethanol-water mixture under stirring at 78 °C for 3 h in a reflux apparatus. The nanoparticles have a mean diameter of 3 nm - 4 nm, which could be confirmed by XRD measurements. Although different ratios of the Pt-NP amount to the graphite surface area were tested, the surfaces of the delaminated sheets were not fully covered with platinum nanoparticles. In contrast, using the wet impregnation method, where the attached platinum salt was reduced by ethanol, a homogeneous coverage of the graphite surface with Pt-NP was obtained (right image). However, there could always be some free Pt agglomerates found in the sample.

152
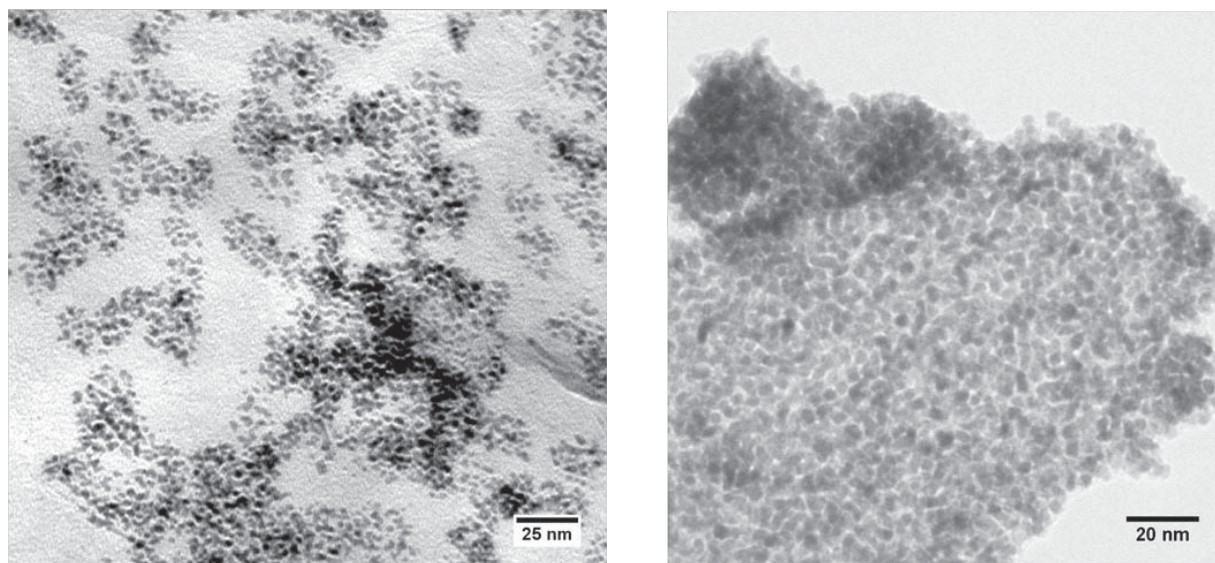
Figure 6.26.: TEM images of Pt-NP coated delaminated graphite sheets from colloidal deposition method (left) and wet impregnation method (right)

Catalytic activity of Pt-NP coated graphite sheets

In a first-principles investigation, the catalytic activity of the Pt-NP coated graphite sheets is examined in the following section. As the catalytic reaction, the reduction from p-nitrophenol to p-aminophenol with $NaBH_4$ and Pt-NP as the heterogeneous catalyzer, was chosen. Sodium borohydrate is used in great excess to ensure that its concentration does not influence the catalytic reaction and therefore a pseudo first order kinetics can be assumed. The reaction can be tracked by means of UV-Vis spectroscopy, since p-nitrophenol has an absorption maximum at 400 nm and p-aminophenol at about 300 nm. The absorption spectra as a function of reaction time are presented in Fig. 6.27. During this reaction, only pure synthesized Pt-NP without any graphite were used as catalyzer.

The absorption maximum of the p-nitrophenol decreases with time, indicating an ongoing reaction until 9 minutes when almost the whole p-nitrophenol is converted. Simultaneously, the adsorption maximum of p-aminophenol increases. The presence of two isosbestic points (encircled) reveals that no secondary reaction takes place. An isosbestic point describes a wavelength at which at least two chemical species (e.g. a reactant and a product) have identical molar adsorption coefficients that remain constant

153
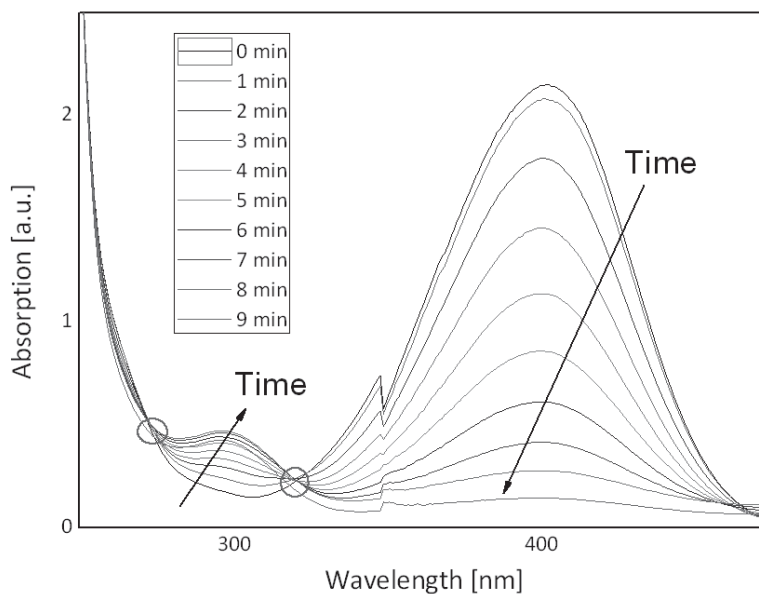
Figure 6.27.: Absorption spectra of p-nitrophenol and p-aminophenol at different reaction times

during a reaction. Stable isosbestic points indicate that a reaction is proceeding without forming intermediate or multiple products.

In Fig. 6.28, the reaction kinetics of the pure Pt-NP and Pt-NP coated graphite sheets (from colloidal deposition method) are compared for different platinum concentrations. The normalized absorption A/A_0 of p-nitrophenol is given as a function of reaction time reduced by a so called induction time for the diffusion of the reactants to the active centers of the catalyst.

154
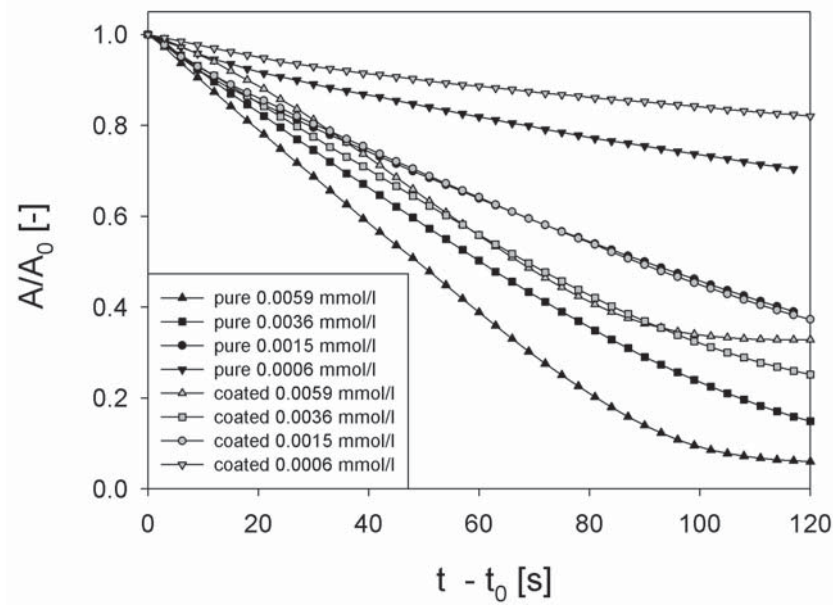
Figure 6.28.: Reaction kinetics of pure Pt-NP and Pt-NP coated delaminated graphite sheets

With increasing Pt concentration, a steeper fall of the normalized absorption curves takes place, indicating a faster conversion of the p-nitrophenol. The pure Pt-NP allow a faster reaction kinetics compared to the platinum particles that are stacked on the graphite surface. The rate constant (here: the apparent rate constant, which is used instead of the true rate constant multiplied with the $NaBH_4$ concentration) of each reaction can be determined from the slopes of the curves, if the ordinate is given in natural logarithmic scale since the following relation apply:

$$A_{400} = A_{400}^0 \cdot e^{-k_{app} \cdot t} \tag{6.9}$$

In Fig. 6.29, the apparent rate constants k_{app} of both systems are given for different Pt concentrations.
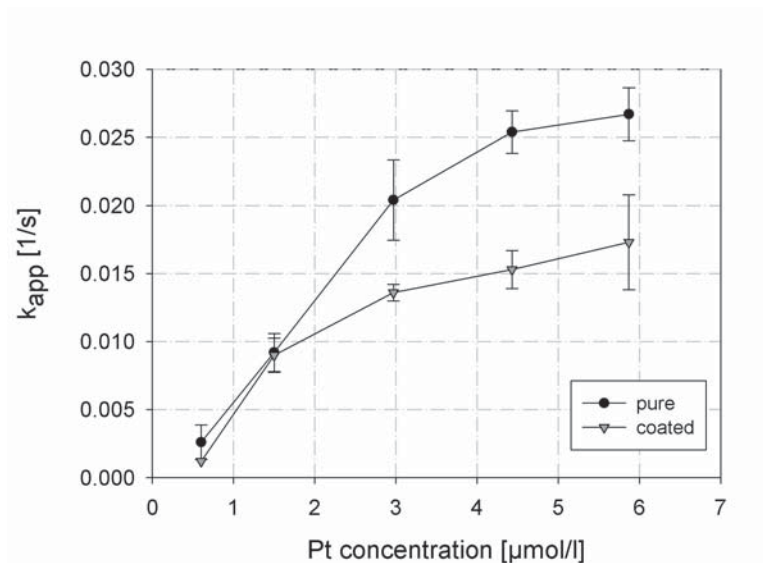
Figure 6.29.: Apparent rate constants k_{app} as a function of Pt concentration for pure Pt-NP and Pt-NP coated delaminated graphite sheets

It can be seen that the apparent rate constants of the pure Pt-NP are larger than those for Pt-NP attached on the graphite sheets. This finding is not astonishing, because the pure Pt-NP, which are not stacked on a carrier material always yield a larger surface area. Nevertheless, catalyst particles are mostly combined with carrier particles in order to avoid a strong agglomeration of the catalyst particles when they are used in dry state and it facilitates their separation from the process if the catalyst material becomes inactive and has to be renewed. However, the above presented results clearly show that the Pt-NP deposited on the surface of delaminated graphite sheets, exhibit a remarkable catalytic activity with rate constants in the same order of magnitude than those achieved by other groups under similar conditions [Ghos 04], [Mei 05].

7. Conclusion and Outlook

Wet grinding in stirred media mills allows the production of nanoparticles by breakage of coarser feed materials. In long-term grinding experiments, a lower grinding limit was found, where no further particle breakage takes place. This true grinding limit has to be distinguished from the apparent grinding limit, which depends on the stabilization of the particles against agglomeration and the flow conditions in the milling chamber. The evolution of the internal microstructure of the particles was shown to play a major role in nanoparticle breakage. Although the particles fall below the brittle-to-ductile transition size, which was regarded as the overall limit of grinding, further size reduction is enabled by a ductile fracture under cyclic loading. Strong plastic deformation is observed even in originally brittle ceramic particles, since the fracture stress exceeds the yield stress below a certain particle size. An accumulation of defects during repeated stressing weakens the material and allows further size reduction as a kind of fatigue fracture. However, below a critical grain size, the defect density declines for the investigated materials. It is likely that dislocations or crystal twins cannot be generated or stored in the smallest grains and therewith the grinding limit is reached, since the transferred energies from the grinding media are no longer sufficient to fracture the particles without available crack nuclei.

Detailed studies were carried out for tin dioxide particles to investigate the influence of process and environmental conditions on the overall limit of grinding. Changing the stress energy, the suspension viscosity and stability, the grinding media material and shape, as well as the process temperature did not show any influence on the grinding limit. In each experiment, a critical size of about 10 nm was reached for the tin dioxide particles. In contrast, the breakage kinetics strongly depend on most of the investigated parameters. In particular, the stress energy highly affects the breakage

157

rates. Hence, huge energy savings are possible by an appropriate adjustment of process parameters. Moreover, a better product quality in terms of a lower amorphous content and less contamination due to grinding media attrition can be achieved.

In addition to tin dioxide, the breakage behavior of several other inorganic materials was investigated. Nearly all of the ground particles yield a grinding limit in the nanometer range which vary with the material system. Since a grinding limit as a result of machine limitation can be excluded and the strong variation in impact intensity did not show a change in the grinding limit, it is likely that the true grinding limit is mainly material dependent. A correlation of the observed limits with distinct material properties was not possible for the time being due to the lack of reliable material data for ceramic nanoparticles. Relevant material information could be provided, for instance, by single particle stressing experiments with a picoindenter inside a transmission electron microscope in future works. With this apparatus, it should be possible on the one hand to determine selected material properties from nanosized particles and in particular from particles coming directly out of the milling process. On the other hand, the response of the particles' microstructure can be followed during and after distinct stressing. New insights in the defect structure can be gained, which might help to understand the fracture process in more detail. Despite single particle investigations, the XRD method can be extended to obtain more information about the microstructure of the whole particle collective. In subsequent works new evaluation methods should be introduced which allow, for instance, the determination of a crystallite size distribution so that a closer look on the internal processes during the milling treatment becomes possible.

In addition to the breakage behavior of brittle materials which mainly show a random size reduction in the comminution process, the breakage behavior of layered materials was studied. Graphite particles were chosen as a model system for the investigations. The strong anisotropy of the bond forces in the graphite crystal result in a selective, orientation depen-

158

dent fragmentation of the particles. As a result, thin graphite flakes with a high aspect ratio are obtained. Since a great interest exists for very thin and concurrently wide sheets, the aim was to realize a controlled selective size reduction by a milling process. Hence, the process parameters were adjusted in a way that the acting forces overcome the attractive van der Waals forces between the sheets without breaking them. Besides the overall inserted energy, the stress intensity plays a major role in the selective breakage mechanism, which can be regarded as a kind of peeling process. Continuous rubbing of the grinding beads over the graphite surface allows the delamination of very thin sheets even down to graphene monolayers. These sheets exhibit aspect ratios up to 500. AFM statistics reveal that 50 % of all delaminated sheets are thinner than 3 nm and about 5 % of them are monolayers.

Finally, some first applications for the delaminated graphene sheets such as their use as filler material in polymers or the production of conductive films were tested and yield promising results. However, the process needs to be optimized in future works. First, to avoid breakage of the flakes it would be helpful to remove already delaminated sheets from the milling process. This could be realized either in a circuit or continuous operation mode coupled with a mechanical separation unit which allows the removal of the thinnest sheets and a backfill of the unpeeled graphite particles. On the one hand this could lead to higher aspect ratios and on the other hand enhance the product quality by lowering the defect density. Secondly, the material system itself can be optimized. Graphite particles with larger domain sizes and a higher purity, especially a lower oxygen content, would lead to a higher product quality. In addition, the stabilizer SDS has to be removed or replaced at least for electronic applications, because it reduces the conductivity of the overall system. However, the presented process is very promising for an industrial application, since it allows a high-yield and low-cost production of graphene monolayers.

Bibliography

[Anti 06]   M. V. Antisari, A. Montone, N. Jovic *et al.* "Low energy pure shear milling: A method for the preparation of graphite nano-sheets". *Scripta Materialia*, 55(11), 1047–50, 2006.

[Arms 09]   P. Armstrong, C. Knieke, M. Mackovic *et al.* "Microstructural evolution during deformation of tin dioxide nanoparticles in a comminution process". *Acta Materialia*, 57(10), 3060–3071, 2009.

[Bala 08]   A. A. Balandin, S. Ghosh, W. Z. Bao *et al.* "Superior thermal conductivity of single-layer graphene". *Nano Lett*, 8(3), 902–7, 2008.

[Balo 10]   R. Balog, B. Jorgensen, L. Nilsson *et al.* "Bandgap opening in graphene induced by patterned hydrogen adsorption". *Nat Mater*, 9(4), 315–9, 2010.

[Balz 05]   D. Balzar, N. C. Popa. "Analyzing microstructure by Reitveld refinement". *The Rigaku Journal*, 22(1), 16–25, 2005.

[Balz 99]   D. Balzar. "Voigt function model in diffraction-line broadening analysis". *(IUCr) Monographs on Crystallography*, 10, 94–126, 1999.

[Bath 99]   C. Bathias. "There is no infinite fatigue life in metallic materials". *Fatigue Fract Eng M*, 22(7), 559–65, 1999.

[Beck 01]   M. Becker, A. Kwade, J. Schwedes. "Stress intensity in stirred media mills and its effect on specific energy requirement". *International Journal of Mineral Processing*, 61(3), 189–208, 2001.

[Berg 04]   C. Berger, Z. Song, T. Li *et al.* "Ultrathin Epitaxial Graphite: 2D Electron Gas Properties and a Route toward Graphene-based Nanoelectronics". *The Journal of Physical Chemistry B*, 108(52), 19912–6, 2004.

[Bilg 06]   E. Bilgili, R. Hamey, B. Scarlett. "Nano-milling of pigment agglomerates using a wet stirred media mill: Elucidation of the kinetics and breakage mechanisms". *Chem Eng Sci*, 61(1), 149–57, 2006.

[Blak 07]   P. Blake, E. W. Hill, A. H. C. Neto *et al.* "Making graphene visible". *Appl Phys Lett*, 91(6), 063124/1–3, 2007.

[Blec 96]   L. Blecher, J. Schwedes. "Energy distribution and particle trajectories in a grinding chamber of a stirred ball mill". *Int J Miner Process*, 44-45, 617–27, 1996.

[Blum 03]   W. Blum. "Werkstoffe und ihre Struktur". *Lecture notes, Department of Materials Science and Engineering*, University Erlangen-Nürnberg, 1–147, 2003.

[Boer 65]   L. B. de Boer, J.H. "Studies on pore systems in catalysts: I-VII". *Journal of Catalysis*, various volumes, 1964/1965.

[Bokh 95]   B. B. Bokhonov, I. G. Konstanchuk, V. V. Boldyrev. "Structural and morphological changes during the mechanical activation of nano-size particles". *Materials Research Bulletin*, 30(10), 1277–84, 1995.

[Bolo 08]   K. I. Bolotin, K. J. Sikes, Z. Jiang *et al.* "Ultrahigh electron mobility in suspended graphene". *Solid State Commun*, 146(9-10), 351–5, 2008.

[Bors 09]   N. K. Borse, M. R. Kamal. "Estimation of Stresses Required for Exfoliation of Clay Particles in Polymer Nanocomposites". *Polymer Engineering and Science*, 49(4), 641–50, 2009.

[Brei 09]   S. Breitung-Faes. "Optimierungspotential bei der Herstellung keramischer Nanopartikeln in Rührwerkskugelmühlen". *PhD thesis*, TU Braunschweig, 2009.

[Canc 11]   L. G. Cancado, A. Jorio, E. H. Martins Ferreira *et al.* "Quantifying defects in graphene via Raman spectroscopy at different excitation energies". *Nano Letters*, 11(8), 3190–3196, 2011.

[Chen 02]   B. Chen, D. Penwell, L. R. Benedetti *et al.* "Particle-size effect on the compressibility of nanocrystalline alumina". *Phys Rev B*, 66(14), 144101/1–4, 2002.

[Chen 09]   B. Chen, H. Zhang, K. A. Dunphy-Guzman *et al.* "Size-dependent elasticity of nanocrystalline titania". *Phys Rev B*, 79, 125406/1–8, 2009.

[Cho 96]   H. Cho, M. A. Waters, R. Hogg. "Investigation of the grind limit in stirred-media milling". *International Journal of Mineral Processing*, 44-45, 607–15, 1996.

[Chri 98]   S. Christiansen, M. Albrecht, H. P. Strunk *et al.* "Microstructure of novel superhard nanocrystalline amorphous composites as analyzed by high resolution transmission electron microscopy". *J Vac Sci Technol B*, 16(1), 19–22, 1998.

[Coir 86]   V. M. Coiro, F. Mazza, G. Pochetti. "Crystal Phases Obtained from Aqueous Solutions of Sodium Dodecyl Sulfate.". *Acta Cryst*, C42, 991–995, 1986.

[Derj 41]   B. V. Derjaguin, L. D. Landau. "Theory of Stability of Highly Charged Lyophobic Sols and Adhesion of Highly Charged Particles in Solutions of Electrolytes". *Acta Physicochim USSR*, 14, 633–52, 1941.

[Dodd 02]   A. C. Dodd, P. G. McCormick. "Synthesis of nanocrystalline ZrO2 powders by mechanochemical reaction of ZrCl4 with LiOH". *Journal of the European Ceramic Society*, 22, 1823–1829, 2002.

[Dryz 94]   J. Dryzmala. "Hydrophobicity and Collectorless Flotation of Inorganic Materials". *Adv Colloid Interfac*, 50(1-3), 143–85, 1994.

[Dugd 60]   C. Dugdale. "Yielding of steel sheets containing slits". *J. Mech. Phys. Solids*, 8, 100–104, 1960.

[Ecke 92]   J. Eckert, J. C. Holzer, C. E. Krill *et al.* "Structural and Thermodynamic Properties of Nanocrystalline Fcc Metals Prepared by Mechanical Attrition". *J Mater Res*, 7(7), 1751–61, 1992.

[Ecke 95]   J. Eckert. "Relationships governing the grain size of nanocrystalline metals and alloys". *Nanostruct Mater*, 6(1-4), 413–6, 1995.

[Engl 09]   J. M. Englert, J. Röhrl, C. D. Schmidt *et al.* "Soluble Graphene: Generation of Aqueous Graphene Solutions Aided by a Perylenebisimide-Based Bolaamphiphile". *Advanced Materials*, 21, 1–5, 2009.

[Evan 84]   A. G. Evans, K. T. Faber. "Crack-Growth Resistance of Microcracking Brittle Materials". *J. Am. Ceram. Soc.*, 67(4), 255–60, 1984.

[Fech 90]   H. J. Fecht, E. Hellstern, Z. Fu *et al.* "Nanocrystalline Metals Prepared by High-Energy Ball Milling". *Metall Trans A*, 21(9), 2333–7, 1990.

[Ferr 06]   A. C. Ferrari, J. C. Meyer, V. Scardaci *et al.* "Raman spectrum of graphene and graphene layers". *Physical Review Letters*, 97(18), 187401/1–4, 2006.

[Fran 98]   C. Frances, C. Laguerie. "Fine wet grinding of an alumina hydrate in a ball mill". *Powder Technol*, 99(2), 147–53, 1998.

[Fu 84]   Y. Fu, A. G. Evans, W. M. Kriven. "Microcrack Nucleation in Ceramics Subject to a Phase-Transformation". *J Am Ceram Soc*, 67(9), 626–30, 1984.

[Garc 02]   F. Garcia, N. Le Bolay, C. Frances. "Changes of surface and volume properties of calcite during a batch wet grinding process". *Chem Eng J*, 85(2-3), 177–87, 2002.

[Geim 07]   A. K. Geim, K. S. Novoselov. "The rise of graphene". *Nature Mater*, 6(3), 183–91, 2007.

[Gerb 06]   W. W. Gerberich, W. M. Mook, M. J. Cordill *et al.* "Nanoprobing fracture length scales". *Int J Fracture*, 138(1-4), 75–100, 2006.

[Ghad 02]   M. Ghadiri, Z. Zhang. "Impact attrition of particulate solids. Part 1: A theoretical model for chipping". *Chem. Eng. Sci.*, 57, 3659–3669, 2002.

[Ghos 04]   S. K. Ghosh, M. Mandal, S. Kundu *et al.* "Bimetallic Pt-Ni nanoparticles can catalyze reduction of aromatic nitro compounds by sodium borohydride in aqueous solution". *Appl Catal a-Gen*, 268(1-2), 61–6, 2004.

[Graf 07]   D. Graf, F. Molitor, K. Ensslin *et al.* "Raman imaging of graphene". *Solid State Commun*, 143(1-2), 44–6, 2007.

[Grif 21]   A. A. Griffith. "The phenomena of rupture and flow in solids". *Phil. Trans. Roy. Soc. (London)*, 221, 163–198, 1921.

[Grya 89]   V. G. Gryaznov, A. M. Kaprelov, A. E. Romanov. "Size effects of dislocation stability in small particles nad microcrystallites". *Scr. Met.*, 23, 1443–8, 1989.

[Grya 91]   V. G. Gryaznov, I. A. Polonsky, A. E. Romanov *et al.* "Size effects of dislocation stability in nanocrystals". *Phys Rev B*, 44(1), p. 42, 1991.

[Haga 79]   J. T. Hagan. "Micromechanics of crack nucleation during indentations". *J Mater Sci*, 14(12), 2975–80, 1979.

[Hall 51]   E. Hall. "The deformation and ageing of mild steel III. Discussion of results". *Proc. Phys. Soc. B*, 64, 747–753, 1951.

[Han 07]   M. Y. Han, B. Ozyilmaz, Y. B. Zhang *et al.* "Energy band-gap engineering of graphene nanoribbons". *Physical Review Letters*, 98(20), 206805/1–4, 2007.

[Haya]   S. Hayashi, S. Ikeda. "Micelle size and shape of sodium dodecyl sulfate in concentrated NaCl solutions". *Journal of Physical Chemistry*, 84.

[Hebe 06]   R. J. Hebert, J. H. Perepezko, H. Rösner *et al.* "Dislocation formation during deformation-induced synthesis of nanocrystals in amorphous and partially crystalline amorphous Al88Y7Fe5 alloy". *Scripta Mater.*, 54, 25–29, 2006.

[Henn 10]   S. L. A. Hennart, W. J. Wildeboer, P. van Hee *et al.* "Stability of particle suspensions after fine grinding". *Powder Technol*, 199(3), 226–31, 2010.

[Hern 08]   Y. Hernandez, V. Nicolosi, M. Lotya *et al.* "High-yield production of graphene by liquid-phase exfoliation of graphite". *Nature Nano*, 3(9), 563–8, 2008.

[Hirt 82]   J. P. Hirth, J. Lothe. "Theory of dislocations". *Book, Wiley, New York*, p. 88, 1982.

164

[Hopp 10]   H. W. Höppel, L. May, M. Prell *et al.* "Influence of grain size and precipitation state on the fatigue lives and deformation mechanisms of CP aluminium and AA6082 in the VHCF-regime". *Intern. J. Fatigue*, 33(1), 10–18, 2010.

[Husb 92]   J. C. Husband, J. M. Adams. "Shear-induced aggregation of carboxylated polymer latices". *Colloid and Polymer Science*, 270(12), 1194–200, 1992.

[Iiji 91]   S. Iijima. "Helical Microtubules of Graphitic Carbon". *Nature*, 354(6348), 56–8, 1991.

[Irwi 57]   G. R. Irwin. "Analysis of Stresses and Strains Near the End of a Crack Traversing a Plate". *J. Appl. Mech.*, 24, 361–4, 1957.

[Ishi 07]   M. Ishigami, J. H. Chen, W. G. Cullen *et al.* "Atomic structure of graphene on SiO2". *Nano Lett*, 7(6), 1643–8, 2007.

[Jano 02]   R. Janot, D. Guerard. "Ball-milling: the behavior of graphite as a function of the dispersal media". *Carbon*, 40(15), 2887–96, 2002.

[Jimb 92]   G. Jimbo. "Chemical engineering analysis of fine grinding phenomenon and process". *Journal of Chemical Engineering of Japan*, 25(2), 117–27, 1992.

[Kara 03]   G. R. Karagedov, N. Z. Lyakhov. "Mechanochemical Grinding of Inorganic Oxides". *Kona*, 21, 76–87, 2003.

[Kend 78]   K. Kendall. "The impossibility of comminuting small particles by compression". *Nature*, 272, 710–1, 1978.

[Kili 02]   C. Kilic, A. Zunger. "Origins of coexistence of conductivity and transparency in SnO2". *Physical Review Letters*, 88(9), 095501/1–4, 2002.

[Kim 09]   K. S. Kim, Y. Zhao, H. Jang *et al.* "Large-scale pattern growth of graphene films for stretchable transparent electrodes". *Nature*, 457(7230), 706–10, 2009.

[Kneh 82]   R. Knehans, R. Steinbrech. "Memory effect of crack resistance during slow crack growth in notched Al203 bend specimens". *J. Mater. Sci. Lett.*, 1, 327–29, 1982.

[Knie 09]   C. Knieke, M. Sommer, W. Peukert. "Identifying the apparent and true grinding limit". *Powder Technology*, 195(1), 25–30, 2009.

[Knie 10a]   C. Knieke, A. Berger, J. Röhrl *et al.* "Scalable production of graphene sheets by mechanical delamination". *Carbon*, 48(11), 3196–3204, 2010.

[Knie 10b]   C. Knieke, C. Steinborn, S. Romeis *et al.* "Nanoparticle production with stirred media mills: opportunities and limits". *Chem. Eng. Technol.*, 33(9), 1401–1411, 2010.

[Knie 11a]   C. Knieke, S. Romeis, W. Peukert. "Influence of process parameters on breakage kinetics and grinding limit at the nanoscale". *AIChE Journal*, 57(7), 1751–1758, 2011.

[Knie 11b]   C. Knieke, P. Vozdecky, A. Roosen *et al.* "Verfahrenstechnische Fortschritte für die Herstellung neuer Materialien - Foliengießen aus Nanopartikeln". *Chemie Ingenieur Technik*, 83(4), 535–544, 2011.

[Koch 97]   C. C. Koch. "Synthesis of nanostructured materials by mechanical milling: Problems and opportunities". *Nanostruct Mater*, 9(1-8), 13–22, 1997.

[Kwad 02]   A. Kwade, J. Schwedes. "Breaking characteristics of different materials and their effect on stress intensity and stress number in stirred media mills". *Powder Technol*, 122(2-3), 109–21, 2002.

[Kwad 96]   A. Kwade. "Autogenzerkleinerung von Kalkstein in Rührwerkskugelmühlen". *PhD thesis*, TU Braunschweig, 1996.

[Kwad 99]   A. Kwade. "Determination of the most important grinding mechanism in stirred media mills by calculating stress intensity and stress number". *Powder Technol*, 105(1-3), 382–8, 1999.

[Kwan 04]   C. C. Kwan, Y. Q. Chena, Y. L. Ding *et al.* "Development of a novel approach towards predicting the milling behaviour of pharmaceutical powders". *Eur J Pharm Sci*, 23(4-5), 327–36, 2004.

[Laga 97]   G. Lagaly, O. Schulz, R. Zimehl. "Dispersionen und Emulsionen". *Book, Steinkopff Verlag*, Darmstadt, Germany, 1997.

[Lata 03]   A. Latapie, D. Farkas. "Effect of grain size on the elastic properties of nanocrystalline alpha-iron". *Scripta Materialia*, 48(5), 611–5, 2003.

[Lee 08]   C. Lee, X. D. Wei, J. W. Kysar *et al.* "Measurement of the elastic properties and intrinsic strength of monolayer graphene". *Science*, 321(5887), 385–8, 2008.

[Lian 09]   Y. Y. Liang, J. Frisch, L. J. Zhi *et al.* "Transparent, highly conductive graphene electrodes from acetylene-assisted thermolysis of graphite oxide sheets and nanographene molecules". *Nanotechnology*, 20(43), 434007/1–6, 2009.

[Loty 09]   M. Lotya, Y. Hernandez, P. J. King *et al.* "Liquid Phase Production of Graphene by Exfoliation of Graphite in Surfactant/Water Solutions". *Journal of the American Chemical Society*, 131(10), 3611–20, 2009.

[Mak 08]   K. F. Mak, M. Y. Sfeir, Y. Wu *et al.* "Measurement of the Optical Conductivity of Graphene". *Physical Review Letters*, 101(19), 196405/1–4, 2008.

[Mart 81]   G. Martinez, J. Morales, G. Munuera. "Grinding-Induced Structural Transformations in CaCO3". *J Colloid Interf Sci*, 81(2), 500–10, 1981.

[McAl 07]   M. J. McAllister, J. Li, D. H. Adamson *et al.* "Single Sheet Functionalized Graphene by Oxidation and Thermal Expansion of Graphite". *Chemistry of Materials*, 19(18), 4396–404, 2007.

[Mei 05]   Y. Mei, G. Sharma, Y. Lu *et al.* "High catalytic activity of platinum nanoparticles immobilized on spherical polyelectrolyte brushes". *Langmuir*, 21(26), 12229–34, 2005.

[Meie 09]   M. Meier, E. John, D. Wieckhusen *et al.* "Influence of mechanical properties on impact fracture: Prediction of the milling behaviour of pharmaceutical powders by nanoindentation". *Powder Technology*, 188(3), 301–313, 2009.

[Mend 03]   S. Mende, F. Stenger, W. Peukert *et al.* "Mechanical production and stabilization of submicron particles in stirred media mills". *Powder Technol*, 132(1), 64–73, 2003.

[Mend 04a]   G. Mende, S. Bernotat, J. Schwedes. "Displacement flow and particle displacement between milling balls resp milling ball and wall". *Chemie Ingenieur Technik*, 76(1-2), 77–80, 2004.

[Mend 04b]   S. Mende. "Mechanische Erzeugung von Nanopartikeln in Rührwerkskugelmühlen". *PhD thesis*, TU Braunschweig, 2004.

[Meye 06]   M. A. Meyers, A. Mishra, D. J. Benson. "Mechanical properties of nanocrystalline materials". *Prog Mater Sci*, 51(4), 427–556, 2006.

[Meye 07]   J. C. Meyer, A. K. Geim, M. I. Katsnelson *et al.* "The structure of suspended graphene sheets". *Nature*, 446(7131), 60–3, 2007.

[Mile 08]   A. Milev, M. Wilson, G. S. K. Kannangara *et al.* "X-ray diffraction line profile analysis of nanocrystalline graphite". *Materials Chemistry and Physics*, 111(2-3), 346–50, 2008.

[Mook 07]   W. M. Mook, J. D. Nowak, C. R. Perrey *et al.* "Compressive stress effects on nanoparticle modulus and fracture". *Phys Rev B*, 75(21), 2007.

[Nair 08]   R. R. Nair, P. Blake, A. N. Grigorenko *et al.* "Fine structure constant defines visual transparency of graphene". *Science*, 320(5881), p. 1308, 2008.

[Nieh 91]   T. G. Nieh, J. Wadsworth. "Hall-Petch Relation in Nanocrystalline Solids". *Scripta Metall Mater*, 25(4), 955–8, 1991.

[Ning 97]   Z. Ning, R. Boerefijn, M. Ghadiri *et al.* "Distinct element simulation of impact breakage of lactose agglomerates". *Advanced Powder Technology*, 8(1), 15–37, 1997.

[Novo 04]   K. S. Novoselov, A. K. Geim, S. V. Morozov *et al.* "Electric field effect in atomically thin carbon films". *Science*, 306(5296), 666–9, 2004.

[Ogur 97]   K. Ogura, T. Saino, M. Nakayama *et al.* "The humidity dependence of the electrical conductivity of a soluble polyaniline-poly(vinyl alcohol) composite film". *J. Mater. Chem.*, 7(12), 2363–66, 1997.

[Orow 49]   E. Orowan. "Fracture and strength of solids". *Rep. Prog. Phys.*, 12, 185–232, 1949.

[Ostl 09]   F. Ostlund, K. Rzepiejewska-Malyska, K. Leifer *et al.* "Brittle-to-Ductile Transition in Uniaxial Compression of Silicon Pillars at Room Temperature". *Adv Funct Mater*, 19(15), 2439–44, 2009.

[Pan 97]   X. Pan, J. G. Zheng. "Microstructure of and crystal defects in the nanocrystalline tin dioxide films". *Mat. Res. Soc. Symp. Proc.*, 472, 87–92, 1997.

[Park 09]   S. Park, R. S. Ruoff. "Chemical methods for the production of graphenes". *Nature Nano*, 4(4), 217–24, 2009.

[Penn 98]   R. L. Penn, J. F. Banfield. "Imperfect oriented attachment: Dislocation generation in defect-free nanocrystals". *Science*, 281(5379), 969–71, 1998.

[Pese 08]   H. Pesenti, M. Leoni, P. Scardi. "XRD line profile analysis of calcite powders produced by high energy milling". *Z Kristallogr*, 143–50, 2008.

[Petc 53]   N. Petch. *J. Iron Steel Inst.*, 173, 25–28, 1953.

[Peuk 04]   W. Peukert. "Material properties in fine grinding". *Int. J. Miner. Process.*, 74, 3–17, 2004.

[Pezz 98]   G. Pezzotti, K. Ota. "Internal friction of ceramic single crystals at very high temperature". *Phys Rev B*, 58(18), 11880–9, 1998.

[Polo 91]   I. A. Polonsky, A. E. Romanov, V. G. Gryaznov *et al.* "Screw dislocation in spherical particle". *Czech. J. Phyz*, 41(12), 1249–55, 1991.

[Pour 07]   P. Pourghahramani, E. Forssberg. "Changes in the structure of hematite by extended dry grinding in relation to imposed stress energy". *Powder Technol*, 178(1), 30–9, 2007.

[Pour 08]   P. Pourghahramani, E. Altin, M. R. Mallembakam *et al.* "Microstructural characterization of hematite during wet and dry millings using Rietveld and XRD line profile analyses". *Powder Technol*, 186(1), 9–21, 2008.

[Rehb 72]   P. A. Rehbinder, E. D. Shchukin. "Surface phenomena in solids during deformation and fracture processes". *in S.G. Davison (ed.), Progress in Surface Science*, 3, 97–188, 1972.

168

[Rein 09]   A. Reina, X. T. Jia, J. Ho *et al.* "Large Area, Few-Layer Graphene Films on Arbitrary Substrates by Chemical Vapor Deposition". *Nano Lett*, 9(1), 30–5, 2009.

[Riet 69]   H. M. Rietveld. "A profile refinement method for nuclear and magnetic structures". *J. Appl. Cryst.*, 2, 65–71, 1969.

[Roes 06]   J. Roesler, H. Harders, M. Bäker. "Mechanisches Verhalten der Werkstoffe". *Book*, Teubner Verlag, 2nd Edition, 2006.

[Roma 95]   A. E. Romanov. "Continuum theory of defects in nanoscaled materials". *Nanostruct Mater*, 6(1-4), 125–34, 1995.

[Rose 04]   M. J. Rosen. "Surfactants and Interfacial Phenomena". *Book*, Hoboken, New Jersey: John Wiley Sons, p. 3rd Edition, 2004.

[Rump 90]   H. Rumpf. "Particle Technology". *Chapman and Hall*, Book, London, UK, 1990.

[Sand 03]   J. K. W. Sandler, J. E. Kirk, I. A. Kinloch *et al.* "Ultra-low electrical percolation threshold in carbon-nanotube-epoxy composites". *Polymer*, 44(19), 5893–9, 2003.

[Sche 18]   P. Scherrer. "Estimation of the size and internal structure of colloidal particles by means of Roentgen rays.". *Nachr. Ges. Wiss. Göttingen*, 96–100, 1918.

[Schm 11]   C. W. Schmidt, C. Knieke, V. Maier *et al.* "Accelerated grain refinement during accumulative roll bonding by nanoparticle reinforcement". *Scripta Mater.*, 64(3), 245–248, 2011.

[Schn 06]   H. C. Schniepp, J. Li, M. J. McAllister *et al.* "Functionalized Single Graphene Sheets Derived from Splitting Graphite Oxide". *The Journal of Physical Chemistry B*, 110(17), 8535–9, 2006.

[Scho 71]   K. Schönert, K. Steier. "Die Grenze der Zerkleinerung bei kleinen Korngrößen". *Chem Ing Tech*, 43(13), 773–7, 1971.

[Scho 88]   K. Schönert, S. Bernotat. "Size Reduction". *Ullmann's Encyclopedia of Industrial Chemistry*, Wiley-VCH, Weinheim, 1988.

[Schu 93]   W. Schütz. "Zur Geschichte der Schwingfestigkeit". *Materialwissenschaft und Werkstofftechnik*, 24, 203–232, 1993.

[Shar 07]   M. A. Sharif, H. Sueyoshi. "Microstructure and Properties of Porous CMCs Prepared by HIPing the Pyrolyzed ZrO2/Si/Phenol Resin Composite". *Materials Science Forum*, 561-565, 747–750, 2007.

[Si 08]   Y. C. Si, E. T. Samulski. "Exfoliated Graphene separated by Platinum Nanoparticles". *Chem Mater*, 20(21), 6792–7, 2008.

[Smit 58]   F. M. Smits. "Measurement of Sheet Resistivities with the Four-Point Probe". *The Bell System Technical Journal*, 1958.

[Somm 07]   M. Sommer. "Mechanical production of nanoparticles in stirred media mills". *PhD thesis*, University Erlangen-Nürnberg, 2007.

[Stan 06a]   S. Stankovich, D. A. Dikin, G. H. B. Dommett *et al.* "Graphene-based composite materials". *Nature*, 442(7100), 282–6, 2006.

[Stan 06b]   S. Stankovich, R. D. Piner, S. T. Nguyen *et al.* "Synthesis and exfoliation of isocyanate-treated graphene oxide nanoplatelets". *Carbon*, 44(15), 3342–7, 2006.

[Stan 07]   S. Stankovich, D. A. Dikin, R. D. Piner *et al.* "Synthesis of graphene-based nanosheets via chemical reduction of exfoliated graphite oxide". *Carbon*, 45(7), 1558–65, 2007.

[Steh 06]   N. Stehr, A. Kwade, H. Weit *et al.* "Hochschulkurs - Zerkleinern und Dispergieren mit Rührwerkskugelmühlen". *Kapitel: Maßstabsübertragung*, 2006.

[Steh 82]   N. Stehr. "Zerkleinerung und Materialtransport in einer Rührwerkskugelmühle". *PhD thesis*, TU Braunschweig, 1982.

[Sten 02]   H. H. Stender. "Einfluß von Größe und Bauart auf die Zerkleinerung in Rührwerkskugelmühlen". *PhD thesis*, TU Braunschweig, 2002.

[Sten 03]   F. Stenger, W. Peukert. "The role of particle interactions on suspension rheology - Application to submicron grinding in stirred ball mills". *Chem Eng Technol*, 26(2), 177–83, 2003.

[Sten 05a]   F. Stenger. "Grenzflächeneffekte bei der Nanozerkleinerung in Rührwerkskugelmühlen". *PhD thesis*, University Erlangen-Nürnberg, 2005.

[Sten 05b]   F. Stenger, S. Mende, J. Schwedes *et al.* "The influence of suspension properties on the grinding behavior of alumina particles in the submicron size range in stirred media mills". *Powder Technol*, 156(2-3), 103–10, 2005.

[Sten 05c]   F. Stenger, S. Mende, J. Schwedes *et al.* "Nanomilling in stirred media mills". *Chemical Engineering Science*, 60(16), 4557–65, 2005.

[Stok 44]   A. R. Stokes, A. J. C. Wilson. "The diffraction of X rays by distorted crystal aggregates - I". *Proc. Phys. Soc. (Lond.)*, 56, 174–181, 1944.

[Stol 08]   M. D. Stoller, S. J. Park, Y. W. Zhu *et al.* "Graphene-Based Ultracapacitors". *Nano Lett*, 8(10), 3498–502, 2008.

[Sun 03]   S. H. Sun, G. W. Meng, G. X. Zhang *et al.* "Raman scattering study of rutile SnO2 nanobelts synthesized by thermal evaporation of Sn powders". *Chem Phys Lett*, 376(1-2), 103–7, 2003.

[Sun 10]   Z. Sun, A. R. Barron. "TEM Imaging of Carbon Nanomaterials". *Scientific-Commons*, http://cnx.org/content/m22963/latest/, 2010.

[Sund 04]   J. Sundqvist, M. Ottosson, A. Harsta. "CVD of epitaxial SnO2 films by the SnI4/O-2 precursor combination". *Chem Vapor Depos*, 10(2), 77–82, 2004.

[Tabo 70]   D. Tabor. "The hardness of solids". *Rev. Phys. Technol.*, 1, 145–55, 1970.

[Tadm 01]   R. Tadmor. "The London-van der Waals interaction energy between objects of various geometries". *J Phys-Condens Mat*, 13(9), 195–202, 2001.

[Theu 99]   J. Theuerkauf, J. Schwedes. "Theoretical and experimental investigation on particle and fluid motion in stirred media mills". *Powder Technol*, 105(1-3), 406–12, 1999.

[Thom 87]   P. Thompson, D. E. Cox, J. B. Hastings. "Rietveld refinement of Debye-Scherrer synchrotron X-ray data from Al2O3". *J. Appl. Cryst.*, 20, 79–83, 1987.

[Ting 08]   C. H. Ting, C. Y. Tan, S. Ramesh *et al.* "Sintering Behaviour of TiO2 Doped Alumina for Biomedical Application". *Biomed 2008, IFMBE Proceedings*, 21(3,6), 351–353, 2008.

[Tsuz 04]   T. Tsuzuki, P. G. McCormick. "Mechanochemical synthesis of nanoparticles". *Journal of Materials Science*, 39, 5143–5146, 2004.

[Vale 07]   P. Valentini, W. W. Gerberich, T. Dumitrica. "Phase-transition plasticity response in uniaxially compressed silicon nanospheres". *Physical Review Letters*, 99(17), 175701/1–4, 2007.

[Vepr 95]   S. Veprek, S. Reiprich. "A concept for the design of novel superhard coatings". *Thin Solid Films*, 268(1-2), 64–71, 1995.

[Verw 48]   E. J. W. Verwey, J. T. G. Oberbeek. "Theory of stability of lyophobic colloids". *Elsevier*, Amsterdam, 1948.

[Vita 08]   A. Vital, S. Zurcher, R. Dittmann *et al.* "Ultrafine comminution of dental glass in a stirred media mill". *Chem Eng Sci*, 63(2), 484–94, 2008.

[Voge 03]   L. Vogel. "Zur Bruchwahrscheinlichkeit prallbeanspruchter Partikeln". *PhD thesis*, TU München, 2003.

[Vozd 10]   P. Vozdecky, C. Knieke, W. Peukert *et al.* "Direct tape casting of nano-sized Al2O3 slurries derived from autogenous nano-milling". *J. Amer. Ceram. Soc.*, 93(5), 1313–1319, 2010.

[Walk 37]   W. H. Walker, W. K. Lewis, W. H. McAdams *et al.* "Principles of Chemical Engineering". *McGraw-Hill, New York*, p. 255, 1937.

[Wang 04]   X. T. Wang, N. P. Padture. "Shear strength of ceramics". *J Mater Sci*, 39(5), 1891–3, 2004.

[Wang 06]   Y. M. Wang, E. Forssberg. "Production of carbonate and silica nano-particles in stirred bead milling". *Int J Miner Process*, 81(1), 1–14, 2006.

[Wang 07]   X. Wang, L. Zhi, K. Müllen. "Transparent, Conductive Graphene Electrodes for Dye-Sensitized Solar Cells". *Nano Lett*, 8(1), 323–7, 2007.

[Wanl 96]   E. J. Wanless, W. A. Ducker. "Organization of sodium dodecyl sulfate at the graphite-solution interface". *Journal of Physical Chemistry*, 100(8), 3207–14, 1996.

[Weit 86]   H. Weit, J. Schwedes. "Maßstabsvergrößerung von Rührwerkskugelmühlen". *Chemie Ingenieur Technik*, 58(10), 818–19, 1986.

[Wu 02]   J. Wu, N. P. Padture, P. G. Klemens *et al.* "Thermal conductivity of ceramics in the ZrO2-GdO1.5 system". *J Mater Res*, 17(12), 3193–200, 2002.

[Xie 08]   S. H. Xie, Y. Y. Liu, J. Y. Li. "Comparison of the effective conductivity between composites reinforced by graphene nanosheets and carbon nanotubes". *Appl Phys Lett*, 92(24), 243121/1–3, 2008.

[Yu 07]   J. R. Yu, K. B. Lu, E. Sourty *et al.* "Characterization of conductive multi-wall carbon nanotube/polystyrene composites prepared by latex technology". *Carbon*, 45(15), 2897–903, 2007.

[Yu 10]   Q. Yu, Z. W. Shan, J. Li *et al.* "Strong crystal size effect on deformation twinning". *Nature*, 463(7279), 335–8, 2010.

[Zett 68]   A. C. Zettlemoyer. "Hydrophobic surfaces". *J Colloid Interf Sci*, 28(3-4), 343–69, 1968.

[Zhan 05]   Y. B. Zhang, Y. W. Tan, H. L. Stormer *et al.* "Experimental observation of the quantum Hall effect and Berry's phase in graphene". *Nature*, 438(7065), 201–4, 2005.

172

A. Appendix

A.1. Reproducibility of grinding experiments

The reproducibility of experimental data is an important factor for reliable results. Since the grinding experiments and their evaluation require a great expenditure of work, it is not possible to repeat every single experiment. Nonetheless, some selected experiments were repeated in order to examen their reproducibility. In Fig. A.1, the particle and crystallite size evolution is given for three different experiments that were carried out under the same grinding conditions.
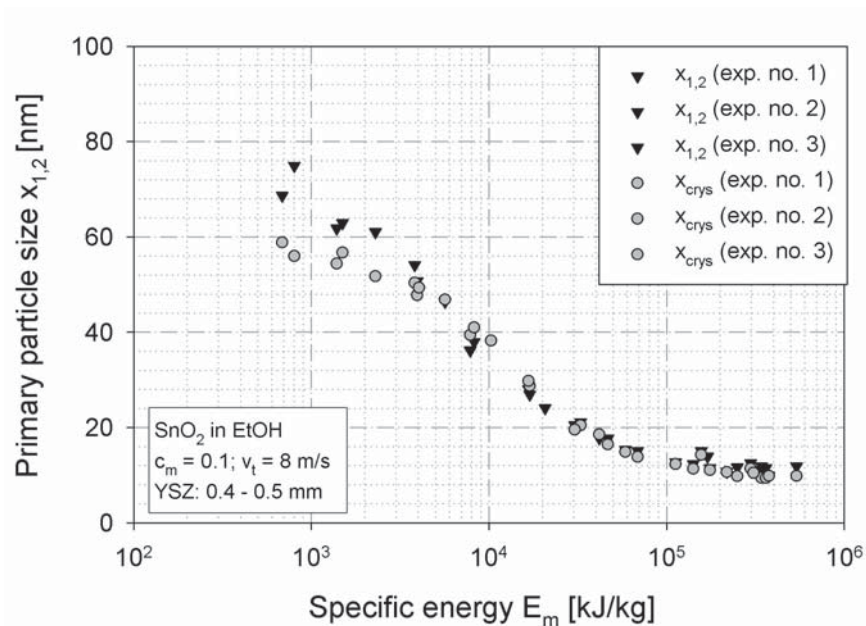

Figure A.1.: Reproducibility of grinding experiments: SnO_2 milled in ethanol

In general, both the primary particle sizes as well as the crystallite sizes could be well reproduced in the experiments. The largest deviations exist at the beginning of the experiments since the manual filling procedure

varies slightly in each experiment and the used measuring instruments yield larger standard deviations for larger particle sizes. In addition to the reproducibility of the grinding experiments, the reproducibility of the measuring data is of great importance for a correct interpretation of the obtained results. The reproducibility of the measured data depends on the one hand on the standard deviations of the instrument and on the other hand on variations during sample preparation. The error bars in the given diagrams of this work represent the standard deviations of the related instrument as a function of the measuring variable, for instance the particle size. Since BET was the most frequently used analysis method of this work, deviations of the measured results are presented as a function of several preparative factors. In Fig. A.2, the influence of heating time and temperature on the mass specific surface area S_m during the degassing under vacuum of a milled powder is presented.
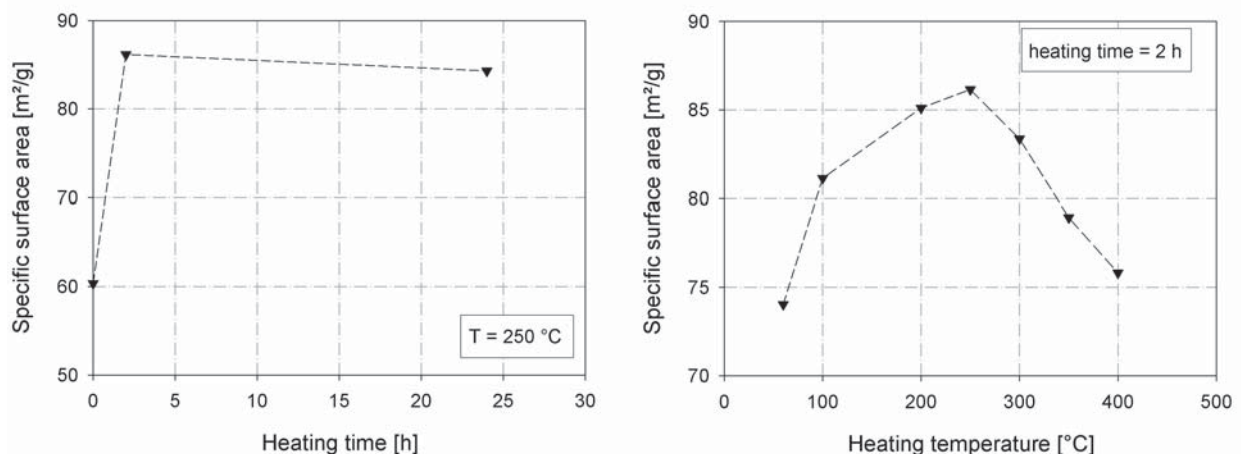

Figure A.2.: Influence of sample preparation on the BET surface area: influence of heating time (left) and temperature (right)

It is obvious that the degassing conditions have a strong influence on the final surface area. If the heating time is too short, not all solvent molecules are removed from the particles' surface and smaller S_m values are obtained. The same happens if the heating temperature is too low. In contrast, at too large temperatures ($> 250\,°C$ at 2 h heating time) the surface area starts to decrease caused by a beginning densification and possible formation of solid

174

bridges. A maximum mistake of about 14 % is possible by choosing wrong heating conditions in the analyzed range. Hence, it is very important to work out the optimal preparation conditions for each material system. The results of another sample, which was measured three times under the same heating specifications, are given in Fig. A.3. Deviations of less than 2 % are observed for high surface areas. Also, other preparative factors such as the pestling time (0 min to 60 min) of the samples before the measurements as well as the degree of cell filling were investigated. In both cases it could be shown that the variations are smaller than the standard deviation of the instrument.
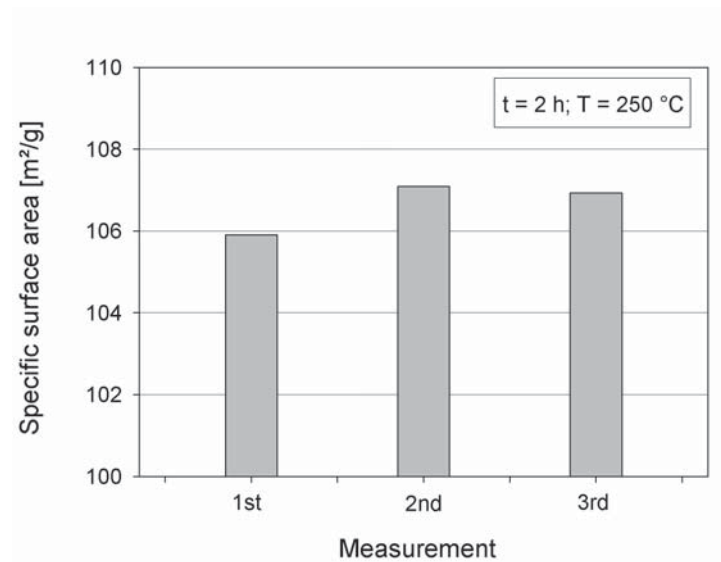

Figure A.3.: Deviations of the surface area from BET measurements

A.2. Comparison between Rietveld and Scherrer evaluation

In this work, two evaluation methods for the X-ray diffraction pattern were employed: the Scherrer equation and the Rietveld refinement. Both methods provide information about a volume-weighted crystallite size. In the following, the theoretical background of the Rietveld method is described.

The Rietveld refinement

The Rietveld refinement is a technique which was published by Hugo Rietveld in the late 1960's and allows the characterization of crystalline materials by means of X-ray or neutron radiation [Riet 69].
The X-ray pattern of a crystalline powder contains material information as well as information about the inner structure, e.g. the size of the coherent scattering domains (which is usually termed as crystallite size) and the mircostrain resulting from defects in the material. Both effects cause a broadening of the diffraction peaks, but show a different Bragg angle dependency, which allows a seperate evaluation of crystallite size and strain. During a Rietveld refinement, a theoretical line profile is generated from materials' structure data. It was shown that the line profile can be fitted by some combination of Gauss and Lorentz functions such as a Voigt function (convolution of Gauss and Lorentz functions), pseudo-Voigt (weighted sum of both), or Pearson VII function (Lorentz function with a variable exponent) [Balz 05]. The most widely used model in Rietveld refinements is the pseudo-Voigt function, which is also used in this work. The theoretical pattern is refined by a least square approach until it matches the measured profile. Finally, for each portion, e.g. Lorentzian and Gaussian, the full width at half maximum Γ as a function of the Bragg angle Θ is obtained. Using the pseudo-Voigt model from Thompson, Cox, and Hastings [Thom 87] gives the following dependencies:

$$\Gamma_G^2 = U tan^2\Theta + V tan\Theta + W + P/cos^2\Theta \tag{A.1}$$

176

$$\Gamma_L = X/cos\Theta + Y tan\Theta \tag{A.2}$$

where G and L are related to Gauss and Lorentz profiles, respectively. The other parameters U, V, W, X, Y, and P are fit parameters containing information about crystallite size and strain. After subtraction of the instrumental line broadening from the fitted profile, size information can be gained from the parameters X and P (cosine terms), whereas strain information are obtained from U and Y values (tangent terms). The evaluation of the crystallite size is based on the well-known Scherrer equation (see Eq. 4.3) and the microstrain is determined with the approach of Stokes and Wilson [Stok 44]. The maximum (upper limit) strain ϵ_0 is defined as

$$\epsilon_0 = \frac{\Delta d}{d} = \frac{\beta_D(2\Theta)}{4 tan\Theta} \tag{A.3}$$

where Δd is the change of the lattice parameter d caused by the presence of defects and β_D is the portion of the integral breadth of a diffraction peak, which is related to lattice distortion [Balz 99]. β_D can be obtained from the refined U (for Lorentz profile) and Y (for Gauss profile) values after conversion of the FWHM values to intergral breadth values.

To achieve reliable size and strain information, a good fit is the most important requirement in a Rietveld refinement. A measure for the quality of the fit is the GOF (= goodness of fit) value and the R_{wp} (= weighted residual error) value. Furthermore, high quality diffraction patterns are necessary to allow correct evaluations.

Comparison of Rietveld and Scherrer results

In contrast to the Rietveld refinement, the Scherrer approach does not consider a microstrain inside the lattice and relates the whole peak broadening to the crystallite size. Hence, the sizes obtained from the Scherrer equation are underestimated for strained particles. In Fig. A.4, the crystallite sizes

of a grinding experiment evaluated with both methods are compared. In addition, the influence of the instrumental line broadening is investigated. Therefore, the X-ray pattern of a LaB_6 NIST standard was measured and the instrumental FWHM values were detected as a function of diffraction angle (Caglioti function). The consideration of the instrumental broadening is important especially for larger grain sizes where the size broadening is in the same order of magnitude as the instrumental broadening. The Rietveld evaluation with the software TOPAS automatically subtract the instrumental broadening, which is calculated from given instrumental parameters.
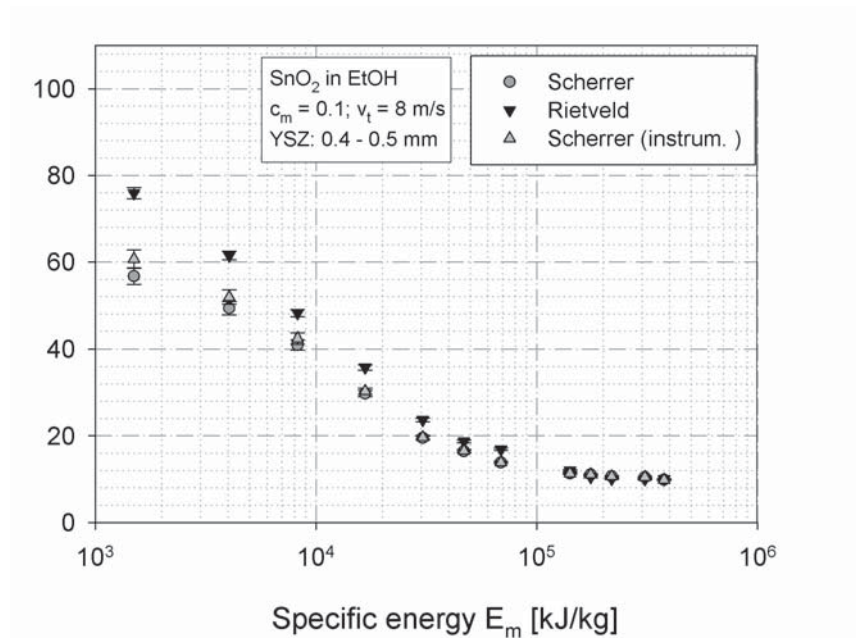

Figure A.4.: Comparison between Rietveld and Scherrer evaluation

As expected, the crystallite sizes obtained from the Scherrer equation are a little smaller than the sizes from the Rietveld refinement especially for larger sizes where differences in the broadening have a stronger impact on the grain size and an evaluation becomes more imprecise. The instrumental broadening has only a slight influence for larger grain sizes (> 50 nm). It has to be taken into account that the elimination of the instrumental profile requires a deconvolution of the measured profile into its single components.

178

A.3. Micropore analysis of various materials

The primary particle sizes presented in this work were calculated from the measured mass specific surface areas. The BET measurements were carried out as 7-point measurements, where the adsorbed nitrogen volume is detected at seven different relative pressures p/p_0. Thereby, it is of great importance to exclude the presence of micropores inside the particles, which can enhance the measured surface areas and falsify the calculated primary particle sizes. One method for the detection of micropores is the V-t-plot according to de Boer [Boer 65], where the adsorption isotherm is measured at low relative pressures. The volume of the adsorbed gas V is plotted versus the thickness of the adsorbed film t. The statistical thickness t can be calculated from the relative pressures p/p_0 using Eq. A.4 [see Nova Operation Manual, Quantachrome, 2008].

$$t(\mathring{A}) = 0.88 \left(\frac{p}{p_0}\right)^2 + 6.45 \left(\frac{p}{p_0}\right) + 2.98 \tag{A.4}$$

The V-t-plot gives a straight line for non-porous materials, which passes through the origin. The total surface area S_t can be calculated from the slope of the V-t-plot using the derived equation from de Boer (Eq. A.5). The total surface area equals the obtained mesopore surface area from the BET method (7- or 4-point measurement) S_m, if no micopores exist in the sample. Otherwise the total surface area consists of both, a micro- and mesopore portion (see Eq. A.6). For the determination of the Sauter diameter, only the mesopore surface area from the BET approach can be used.

$$S_t = \frac{15.47 \cdot V}{t(\mathring{A})} \tag{A.5}$$

$$S_t = S_{MP} + S_m \tag{A.6}$$

In Fig. A.5, a typical V-t-plot of a microporous milled alumina sample is given [Somm 07]. Two distinct slopes can be detected. At low relative pressures (small de Boer film thicknesses), a steeper gradient is observed since a larger effective surface area is available for adsorption. When the micropores are filled with gas at higher relative pressures, the slope flattens

179

and reflects the mesopore adsorption. From this part of the curve, the specific surface area of the mesopores S_m can be determined. The intersection point of both straight lines gives the median radius of the micropores in the sample.
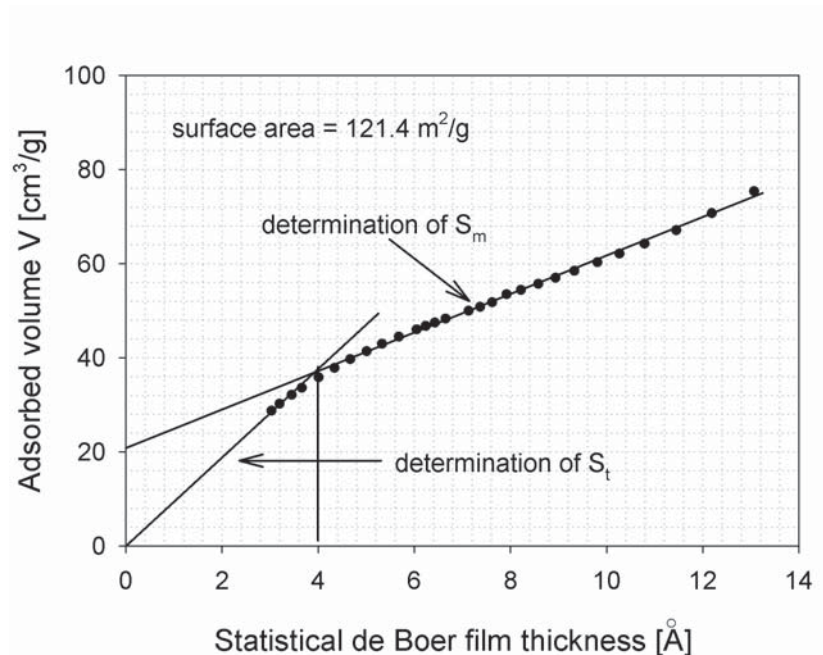

Figure A.5.: V-t-plot of a microporous milled alumina sample [Somm 07]

In Fig. A.6 and Fig. A.7, the V-t-plots of the materials used in this work are presented. For each material system, the final sample after the grinding treatment was analyzed. The linear regression reveal that the measured data lie on a straight line that passes roughly through the origin. Hence, the formation of micropores can be neglected for the investigated systems. Some regression curves show negative axis intercepts which could be related to a preferred monolayer adsorption rather than the assumed multilayer adsorption in the BET approach.
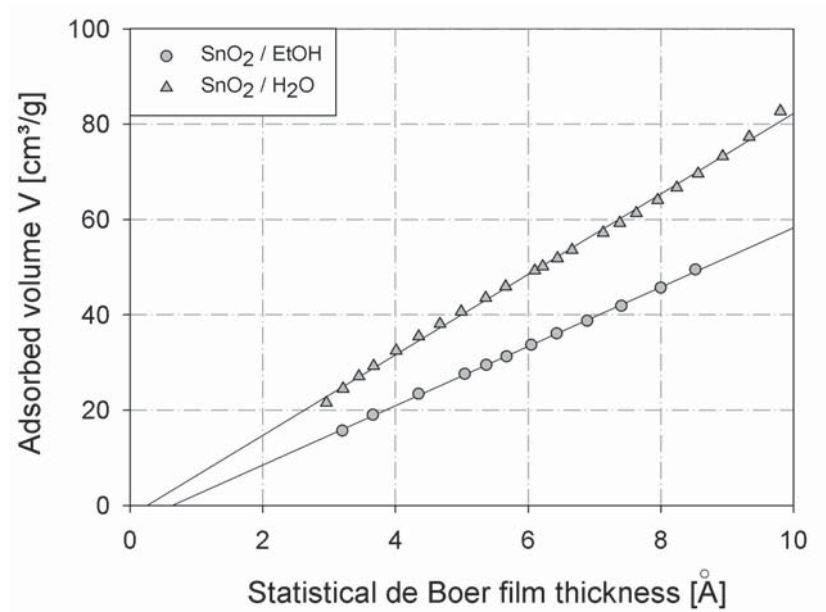
180

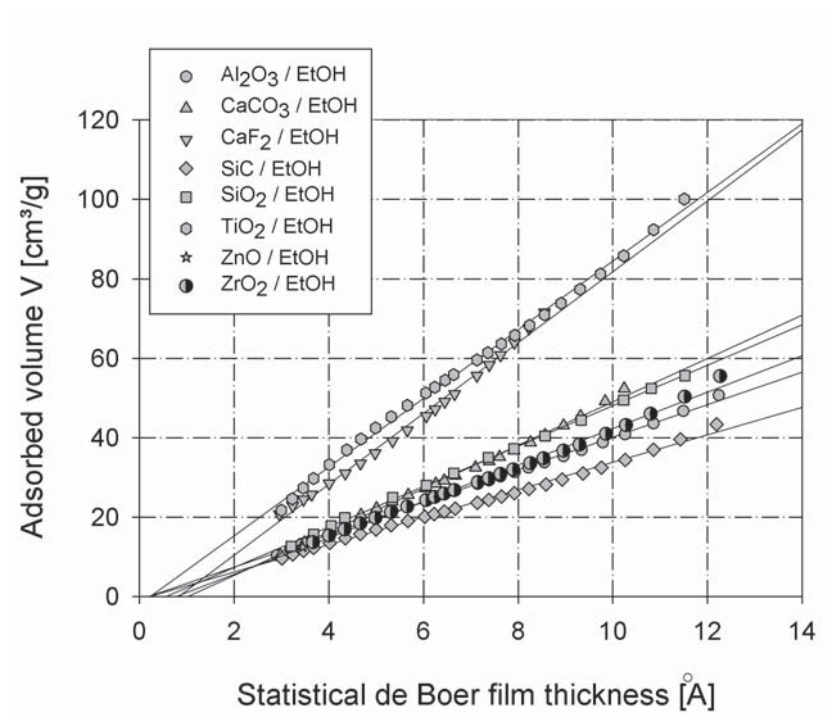Figure A.6.: V-t-plots of milled SnO_2 particles

Figure A.7.: V-t-plots of the materials used in this work (milled in ethanol)

A.4. Coating of delaminated graphite sheets

As discussed in chapter 6.5.3, the delaminated graphite sheets can be coated with platinum nanoparticles in different ways. In the following, supporting information about the experimental procedures are given for each synthesis route.

Colloidal deposition method

Pt-NP were produced via reduction of hexachloroplatinic acid (H_2PtCl_6) in an ethanol-water mixture under stirring at 78 °C for 3 h in a reflux apparatus (see Tab. A.1). PVP was used as a stabilizer for the Pt-NP. The size of the nanoparticles strongly depends on the synthesis conditions. The produced Pt-NP were mixed with a centrifuged suspension of delaminated graphite, which was milled for 3 h under standard conditions (see Tab. A.2). PVA was used as a stabilizer in the milling experiments. After the grinding treatment, the suspension was washed five times via centrifugation and redispersed in millipore water to remove unattached polymer. Finally, the suspension was centrifuged (3 min, 3000 rpm, centrifuge 5418, Eppendorf AG) to separate unpeeled thicker particles. The supernatant was mixed in ratios of 1:1 or 2:1 with the suspension of the colloidal Pt-NP and the mixture was set to rest for at least 1 hour.

Table A.1.: Colloidal deposition method - Preparation of Pt-NP suspension

Reactant	Amount
H_2PtCl_6-solution (6 mM)	5 ml
Ethanol (analytical)	40.5 ml
Millipore water	4.5 ml
PVP	7.5 mg
Apparatus	reflux system
Time	> 3 h
Temperature	78 °C -79 °C

Table A.2.: Colloidal deposition method - Delamination conditions

Parameter	Condition
Solid content	1 wt% GS 6
Milling time	3 h
Grinding media	0.1 mm YSZ
Revolution speed stirrer	1500 rpm
Stabilizer	PVA
c_{PVA}	1 wt%

Wet impregnation method

After delamination in the stirred media mill (conditions see Tab. A.3), the suspension was centrifuged (3 min, 3000 rpm, centrifuge 5418, Eppendorf AG) to remove unpeeled thicker particles. Hexachloroplatinic acid was added to the suspension. The ions of the hexachloroplatinic acid attach to the sheet's surface and were reduced to Pt-NP either by the addition of sodium borohydrate or ethanol (Tab. A.4). Since the negatively charged chloroplatinate ions do not adsorb on a negatively charged graphite-SDS surface, the graphite particles were stabilized in the milling experiments with the nonionic surfactant dodecyl dimethyl amino oxide (DMAO).

Table A.3.: Wet impregnation method - Delamination conditions

Parameter	Condition
Solid content	1 wt% GS 6
Milling time	5 h
Grinding media	0.1 mm YSZ
Revolution speed stirrer	1500 rpm
Stabilizer	DMAO
c_{DMAO}	10 mM

Table A.4.: Wet impregnation method - Coating conditions

Parameter	NaBH$_4$ reduction	EtOH reduction
c$_{\text{H}_2\text{PtCl}_6}$	10 mM	6 mM
V(GS-susp.):V(H$_2$PtCl$_6$-solu.)	2:1	4:1
Amount reduction medium	slight excess of NaBH$_4$	times 9 of GS-H$_2$PtCl$_6$-volume
Apparatus	beaker	reflux system
Impregnation time	> 30 min	> 3 h
Temperature	RT	78 °C -79 °C

Curriculum Vitae

Personal Data

Name	Catharina Knieke
Date of Birth	07/23/1981
Place of Birth	Hildesheim, Niedersachsen
Citizenship	German
E-Mail	Catharina.Knieke@gmx.de

Education

09/88 – 07/92	Elementary School, Borsum
09/92 – 07/94	Middle School, Harsum
09/94 – 06/01	Michelsen Secondary School, Hildesheim
10/01 – 05/06	TU Clausthal, Studies of Process Engineering
09/05 – 05/06	Internship and Diploma thesis with BASF AG, Ludwigshafen
07/06 – 09/10	Research Associate at the Institute of Particle Technology, University Erlangen-Nürnberg
11/10 – 11/11	Research Associate at the New Jersey Institute of Technology, NJ, USA
since 02/12	Research Engineer with BASF SE, Ludwigshafen